Doctoral Dissertation

Studies on Control of Backbone Orientation and Molecular Design of Copolymer Bearing Isoindigo Pigment for Organic Photovoltaics

(有機太陽電池を志向したイソインディゴ色素を有する
共重合体の主鎖配向制御と分子設計に関する研究)

Marina Ide

January 2017

Department of Applied Chemistry,
Graduate School of Engineering,
Osaka University

Preface

The studies presented in this dissertation were carried out under the direction of Associate Professor Akinori Saeki at Department of Applied Chemistry, Graduate School of Engineering, Osaka University and Professor Shu Seki at Department of Molecular Engineering, Graduate School of Engineering, Kyoto University.

The objective in this dissertation is to provide insights into the organic semiconducting copolymers bearing an analogue of isoindigo pigment, including their synthesis procedures, organic photovoltaic devices, and optoelectronic evaluations. The author hopes these results and findings contribute to the molecular design of semiconducting copolymers for organic photovoltaics.

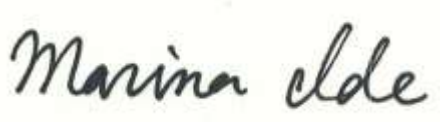

Marina Ide

Department of Applied Chemistry

Graduate School of Engineering

Osaka University, Japan

January 2017

Contents

Chapter 1: General Introduction

Renewable energy sources, which do not rely on oil and coal from the earth, are in strong demands all over the world. Development of an energy harvesting system is highly required to maintain human lives in the future. Chemical engineering including synthesis and processing of functional materials is one of the most plausible solutions to overcome the energy shortage, which could produce affordable energies from natural sources. Among the renewable energy sources, photovoltaic cells have been most intensively investigated, where the highest efficiencies are frequently updated in the NREL website[1]. Commercialized crystal silicon photovoltaics have reached over 20% power conversion efficiency (PCE), while an expensive InGaAs/InAs tandem cell over 40% efficiency is limited in the specific applications like a space satellite.

On the other hand, flexible and light-weight photovoltaics using organic materials are one of the frontier researches in recent years.[2] Furthermore, an inorganic-organic hybrid perovskite was firstly introduced in dye sensitized solar cell (DSSC) by T. Miyasaka *et al*. in 2009 and achieved 3.8% PCE with methyl ammonium lead iodine.[3] Currently 21% PCE has been demonstrated in all-solid perovskite solar cell by M. Saliba *et al*., and the stability of the device was improved by addition of inorganic cesium, resulting in thermally stable cation perovskite.[4] However, lead atom composing the perovskite is extremely harmful for human health as reported by World Health Organization,[5] and thus reduction or removal of toxic lead from perovskite solar cells is still in the course of investigation. The examples are methylammonium tin halide perovskite semiconductors[6] and low toxic bismuth halide.[7]

Generally organic photovoltaics composed of polymers or molecules are toxic-element-free flexible films. In 1989, C. W. Tang reported the first organic photovoltaic (OPV) cell of p/n bilayer structure (copper phthalocyanine and perylene derivative) fabricated by using evaporation technique and achieved ~1% PCE.[8] In 1995, A. J. Heeger *et al.* reported the bulk hetero-junction (BHJ) solar cell with

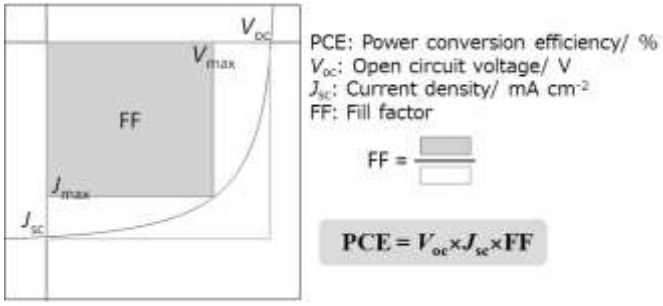

Figure 1. Typical *J*-*V* characteristics of a photovoltaics.

poly(2-methoxy-5-(2'-ethyl-hexyloxy)1,4-phenylenevinylene) (MEH-PPV) and fullerene blend film.[9] This concept significantly increased the current density and reached rather high PCE due to the increment of J_{sc} (Figure 1), because BHJ structure promotes the charge generation that leads to high current density even though it also increases the charge recombination. Numerous donor–acceptor type copolymers have been reported with this BHJ structure and recently PCE achieved over 10%. C. C. Chen *et al.*[10] demonstrated a triple junction organic tandem solar cell with 11.6% PCE composed of several polymers, which was designed to maximize the tandem photocurrent output. Polymers with different bandgaps can cover the wide wavelength region from 300 to 1000 nm, by virtue of the thickness-optimized subcell at around 85–160 nm. H. Hu *et al.*,[11] also achieved 10.7% PCE with a series of difluorobenzothiadizole and oligothiophene-based polymers shown in Figure 2. They provided the important results to tune the energy levels and morphologies of blend films by molecular designing to enhance PCE. In addition, non-fullerene organic solar cell with 10.9% PCE was demonstrated by Z. Li *et al.*, suggesting that a non-fullerene acceptor is also the promising strategy that satisfies both electron transfer and optimal morphology.[12]

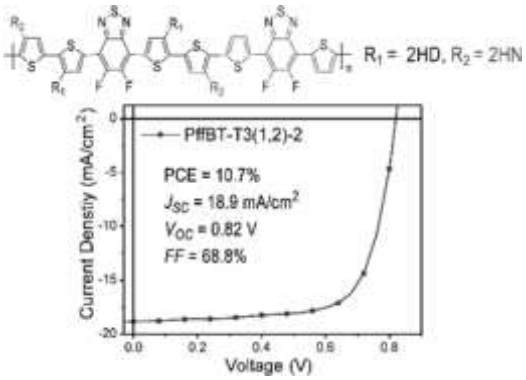

Figure 2. Chemical structure of difluorobenzothiadizole and oligothiophene-based polymers. J-V curve of polymer;PCBM solar cell. (ref 11) Copyright 2015 American Chemical Society.

Of importance in OPV fabrication is the way to obtain a maximized electric power from the aspects of molecular design, photoexcitation related to quantum efficiency, charge generation, charge separation, and charge mobility.[13] OPVs are relatively easy to be fabricated in comparison with inorganic photovoltaics; however, the low carrier mobility and limited absorption region are significant disadvantages over inorganic counterparts. Open circuit voltage (V_{oc}), current density (J_{sc}) and fill factor (FF), which are the parameters of OPV device performance, are influenced by solubility, crystallinity, absorption, charge separation efficiency, and charge transport, which hinder the efficient development of organic electronics.

1-1. Molecular designing

1-1-1. Optimal electronic absorption spectra for OPV

Common organic semiconducting polymers demonstrate wide absorption from visible to near infrared region (300 – 800 nm) for example poly(3-hexylthiophene) (P3HT)[14,15], poly[2,6-(4,4-bis-(2-ethylhexyl)-*4H*-cyclopenta[2,1-b;3,4-b0]dithiophene) -alt-4,7-(2,1,3-benzothiadiazole)]) (PCPDTBT) [16] and poly[4,8-bis-substitutedbenzo [1,2-b:4,5-b']dithiophene-2,6-diyl-alt-4-substitutedthieno[3,4b]thiophene-2,6-diyl] (PTB7)[17,18]. P3HT achieved 3–4% PCE by blending with [6,6]-phenyl-C_{61}-butyric acid methyl ester ($PC_{61}BM$), of which absorption range covers up to around 700 nm. Low bandgap copolymers like PCPDTBT and PTB7 indicate wider absorption spectra than P3HT, and therefore, the density of generated charge carrier is increased in the blend films.[19] The sunlight, which follows Plank equation of black body radiation at 5500 ^{o}C, comprises of the wide range of wavelength from the visible region to the infrared region (<3000 nm). And thus, there is still a room to improve the current density by expanding the absorption spectra of copolymers. One of the facile strategies to this end is a selection of strong donor and acceptor chromophores that are connected in the alternative fashion, leading to the narrower bandgap. In addition, π-stacking of polymer backbone influences the redshift of absorption spectra, which also contributes to the increase of current density.

Therefore, near infrared region is unexplored but promised area that benefits to the improvement of OPV device efficiencies.[20] In order to manipulate the energy level, development of an optimal acceptor with shallow LUMO and deep HOMO level is essential for high V_{oc}. For example, 2-ethylhexyl-3-fluorothieno[3,4-b]thiophene c-2-carboxylate composed of PTB7 is one of the strong acceptor units in OPV copolymers, where PTB7 achieved the 9.2% PCE[18] by Z. He *et al*. They also reported polyfluorene derivative as the electron transfer layer (= hole blocking layer), which leads to the effective charge transport.

1-1-2. Ideal energy gap for OPV

V_{oc} is basically proportional to the energy gap between the HOMO level of a p-type semiconductor and the LUMO level of an n-type semiconductor (Figure 3). The V_{oc} is also relating to the energy level of charge transfer (CT) state. Copolymers should be designed based on the ideal bandgap and suitable LUMO level with $PC_{61}BM$, which is a typical, versatile n-type semiconducting material for efficient charge separation and transport.[21] Intrinsically, V_{oc} is less than the bandgap due to a certain energy loss in OPV, which is illustrated in 2006 by M. C. Scharber *et al*. who assume the unavoidable

energy loss of at least ~ 0.3 V due to the dark current and field driven properties.[22] Insufficient energy gap between LUMOs of p- and n-type semiconducting materials could impede the charge separation and induce the charge recombination. This leads to the decreases in J_{sc} and PCE of OPV devices. In other words, an excessively deep LUMO level of conjugated copolymers is detrimental to the charge separation. Tuning of energy level of donor and acceptor units in alternating copolymers is a general strategy to improve V_{oc}.

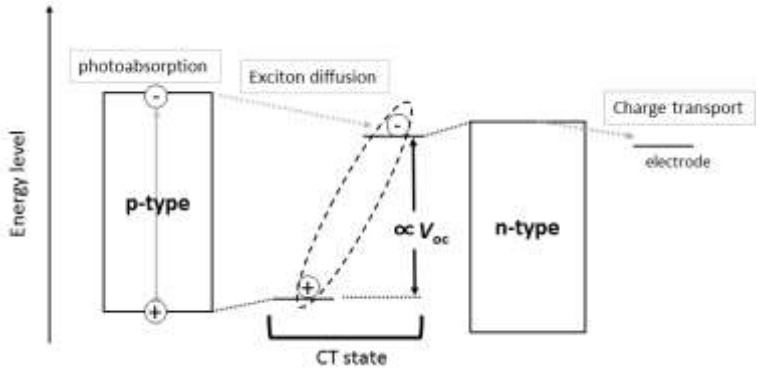

Figure 3. Schematic energy transport in OPV devices.

1-2. Common acceptor moiety for alternative copolymers

1-2-1. Diketopyrrolopyrrole acceptor

Symmetric acceptor, diketopyrrolopyrrole (DPP) unit has been widely investigated in recent years.[23] (Figure 4a) In 1974 D. G. Farnum *et al*. firstly synthesized DPP unit,[24] and further facile synthesis procedure has been developed so far. DPP unit demonstrates a quasi-planar structure due to non-bonding interaction between the oxygen of ketone and the sulfur of thiophene that is connected to the DPP (Sulfur…Oxygen (S…O) interaction).[25] Interestingly, DPP copolymers demonstrated face-on orientation rather than DPP copolymers without S…O interaction.[26] Recently W. S. Yoon *et al*. reported 8.2% PCE with P(NTDT)-BDT polymer by using the bis-lactam acceptor that is an analogue of DPP reducing repulsion by molecular

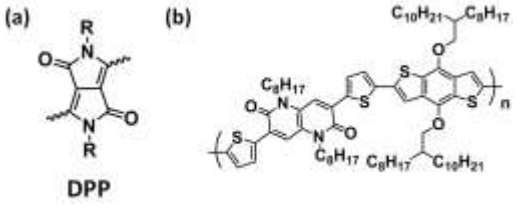

Figure 4. (a) Chemical structure of DPP unit. (b) Chemical structure of P(NTDT)-BDT, reproduced from ref 27. Copyright 2016 American Chemical Society.

designing.[27] (Figure 4b) Remarkably Y. Ji *et al*. synthesized asymmetric DPP copolymers[28] via two-step reactions, resulting in 6.5% PCE by improving its molecular weight and solubility. This is the first report of asymmetric copolymers except for the sensitizers used in DSSC.[29,30] Moreover, L. Dou *et al*. achieved 8.6% PCE in tandem solar cell for the DPP copolymers with 2D-benzodithiophene (BDT) that is BDT with thiophenes in the vertical direction of polymer backbone.[31]

Regarding the mobility enhancement, bulkiness of side chain is believed to influence the orientation of copolymers, for instance, G. –Y. Lee *et al*. achieved the field effect transistor (OFET) hole mobility of 2.27 $cm^2\ V^{-1}\ s^{-1}$ by controlling backbone planarity and intramolecular interaction.[32] Notable ambipolar character has been also investigated for DPP copolymers with benzene spacers, providing high hole and electron mobilities of 8.84 and 4.34 $cm^2\ V^{-1}\ s^{-1}$, respectively.[33] They reported the side chain engineering by siloxane termination that contributes to the formation of efficient π–π stacking with face-on orientations. As the further examples, A. Zhang *et al*. demonstrated the highest OFET mobility of 11.2 $cm^2\ V^{-1}\ s^{-1}$ by controlling the backbone orientation of DPP copolymer bearing bithiophene.[34] It is also possible to tune the orientation of DPP copolymers by introducing various spacers next to DPP, such as thiophene,[35] benzene[36] and thienothiophene.[37]

The advantages of DPP are (a) high quasi–planarity of π-plane, (b) strong accepting property, and (c) facile synthesis procedure. In details, the coplanar structure of copolymer backbone would promote the intermolecular π-stacking in OPV and charge transfer efficiency.[27] While the strong acceptor allows for tuning energy level of copolymers, it can also cause a shallow HOMO level and suppression of V_{oc}. Control of energy level of a copolymer could lead to a high charge separation efficiency and dramatic increase in PCEs. Thus DPP moiety synthesized by facile procedures is one of the attractive electron-accepting chromophores to reach a high PCE.[38]

1-2-2. Isoindigo acceptor

Isoindigo (IDG) that is a structural isomer of blue dye indigo has the symmetric lactam structure (Figure 5a), and acts as the acceptor unit in donor–acceptor alternating copolymers.[39] Introducing alkyl chain on nitrogen of IDG can adjust solubility of IDG copolymers, and so far various IDG copolymers have been reported in electronic devices. IDG oligomer coupled with bithiophene achieved 1.76% PCE in single cell structure of OPV in 2010 reported by J. Mei *et al.*[40] The alternative copolymer coupled with terthiphene was developed by E. Wang *et al*., and 6.3% PCE was achieved.[41] The choice of solvent used in the wet-processed OPV fabrication has a considerable impact

on the orientation of polymer backbone in a thin film. Z. Ma *et al.* investigated the different films spun-cast from different solvents and found that trichlorobenzene showed the best PCE of 7.3% (Figure 5b).[42] In addition, selection of the donor moiety significantly impacts the efficiency of charge transport. For instance, thiophene and terthiophene coupled with BDT and IDG demonstrated different photoluminescence quenching efficiency due to the energetic loss, resulting in the higher J_{sc}, FF and PCE in terthiophene copolymer than those in thiophene copolymer.[43] Orientation trend by introducing thiophene spacer between BDT donor and isoindigo acceptor was discussed by using photoluminescence measurement by Z. Ma *et al*. They proposed that thiophene spacers without alkyl chain contribute to the alignment of backbone orientation.[44] Similarly, IDG coupled with sexthiophene copolymers were designed from the aspect of centrosymmetry structure,[45] leading to a high crystallinity and a high J_{sc} of 16.2 mA cm^{-2}. Interestingly, centrosymmetric structure provides higher crystallinity and sexthiophene-IDG alternative copolymer achieved 7.3% PCE. However, the band gaps of IDG copolymers were around 1.5 eV and further molecular designing can boost the current density by controlling the absorption region to cover whole solar spectrum.[39]

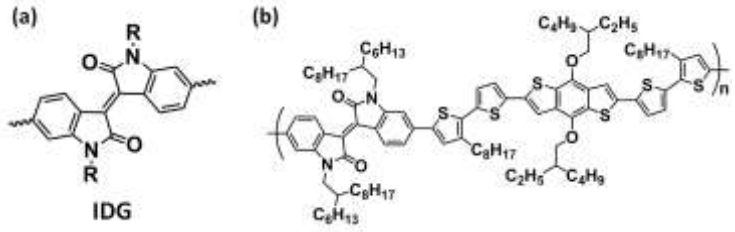

Figure 5. (a) Chemical structure of IDG unit. (b) Chemical structure of PBDT-BTI, reproduced from ref 42. Copyright 2014 WILEY-VCH.

Molecular engineering by introducing a halogen atom on the benzene of IDG is an effective route towards increasing not only PCE but also mobilities of IDG copolymers. For example, fluorination of IDG acceptor induced the low-lying LUMO level, providing the ambient stability. Therefore, T. Lei *et al*. synthesized fluorinated IDG and performed OFET evaluation for hole and electron, reaching 1.85 cm^2 V^{-1} s^{-1} and 0.43 cm^2 V^{-1} s^{-1}, respectively.[46] They controlled the interchain interaction of polymer backbone, leading to different packing structure in the thin film. Moreover fluorinated IDG copolymers tend to form an edge-on orientation and mobilities are increased due to the efficient charge transport through π-π stacking. Chlorination of IDG also demonstrated ambipolar nature with the hole mobility of 0.81 cm^2 V^{-1} s^{-1} and mostly the same electron mobility of 0.66 cm^2 V^{-1} s^{-1}.[47] Additionally, choosing optimal alkyl chain of IDG moiety significantly increased the mobility, for example by using

siloxane termination (0.57 $cm^2 V^{-1} s^{-1}$)[48] and shifting the branching point of alkyl side chain away from the backbone.[49] IDG copolymers show absorption from visible (300 nm) to near infrared (NIR) region (900 nm); however, the solar spectrum is further extending to the near infrared, and accordingly, a plenty of rooms are left to improve the current density.

1-2-3. Thienoisoindigo acceptor

Although IDG copolymers has attractive properties, the IDG unit is slightly twisted (vide infra), because of the structural repulsion between proton of phenyl and oxygen of ketone. This twist reduces the donor-acceptor interactions, the effective conjugation length, and the stacking interactions of the polymer chains, adversely affecting the device performance.

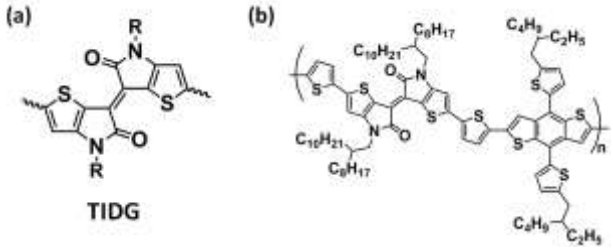

Figure 6. (a) Chemical structure of TIDG unit. (b) Chemical structure of PBDT-TIIG, reproduced from ref 63. Copyright 2015 American Chemical Society.

To overcome this drawback, 4,4'-bis(alkyl)-[6,6'-bithieno[3,2-b]pyrrolylidene] -5,5'(4*H*,4'*H*)-dione units, so-called thienoisoindigo (TIDG) was synthesized instead of IDG for the development of low-band gap conjugated polymers (Figure 6a). TIDG consists of five-membered heterocyclic aromatic rings, which can grant a higher planarity to the molecular plane than that of arylene groups, leading to the enhanced charge delocalization via quinoidal structure of the backbone. It promises the higher planarity and stronger electron accepting properties than IDG, and copolymers composed of TIDG are suitable for the use as a near-infrared photodetectors and as a donor–acceptor polymer. Several near-infrared absorbing copolymers bearing thienoisoindigo were reported, and the band edges of photoabsorption reached over 1500 nm[50] or 2500 nm.[51] Synthesis of a similar structure of TIDG was reported firstly in 2002 by D. J. Lee *et al*. but practical application for electronic devices was not demonstrated,[52] except for one patent.[53] In 2012, R. S. Ashraf *et al*. reported the synthesis and OFET properties of TIDG-benzothiadiazole copolymers, which revealed an unprecedented ambipolar nature with comparable hole and electron mobilities over 0.1 $cm^2 V^{-1} s^{-1}$,[54] demonstrating the intriguing electronic features of TIDG-based

copolymer family. Y. Koizumi *et al*.[55] and G. W. P. Van Pruissen *et al*.[56] also evaluated hole mobility of TIDG copolymers by OFET, and both groups reported that synthesized TIDG copolymers have remarkable NIR absorbing properties. Further investigation for TIDG oligomers[57,58] or copolymers[59] are reported regarding the OPV devices. G. Kim *et al*. achieved a prominent hole mobility of 14.4 cm^2 V^{-1} s^{-1} by coupling the naphthalene with TIDG[60] and the naphthalene–TIDG copolymer formed edge-on orientation with 70% majority in the entire films. G. Kim *et al*. investigated the interplay between crystallinity and morphology and concluded that formation of high crystalline domain and dense molecular packing provided the high OFET hole mobility.[61]

As for the TIDG copolymers for OPV, 1.4% PCE of TIDG copolymer coupled with fluorene was investigated, whereas TIDG copolymers had the trend of significant loss of J_{sc} because of bulk recombination in blend film.[62] In 2015, C. Lu *et al*. demonstrated the 2.55 % PCE by alternative copolymer coupled with BDT,[63] (Figure 6b) and the TIDG copolymer showed broadened incident photon-to-current efficiencies (IPCE) from visible to NIR region; however, the relatively low V_{oc} was due to the high-lying HOMO level as is the case for another report.[62]

In comparison with IDG copolymers, TIDG copolymers have both drawbacks and advantages regarding the electronic device application. Coplanar structure has a possibility to improve the PCE because it can reduce the π–π stacking and demonstrate high crystallinity. In addition, TIDG copolymers are prospected as the use in tandem solar cell in respect of broad absorption from visible to NIR region.

1-3. Measurement techniques for OPV blend films

1-3-1. Mobility measurement

Charge carrier mobility of organic semiconducting copolymer is a crucial parameter to determine the efficiency of charge transport. In OPV, transporting rate relates to the charge recombination, and thus, charge carriers with high mobility merit the high photo current density. Besides, the balance of hole and electron mobilities in OPV devices impacts the PCE and unbalanced mobilities results in lower efficiency.[64] Generally hole mobilities (μ_h) of organic semiconducting

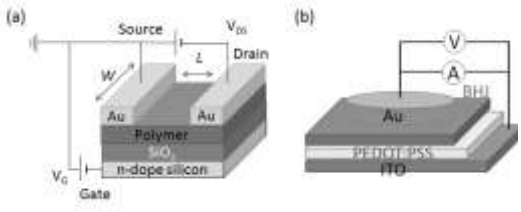

Figure 7 (a) FET device structure of bottom gate – top contact type. (b) SCLC device structure for hole mobility measurement.

copolymers are measured by using an organic field-effect transistor (OFET)[65,66] or a space-charge limited current (SCLC)[67] technique. The structure of OFET devices is illustrated in Figure 7, which is a bottom gate–top contact type OFET. Compounds are drop-casted or spun-coat on the silicon substrate covered with insulating dielectric SiO_2 layer. Hole transport from an electrode (source) to another electrode (drain) is in the parallel direction to the substrate. Packing orientation of polymer dominates the charge transport, and therefore, the edge-on orientation is preferable for the high mobility in OFET measurement.[68] For example, IDG copolymers functionalized with fluorine increased their hole mobilities because of the edge-on orientation.[46] The π–π stacking ability and molecular orientation in thin film can be discussed from the OFET measurement, providing us useful insights to consider the charge carrier mobility.

SCLC measurement is also one of evaluation techniques of charge carrier mobility in thin films, by fabrication of hole or electron only device.[67] Most importantly, SCLC mobility reflects the vertical transport of charge carriers, similar to solar cells.[69,70] The mobility is varied by the morphology of thin films modified by additive,[71] which often modulates the PCE of OPV device.

1-3-2. Transient absorption spectroscopy (TAS)

To provide an access to the fundamental in OPVs, the sequential processes from the formation of exciton, the diffusion of exciton, the charge separation, to the charge transport should be divided into each cascade. Photoexcitation promptly generates excitons via Frank-Condon principle. They diffuse to the interface between donor and acceptor, giving rise to bound or free charge carriers under the Coulombic potential. Subsequently, the charge carriers are transported to the electrode, while some of charge carriers recombine before the charge collection at the buffer/electrode. The sequence of photocurrent generation is directly accessed by using transient absorption spectroscopy (TAS), which allows monitoring of the dynamics of excitons, bound interfacial CT states, and free charge carriers. For example, regio-regular (RR) and regio-random (RRa) P3HT show significant differences in crystallinity,[72,73] PCE,[15] and mobility.[74] J. Guo *et al*. evaluated the pristine RR- and RRa-P3HT by using TAS and found that RRa-P3HT yielded a large number of triplet excitation state, which has a long lifetime in the microsecond order and is quenched under an O_2 atmosphere, whereas no long-lived transients were observed in RR-P3HT.[75] They assigned the absorption bands at 700 nm (RRa-P3HT) and at 650 nm (RR-P3HT) to the polaron pairs (positive and negative charge carriers interacting with phonon), where the blue-shifted absorption was due to a shorter electron-hole separation of polaron pairs in the

RR-P3HT crystalline domain rather than in the RRa-P3HT amorphous domain.

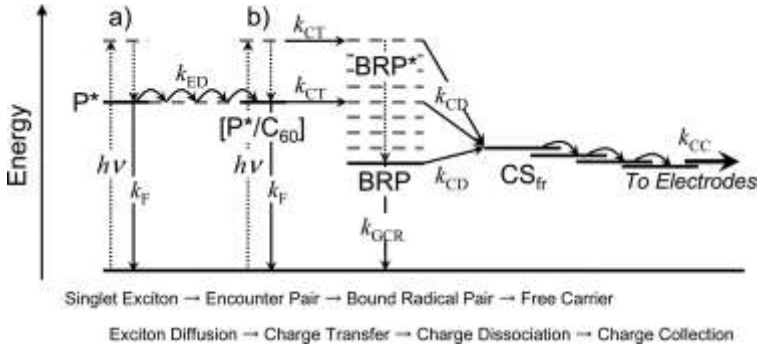

Figure 8. Energy Diagrams of Fundamental Photovoltaic Conversion Processes in P3HT/PCBM Solar Cells. The energy levels involved in photovoltaic conversion are as follows: P*, singlet exciton (a, P3HT crystalline domain; b, P3HT/PCBM interface); [P*/C60], encounter pair; BRP*, nonrelaxed bound radical pair; BRP, relaxed bound radical pair; CS_{fr}, free carrier. The fundamental processes for photovoltaic conversion are as follows: *hv*, light absorption; k_F, total monomolecular deactivations of singlet excitons in P3HT pristine films; k_{ED}, singlet exciton diffusion to the P3HT/PCBM interface and formation of encounter pair; k_{CT}, charge transfer from P3HT to PCBM; k_{GCR}, geminate recombination of bound radical pair; k_{CD}, charge dissociation from bound radical pair; k_{CC}, charge collection of free carriers. Copyright 2010 American Chemical Society. (ref 75)

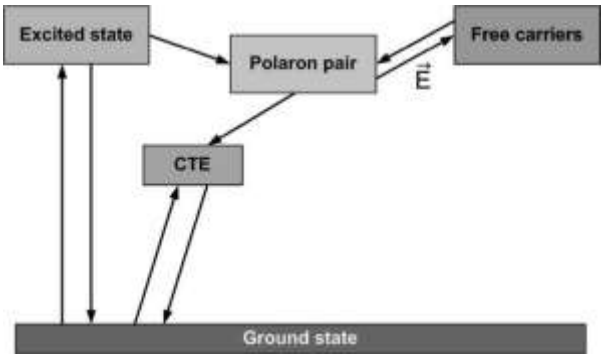

Figure 9. Schematic representation of the excitation in the BHJ under study. For simplicity only the excited state of the polymer is indicated, triplet levels are also omitted. The charge transfer exciton (CTE) state is related to the lowest excited state in the system, and that its presence is extremely relevant to the device's function. Reproduced from ref 78 with permission from 2007 WILEY-VCH.

The same group demonstrated the TAS measurement in P3HT:PCBM blend films, of which observation is in accordance with the practical performance of OPV.[76] They illustrated that the efficiency of charge generation has negligible differences between RR-P3HT and RRa-P3HT, whereas RR-P3HT demonstrated the highly charge dissociation efficiency specifically after thermal annealing (Figure 8). In other words,

RR-P3HT can promote the charge dissociation and formation of free charge carrier as a result of forming desirable phase separated structure in blend film. They revealed that the charge dissociation and collection have a crucial impact on a device performance in P3HT:PCBM solar cells.

Charge transporting mechanism of the low bandgap copolymer PCPDTBT, of which PCE was improved to ~5% by using high-boiling point additive,[16] was evaluated by TAS measurement. In 2007, I. –W. Hwang *et al*. investigated the charge separation mechanism in PCPDTBT:PCBM blend film, indicating the ultrafast photoinduced electron transfer. The relaxation dynamics in the PCPDTBT:PCBM blend film suggested the long-lived mobile carriers without fast recombination channel via CT state.[77] Photoluminescence quenching efficiency in the blend film was also investigated, indicating that the loss pathway was mainly through the CT state (Figure 9, shown as CTE state).[78] Its fast recombination process in PCPDTBT:PCBM was due to the rapid geminate recombination via CT state, leading to the suppression of the external quantum efficiency (EQE) spectra. S. Yamamoto *et al.* investigated the efficiency-limiting process of PCPDTBT:PCBM via TAS measurement and suggested that charge generation efficiency of PCPDTBT was almost 100% which was larger than RR-P3HT but charge dissociation efficiency in PCPDTBT was dominated by the delocalization of singlet exciton (Figure 10).[79] They concluded that the lower EQE of PCPDTBT:PCBM (maximum 70%) than that of RR-P3HT:PCBM was ascribed to the lower charge dissociation and the shorter charge lifetime. In addition, additive enhancement was studied by F. Etzold *et al*. for PCPDTBT to examine the improvement of PCE by addition of high boiling point chemical, 1,8-octanedithiol (ODT) [80] by TAS measurement from visible to NIR region. Additive increased the demixing of morphology towards polymer enriched domain, resulting in suppression of nongeminate recombination, implying a higher yield of free charge carriers. Furthermore P. C. Y. Chow *et al*. investigated the influence of triplet exciton upon addition of ODT on the OPV devices. It was turned out that geminate recombination in PCPDTBT is a

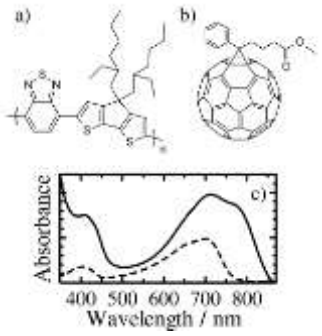

Figure 10. Chemical structures of materials (a) PCPDTBT and (b) PCBM. (c) Absorption spectra of PCPDTBT/PCBM blend films (50:50 w/w) fabricated with DIO (solid line) and of toluene solution of PCPDTBT (broken line). Copyright 2012 American Chemical Society. (ref 79)

governing factor in OPV.[81]

Another low bandgap copolymer PTB7 is often regarded as the benchmark system of efficient OPV to evaluate charge transporting mechanism.[18] 1,8-diiodeoctane (DIO), a versatile, useful additive, was found to enhance initial generation of bound and free charge carriers in the PTB7:PCBM blend film.[82] PTB7:PCBM blend film featured an ultrafast rise in TAS kinetics, meaning that effective charge separation in BHJ film.[19] Whereas back electron transfer is not the main loss pathway like PCPDTBT. [83] It is important to reveal the loss pathways of charge carriers on the basis of TAS results. For instance, geminate recombination process through the CT state is not sensitive to the carrier density (laser power), while the decay rate of bulk recombination is accelerated upon increased carrier density. As described above, TAS measurement is a powerful evaluation technique to determine the mechanisms of charge generation and transport in OPV devices, providing the strategy to improve the PCE and suppress the unfavorable pathways.

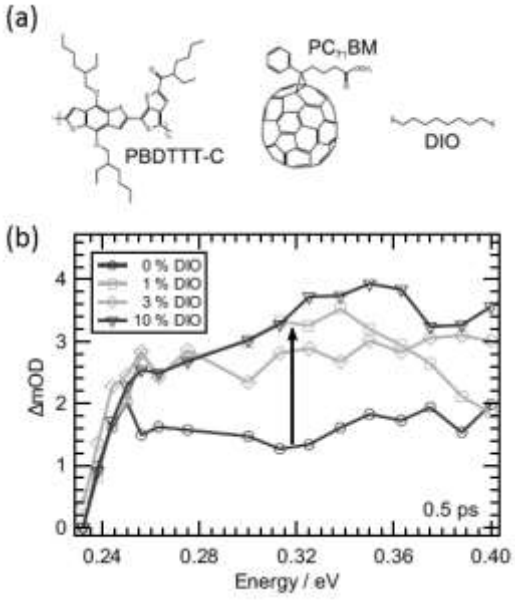

Figure 11. (a) Molecular structure of PBDTTT-C (PTB7), $PC_{71}BM$ and DIO. (b) Initial (0.5 ps) TA spectra probed in the 0.24 to 0.4 eV region. Already the use of 1% DIO results in an enhanced initial generation of bound and free charge carriers (arrow) staying on a similarly high level for the 3% and 10% film. Copyright 2015 Nature publishing group. Reproduced from ref 82.

1-3-3. Time-resolved microwave conductivity (TRMC) measurement

Device fabrication of OPV and various electronic devices definitely include contact issues at the electrode, and intrinsic charge carrier conductivity is difficult to be estimated appropriately. Time-resolved microwave conductivity (TRMC) measurement is one of the powerful techniques to measure transient conductivity in order to avoid the undesirable contact resistance and trapping of carrier.[84] OFET and SCLC measurement need high electronic fields to induce charge carrier transport, resulting in denser trapping and suppression of conductivity. On the other hand, TRMC measurement is conducted without attaching electrodes on a sample, and it enables to measure the

transient photoconductivity by using pulse radiolysis,[85] flash photolysis[86,87] or white lamp.[88] TRMC photoconductivity is found to directly correlate to PCE,[86,88] allowing for a facile evaluation of BHJ films without device fabrications. Thus, TRMC transient is not subject to influences such as BHJ/metal interfacial issues, impurities, and degradation of the buffer and active layers.

BHJ is a blend film of p- and n-type semiconducting materials, and their optimal mixing ratio is dependent on each material. In 2011, the TRMC transient conductivity of P3HT:PCBM was investigated by A. Saeki *et al*., and they found that the product of photoconductivity maxima and lifetime is correlated with the device efficiency, demonstrating that TRMC measurement can reveal the optimal blending ratio and processing condition without device characterization.[86] Laser-flash photolysis TRMC uses a monochrome pulse, which is not as similar as solar spectrum, and thus, TRMC system using a white light pulse from a Xe-flash lamp was developed by the same group.[88] The Xe-flash TRMC provides the optimal blending ratio of BHJ film and shows a good correlation between the transient maxima and PCE/V_{oc} among four kinds of low bandgap polymer, which allows to accelerate the screening of OPV materials.

1-4. Backbone orientation of copolymers for OPV

Of crucial strategy to design an efficient OPV polymer is leveraged on the deeper understanding on the optoelectronic and morphological properties. IDG copolymers achieved the high PCEs by controlling the packing structure and improving mobility, but the film orientation of IDG copolymers are predominately edge-on, which is not advantageous for OPV devices. In general, face-on orientation is preferred for the charge transport in OPV devices,[89] as regarding to the enhancement of electronic coupling between donor and acceptor.[90] Short π–π stacking distance generally shows the high charge carrier mobility advantageous to achieve the high performance. Coplanarity of polymer backbone can suppress the decrement of mobility, resulting in competent charge transport in blend film.[91] In addition, size of aggregation and packing morphology rather than energetic offsets between polymer and fullerene derivatives

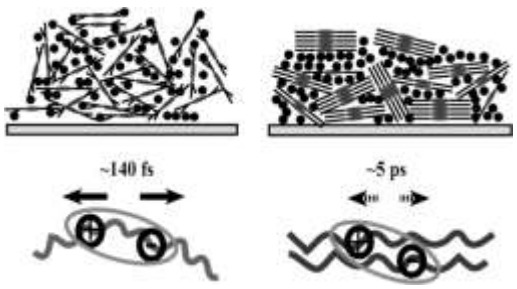

Figure 12. Schematic representation of the polymer packing in BHJs from PTB7 anaologue:PCBM (left) and PTB7:PCBM (right). Copyright 2014 American Chemical Society. (ref 95)

strongly affect the yield of free versus bound charges.[92] Numerous conjugated semiconductors are evaluated in order to optimize the morphology, energy level, crystallinity and solubility.[20]

Controlling the crystallinity of polymers towards efficient charge transporting is partly implemented by adjusting randomness of polymer backbone.[93] P3HT is one of the common homopolymers for OPV, and shows high crystalline properties especially after thermal annealing.[15] However, PTB7, which is relatively amorphous in nature and lower crystallinity than P3HT, demonstrates the higher PCE than that of P3HT. In which additive facilitates moderate phase separation, enhanced crystallinity, and hierarchical morphology optimized for effective charge separation and a high charge transport.[94] PTB7 analogue composed of different alkyl chain (2-ethylhexyl or dodecyl) was varied by Z. Guo *et al*. to tune the molecular packing and interchain interaction of the polymers in order to elucidate the charge separation pathways originating from intrachain and interchain species.[95] It was suggested that the higher polymer crystallinity leads to the slower charge separation due to coarser phase segregation and formation of the interchain excited states that are energetically unfavorable for charge separation (Figure 12). In that paper PTB7 demonstrated stronger peak of face-on orientation parallel to the substrate, and notably, the orientation is kept even after blending with PCBM. Therefore not only crystallinity but also the orientation of copolymer backbone should be taken into account to design the OPV copolymers, especially in respect to the carrier mobility.[89]

Polymer backbone orientation can be controlled by the introduction of alkyl chain into donor and acceptor unit, and dramatically changes the orientation of polymers. For example, I. Osaka *et al*. investigated the series of linear or branched side chain on the thiazolothiazole based copolymer, and performed drastic change of orientation from edge-on to face-on through fine tuning of side chain length.[96] In addition, macroscale morphology brought by the backbone regularity also affect the PCE, which is due to the precise control of backbone vector on the acceptor unit, leading very low photon energy loss in BHJ film.[97]

1-5. Outline of This Work

In this dissertation, the author argues the new pigments for optoelectronic devices, which are analogues of isoindigo. These pigments act as the electron acceptor unit in donor-acceptor alternating copolymers. Their optical, electronic, electric, and morphological properties are evaluated to reveal the structure-property relationship and pave the way towards the evolution of organic photovoltaics.

Chapter 1 introduces the background of organic photovoltaics and common acceptor moiety, for example dyketopyrrolopyrrole (DPP) and isoindigo (IDG), to summarize the outlook of pigment development. Crucial criteria to achieve high power conversion efficiency are also highlighted, and examples of low-bandgap polymers are presented.

Chapter 2 provides synthesis and characterization of the strong electron-acceptor unit thienoisoindigo (TIDG) moiety inspired by isoindigo. The new copolymers bearing TIDG are synthesized and characterized, which reveals the near infrared absorption due to the high planarity. A correlation between crystallinity and a hole mobility measured by field effect transistor is discussed. The high planarity enables TIDG copolymers to absorb wide near infrared region, which is supported by density functional theory calculation.

Chapter 3 summarizes the performance of organic photovoltaics of TIDG copolymers and a bulk charge recombination process in the OPV. Device parameters are evaluated by using an external quantum efficiency and transient absorption spectroscopy. Based on the comprehensive studies using several measurements, the reasons for the low PCE of TIDG copolymers despite the broad absorption are revealed. This perspective describes the importance of an optimized absorption for organic photovoltaics and rigid structure to form face-on orientation in the photovoltaic devices.

Chapter 4 explains the molecular design provided by TIDG copolymers to improve the OPV performance. Unsymmetric acceptor unit, benzothienoisoindigo (BTIDG), is synthesized to address the issues found in TIDG copolymers such as large absorption (shallow HOMO), short lifetime of singlet exciton, and unfavorable polymer orientation. Rigid donor units are selected as the counter donor units to simultaneously achieve moderate energy level, high crystallinity, face-on orientation, and good solubility. The author discusses the role of thiophene spacer and alkyl chains on the

backbone orientation with respect to the solubility, crystallinity and optimal morphology.

Chapter 5 summarizes this dissertation and addresses the outlooks regarding thienoisoindigo and benzothienoisoindigo as the component of organic semiconductors for efficient OPV performance.

This work emphasizes that further efforts should be directed to the molecular design of semiconducting copolymers for organic photovoltaics. In which the energy levels, crystallinity, and solubility are in a delicate interplay, and the present work provides the new insights into the effective extension of photo absorption from visible to near infrared region. The author believes that the present work contributes to the synthesis of new copolymers that allow a highly controlled orientation and unique optical properties.

References

[1] NREL website (http://www.nrel.gov/pv/assets/images/efficiency_chart.jpg)

[2] Li, G.; Zhu, R.; Yang, Y. *Nat. Photo.* **2012**, *6*, 153−161.

[3] Kojima, A.; Teshima, K.; Shirai, Y.; Miyasaka, T. *J. Am. Chem. Soc*. **2009**, *131*, 6050–6051.

[4] Saliba, M.; Matsui, T.; Seo, J.-Y.; Domanski, K.; Correa-Baena, J.-P.; Nazeeruddin, M. K.; Zakeeruddin, S. M.; Tress, W.; Abate, A.; Hagfeldt, A.; Grätzel, M. *Energy Environ. Sci*., **2016**, *9*, 1989−1997.

[5] WHO website "Lead poisoning and health" (http://www.who.int/mediacentre/factsheets/fs379/en/)

[6] Yokoyama, T.; Song, T.-B.; Cao, D. H.; Stoumpos, C. C.; Aramaki, S.; Kanatzidis, M. G. *ACS Energy Lett*. **2017**, *2*, 22−28.

[7] Johansson, M. B.; Zhu, H.; Johansson, E. M. J. *J. Phys. Chem. Lett*. **2016**, *7*, 3467−3471.

[8] C. W. Tang, *Appl. Phys. Lett*., **1986**, *48*, 183–185.

[9] Yu, G.; Gao, J.; Hummelen, J. C.; Wudl, F.; Heeger, A. J. *Science*, **1995**, *270*, 1789–1791.

[10] Chen, C.-C.; Chang, W. -H.; Yoshimura, K.; Ohya, K.; You, J.; Gao, J.; Hong, Z.; Yang Y.; *Adv. Mater*. **2014**, *26*, 5670–5677.

[11] Hu, H.; Jiang, K.; Yang, G.; Liu, J.; Li, Z.; Lin, H.; Liu, Y.; Zhao, J.; Zhang, J.; Huang, F.; Qu, Y.; Ma, W.; Yan. H.; *J. Am. Chem. Soc.* **2015**, *137*, 14149−14157.

[12] Li, Z.; Jiang , K.; Yang, G.; Lai, J. Y. L.; Ma, T.; Zhao, J.; Ma. W,; Yan, H. *Nat. Commun*. **2016**, *7*, 13094, 1-9.

[13] Ostroverkhova, O. *Chem. Rev*. **2016**, *116*, 13279–13412.

[14] Li, G.; Shrotriya, V.; Huang, J.; Yao, Y.; Moriarty, T.; Emery, K.; Yang, Y.; *Nat. Mater*. **2005**, *4*, 864–868.

[15] Kim, Y.; Cook, S.; Tuladhar, S. M.; Choulis, S. A. Nelson, J.; Durrant, J. R.; Bradley, D. C.; Giles, M.; McCulloch, I.; Ha, C.-S.; Ree, M. *Nat. Mater*, **2006**, *5*, 197−203.

[16] Peet, J.; Kim, J. Y.; Coates, N. E.; Ma, W. L.; Moses, D.; Heeger, A. J.; Bazan, G. C. *Nature Mater.* **2007**, *6*, 497–500.

[17] Liang, Y.; Xu, Z.; Xia, J.; Tsai, S.-T.; Wu, Y.; Li, G.; Ray, C.; Yu L. *Adv. Mater.* **2010**, *22*, E135–E138.

[18] He, Z.; Zhong, C.; Su, S.; Xu, M.; Wu, H.; Cao, Y. *Nat. Photo*. **2012**, *6*, 591−595.

[19] Szarko, J. M.; Rolczynski, B. S.; Lou, S. J.; Xu, T.;Strzalka, J.; Marks, T. J.; Yu, L.; Chen, L. X.; *Adv. Funct. Mater*. **2014**, *24*, 10–26.

[20] Dou, L.; Liu, Y.; Hong, Z.; Li, G.; Yang, Y. *Chem. Rev*. **2015**, *115*, 12633−12665.

[21] Faist, M. A.; Kirchartz, T.; Gong, W.; Ashraf, R. S.; McCulloch, I.; de Mello, J. C.; Ekins-Daukes, N. J. E.; Bradley, D. D. C.; Nelson, J. *J. Am. Chem. Soc.* **2012**, *134*, 685−692.

[22] Scharber, M. C.; Mühlbacher, D.; Koppe, M.; Denk, P.; Waldauf, C.; Heeger, A. J.; Brabec, C. J. *Adv. Mater*. **2006**, *18*, 789–794.

[23] Nielsen, C. B.; Turbiez, M.; McCulloch, I. *Adv. Mater*. **2013**, *25*, 1859–1880.

[24] Parnum, D. G.; Mehta, G.; Moore, G. G. I.; Siegal, F. P. *Tetrahedron Lett.*, **1974**, *29*, 2549-2552.

[25] Guo,X.; Zhou, N.; Lou,S. J.; Hennek, J. W.; Ortiz, R. P.; Butler, M. R.; Boudreault, P.-L. T.; Strzalka, J.; Morin, P.-O.; Leclerc, M.; López, N.J. T.; Ratner, M. A.; Chen, L. X.; Chang, R. P. H.; Facchetti, A.; Marks, T. J. *J. Am. Chem. Soc.* **2012**, *134*, 18427–18439.

[26] Kim, H. G.; Kang, B.; Ko, H.; Lee, J.; Shin, J.; Cho, K. *Chem. Mater*. **2015**, *27*, 829−838.

[27] Yoon, W. S.; Kim, D. W.; Park, J.-M.; Cho, I.; Kwon, O. K.; Whang, D. R. Kim, J. H.; Park, J.-H.; Young, S. P. *Macromolecules*, **2016**, *49*, 8489–8497.

[28] Ji, Y.; Xiao, C.; Wang, Q.; Zhang, J.; Li, C.; Wu, Y.; Wei, Z.; Zhan, X.; Hu, W.; Wang, Z.; Janssen, R. A. J.; Li, W. *Adv. Mater.* **2016**, *28*, 943–950.

[29] Holcombe, T. W. Yum, J.-H.; Kim, Y.; Rakstys, K.; Grätzel, M. *J. Mater. Chem. A* **2013**, *1*, 13978–13983.

[30] Huang, J.-H.; Jiang, K.-J.; Zhang, F.; Wu, W.; Li, S.-G.; Yang, L.-M.; Song, Y.-L. *RSC Adv*. **2014**, *4*, 16906–16912.

[31] Dou, L.; You, J.;Yang, J.;Chen, C.-C.; Y, He.; Murase, S.; Moriarty, T.; Emery, K.; Li, G.; Yang, Y. *Nat. Photo*. **2012**, *6*, 180–185.

[32] Lee, G.-Y.; Han, A. -R.; Kim,T.; Lee, H. R.; Oh, J. H.; Park, T. *ACS Appl. Mater. Interfaces* **2016**, *8*, 12307−12315.

[33] Lee, J.; Han, A. -R.; Yu, H.; Shin, T. J.; Yang, C.; Oh, J. H. *J. Am. Chem. Soc*., **2013**, *135*, 9540–9547.

[34] Zhang, A.; Xiao, C.; Wu, Y.; Li, C.; Ji, Y.; Li, L.; Hu, W.; Wang, Z.; Ma, Li, W. *Macromolecules* **2016**, *49*, 6431−6438.

[35] Wienk, M. M.; Turbiez, M.; Gilot, J.; Janssen, R. A. J. *Adv. Mater.* **2008**, *20*, 2556–2560.
[36] Man, W.-K.; Chen, Y.; Peng, Z.; Yu L. *J. Am. Chem. Soc.* **1993**,*115*, 11735-11743.
[37] Bronstein, H.; Chen, Z.; Ashraf, R. S.; Zhang, W.; Du, J.; Durrant, J. R.; Tuladhar, P. S.; Song, K.; Watkins, S. E.; Geerts, Y.; Wienk, M. M.; Janssen, R. A. J. Anthopoulos, T.; Sirringhaus, H.; Heeney, M.; McCulloch, I. *J. Am. Chem. Soc*. **2011**, 133, 3272-3275.
[38] Janssen, R. A. J.; Nelson, J.; *Adv. Mater*. **2013**, *25*, 1847–1858.
[39] Stalder, R.; Mei, J.; Graham, K. R.; Estrada, L. A.; Reynolds, J. R. *Chem. Mater*. **2014**, *26*, 664–678.
[40] Mei, J.; Graham, K. R.; Stalder, R.; Reynolds, J. R. *Org. Lett.*, **2010**, *12*, 4, 660
[41] Wang, E.; Ma, Z.; Zhang, Z.; Vandewal, K.; Henriksson, P.; Inganäs, O.; Zhang, F.;Andersson, M. R. *J. Am. Chem. Soc.* **2011**, *133*, 14244–14247.
[42] Ma, Z.; Dang, D.; Tang, Z.; Gedefaw, D.; Bergqvist, J.; Zhu, W.; Mammo, W.; Andersson, M. R.; Inganäs, O.; Zhang, F.; Wang. E. *Adv. Energy Mater*. **2014**, *4*, 1301455, 1-6.
[43] Vandewal, K.; Ma, Z.; Bergqvist, J.; Tang, Z.; Wang, E.; Henriksson, P.; Tvingstedt, K.; Andersson, M. R.; Zhang, F.; Inganäs, O. *Adv. Funct. Mater.* **2012**, *22*, 3480–3490.
[44] Ma, Z.; Wang, E.; Jarvid, M. E.; Henriksson, P.; Inganäs, O.; Zhang, F.; Andersson, M. R.; *J. Mater. Chem*. **2012**, *22*, 2306–2314.
[45] Ho, C.-C.; Chen, C.-A.; Chang, C.-Y.; Darling, S. B.; Su, W.-F. *J. Mater. Chem. A* **2014**, *2*, 8026−8032.
[46] Lei, T.; Dou, J.-H.; Ma,Z.-J.; Yao, C.-H.; Liu, C.-J. Wang, J.-Y.; Pei, J. *J. Am. Chem. Soc*. **2012**, *134*, 20025−20028.
[47] Lei, T.; Dou, J.-Hu.; Ma, Z.-J.; Liu, C.-J.; Wang, J.-Y. Pei, *Chem. Sci*. **2013**, *4*, 2447–2452.
[48] Mei, J.; Kim, D. H.; Ayzner, A. L.; Toney, M. F.; Bao, Z. *J. Am. Chem. Soc.* **2011**, *133*, 20130–20133.
[49] Lei, T.; Dou, J. -H.; Pei, J. *Adv. Mater.* **2012**, *24*, 6457–6461.
[50] Dutta, G. K.; Han, A. -R.; Lee, J.; Kim, Y.; Oh, J. H.; Yang, C. *Adv. Funct. Mater*. **2013**, *23*, 5317–5325.
[51] Hasegawa, T.; Ashizawa, M.; Hiyoshi, J.; Kawauchi, S.; Mei, J.; Bao, Z.; Matsumoto, H. *Polym. Chem.* **2016**, *7*, 1181–1190.
[52] Lee, D. J.; Kim, K.; Park, Y. J. *Org. Lett*. **2002**, *4*, 873–876.
[53] Flores, J-C.; Berens, U.; Bienewald, F.; Kirner, H. J.; Turbiez, M. G. R. 2011, J**P2**011–501451A.
[54] Ashraf, R. S.; Kronemeijer, A. J.; James, D. I.; Sirringhaus H.; McCulloch, I.; *Chem. Commun*. **2012**, *48*, 3939–3941.
[55] Koizumi, Y.; Ide, M.; Saeki, A.; Vijayakumar, C.; Balan, B.; Kawamoto, M.; Seki, S. *Polym. Chem*. **2013**, *4*, 484–494.
[56] Van Pruissen, G. W. P.; Gholamrezaie, F.; Wienk, M. M.; Janssen, R. A. J. *J. Mater. Chem*. **2012**, *22*, 20387–20393.
[57] Karakawa, M.; Aso, Y. *RSC Adv*. **2013**, *3*, 16259–16263.
[58] Odajima, T.; Ashizawa, M.; Konosu, Y.; Matsumoto, H.; Mori, T. *J. Mater. Chem. C* **2014**, *2*, 10455–10467.
[59] Lu, C.; Chen, H. -C.; Chuang, W.-T.; Hsu, Y.-H.; Chen, W.-C.; Chou, P.-T. *Chem. Mater*. **2015**, *27*, 6837−6847.
[60] Kim, G.; Kang, S.-J.; Dutta, G. K.; Han, Y.-K.; Shin, T. J.; Noh, Y. -Y.; Yang, C. *J. Am. Chem. Soc*., **2014**, *136*, 9477–9483.
[61] Kim, G.; Kim, H.; Jang, M.; Jung, Y. K.; Oh, J. H.; Yang, C. *J. Mater. Chem. C* **2016**, *4*, 9554−9560.
[62] Ide, M; Koizumi, Y.; Saeki, A.; Izumiya, Y.; Ohkita, H.; Ito, S.; Seki, S. *J. Phys. Chem. C* **2013**, *117*, 26859−26870.
[63] Lu, C.; Chen, H. -C.; Chuang, W.-T.; Hsu, Y.-H.; Chen, W.-C.; Chou, P.-T. *Chem. Mater*. **2015**, *27*, 6837−6847.
[64] Kotlarski, J. D.; Blom, P. W. M. *Appl. Phys. Lett*. **2012**, *100*, 013306/1−013306/3.
[65] Horowitz, G. *Adv. Mater*. **1998**, *10*, 365−377.
[66] Dimitrakopoulos, C. D.; Malenfant, P. R. L. *Adv. Mater*. **2002**, *14*, 99−117.
[67] Blom, P. W. M.; de Jong, M. J. M.; Vleggaar, J. J. M. *Appl. Phys. Lett*. **1996**, *68*, 3308–3310.
[68] Labban, A. E.; Warnan, J.; Cabanetos, C.; Ratel, O.; Tassone, C.; Toney, M. F.; Beaujuge, P. M. *ACS Appl. Mater. Interfaces* **2014**, *6*, 19477−19481.
[69] Mikie, T.; Saeki, A.; Ikuma, N.; Kokubo, K.; Seki, S. *ACS Appl. Mater. Interfaces* **2015**, *7*, 12894−12902.
[70] Jung, I. H.; Lo, W. -Y.; Jang, J.; Chen, W.; Zhao, D.; Landry, E. S.; Lu, L.; Talapin, D. V.; Yu, L. *Chem. Mater.* **2014**, *26*, 3450−3459.

[71] Guo, X.; Zhou, N.; Lou, S. J.; Smith, J.; Tice, D. B.; Hennek, J. W.; Ortiz, R. P.; Navarrete, J. T. L.; Li, S.; Strzalka, J.; Chen, L. X.; Chang, R. P. H.; Facchetti, A.; Marks, T. J. *Nature Photo*. **2013**, *7*, 825–833.

[72] Tsoi, W. C.; Spencer, S. J.; Yang, L.; Ballantyne, A. M.; Nicholson, P. G.; Turnbull, A.; Shard, A. G.; Murphy, C. E.: Bradley, D. D. C.; Nelson, J.; Kim, J.-S. *Macromolecules* **2011**, *44*, 2944–2952.

[73] Kohn, P.; Rong, Z.; Scherer, K. H.; Sepe, A.; Sommer, M.; Müller-Buschbaum, P.; Friend, R. H.; Steiner, U.; Hüttner, S. *Macromolecules* **2013**, *46*, 4002−4013.

[74] Mauer, R,; Kastler, M.; Laquai, F. *Adv. Funct. Mater*. **2010**, *20*, 2085–2092.

[75] Guo, J.; Ohkita, H.; Benten, H.; Ito, S. *J. Am. Chem. Soc*. **2009**, *131*, 16869–16880.

[76] Guo, J.; Ohkita, H.; Benten, H.; Ito, S. *J. Am. Chem. Soc*. **2010**, *132*, 6154–6164.

[77] Hwang, I.-W.; Soci, C.; Moses, D.; Zhu, Z.; Waller, D.; Gaudiana, R.; Brabec, C. J.; Heeger, A. J.; *Adv. Mater*. **2007**, *19*, 2307–2312.

[78] Jarzab, D,; Cordella, F.; Gao, J.; Scharber, M.; Egelhaaf, H.-J. Loi, M. A. *Adv. Energy Mater*. **2011**, *1*, 604–609.

[79] Yamamoto, S.; Ohkita, H.; Benten, H.; Ito, S. *J. Phys. Chem. C* **2012**, *116*, 14804−14810.

[80] Etzold, F.; Howard, I. A.; Forler, N.; Cho, D. M.; Meister, M.; Mangold, H.; Shu, J.; Hansen, M. R.; Müllen, K.; Laquai, F. *J. Am. Chem. Soc.* **2012**, *134*, 10569−10583.

[81] Chow, P. C. Y.; Gelinas, S.; Rao, A.; Friend, R. H. *J. Am. Chem. Soc*. **2014**, *136*, 3424−3429.

[82] Zusan, A.; Gieseking, B,; Zerson, M.; Dyakonov, V.; Magerle, R.; Deibel, C. *Sci. Rep*. **2015**, *5*, 08286.

[83] Kraus, H.; Heiber, M. C.; Väth, S.; Kern, J.; Deibel, C.; Sperlich, A.; Dyakonov, V. *Sci. Rep*. **2016**, *6*, 29158.

[84] Seki, S.; Saeki, A.; Sakurai, T.; Sakamaki, D. *Phys. Chem. Chem. Phys.* **2014**, *16*, 11093−11113.

[85] Grozema, F. C.; Siebbeles, L. D. A. *J. Phys. Chem. Lett*. **2011**, *2*, 2951–2958.

[86] Saeki, A.; Tsuji, M.; Seki, S. *Adv. Energy Mater*. **2011**, *1*, 661–669.

[87] Saeki, A.; Fukumatsu, T.; Seki, S. *Macromolecules* **2011**, *44*, 3416–3424.

[88] Saeki, A.; Yoshikawa, S.; Tsuji, M.; Koizumi, Y.; Ide, M.; Vijayakumar, C.; Seki, S. *J. Am. Chem. Soc*. **2012**, *134*, 19035−19042.

[89] Tumbleston, J. R.; Collins, B. A.; Yang, L.; Stuart, A. C.; Gann, E.; Ma, W.; You, W.; Ade, H. Nat. Photo. 2014, 8, 385−391.

[90] Ayzner, A.; Nordlund, D.; Kim, D.-H.; Bao, Z.; Toney, M. F. *J. Phys. Chem. Lett.* **2015**, *6*, 6−12.

[91] Szumilo, M. M.; Gann, E. H.; McNeill, C. R.; Lemaur, V.; Oliver, Y.; Thomsen, L.; Vaynzof, Y.; Sommer, M.; Sirringhaus, H. *Chem. Mater*. **2014**, *26*, 6796−6804.

[92] Jakowetz, A. C.; Böhm, M. L.; Zhang, J.; Sadhanala, A.; Huettner, S.; Bakulin, A. A.; Rao, A.; Friend, R. H. *J. Am. Chem. Soc*. **2016**, *138*, 11672−11679.

[93] Son, S. Y.; Kim, Y.; Lee, J.; Lee, G.-Y.; Park, W.-T.; Noh, Y.-Y.; Park, C. E.; Park, T. *J. Am. Chem. Soc*. **2016**, *138*, 8096−8103.

[94] Liu, F.; Zhao, W.; Tumbleston, J. R.; Wang, C.; Gu, Y.; Wang, D.; Briseno, A. L.; Ade, H.; Russell, T. P. *Adv. Energy Mater*. **2014**, *4*, 1301377, 1-9.

[95] Guo, Z.; Lee, D.; Schaller, R. D.; Zuo, X.; Lee, B.; Luo, T.; Gao, H.; Huang, L. *J. Am. Chem. Soc.* **2014**, *136*, 10024−10032.

[96] Osaka, I.; Saito, M.; Koganezawa, T.; Takimiya, K. *Adv. Mater.* **2014**, *26*, 331–338.

[97] Wang, M.; Wang, H.; Yokoyama, T.; Liu, X.; Huang, Y.; Zhang, Y.; Nguyen, T.-Q.; Aramaki, S.; Bazan, G. C. *J. Am. Chem. Soc.* **2014**, *136*, 12576–12579.

Chapter 2: Thienoisoindigo-Based Low-Band Gap Polymer

2-1. Introduction

Low-band gap copolymers are particularly important because of their ability to absorb in a broad range of wavelengths including visible, near infra-red (NIR), and infra-red regions of the solar spectrum. One of the most popular strategies for achieving low-band gap in polymers was to utilize the internal charge transfer interactions through the incorporation of rationally selected of donor and acceptor moieties to the polymer backbone in an alternating fashion.[1]

Isoindigo (IDG) is a relatively new molecular unit with strong electron accepting properties and intense absorption characteristics used for the development of organic electronic materials.[2] The presence of strong electron donors in conjugation can induce charge transfer interactions in isoindigo derivatives, which increases the absorption intensity and push the absorption band to the near infra-red region[3]. Recent reports suggests that organic electronic and optoelectronic devices with good efficiencies could be fabricated by using isoindigo based polymer[4] and oligomers.[5] For instance, bithiophene-IDG copolymer (IIDDT) exhibited hole mobility as high as 0.79 $cm^2\ V^{-1}\ s^{-1}$.[6] Benzodithiophene-thiophene-IDG copolymer (PBDT-TIT) also showed high PCE of 5.4%.[7] The highest PCE of IDG copolymer bearing non-halogenated IDG reported so far is 6.6 % realized by terthiophene-IDG copolymer (**P3**TI).[8] Recently fluorinated IDG copolymer has been evaluated and reached 7.0% PCE with benzodithiophene introduced thiophene as the side chain.[9] There are many more examples of IDG-based copolymers in combination with thiophene, fluorene, and phenyl groups.[4,10]

In this chapter, the author summarizes the synthesis of a series of new copolymers with extremely low-band gaps consisting of TIDG in conjunction with typical donor units such as benzodithiophene (BDT), cyclopentadithiophene (CPDT), fluorene (FLO), and dithienothiophene (DTT). Their optical and electronic properties were investigated and discussed using ultraviolet photoelectron spectroscopy, optical spectroscopy, FET analysis, and density functional theory (DFT).[11]

2-2. Synthesis of TIDG copolymers

The synthetic scheme for monomers and polymers were illustrated in Schemes 1 through 4.

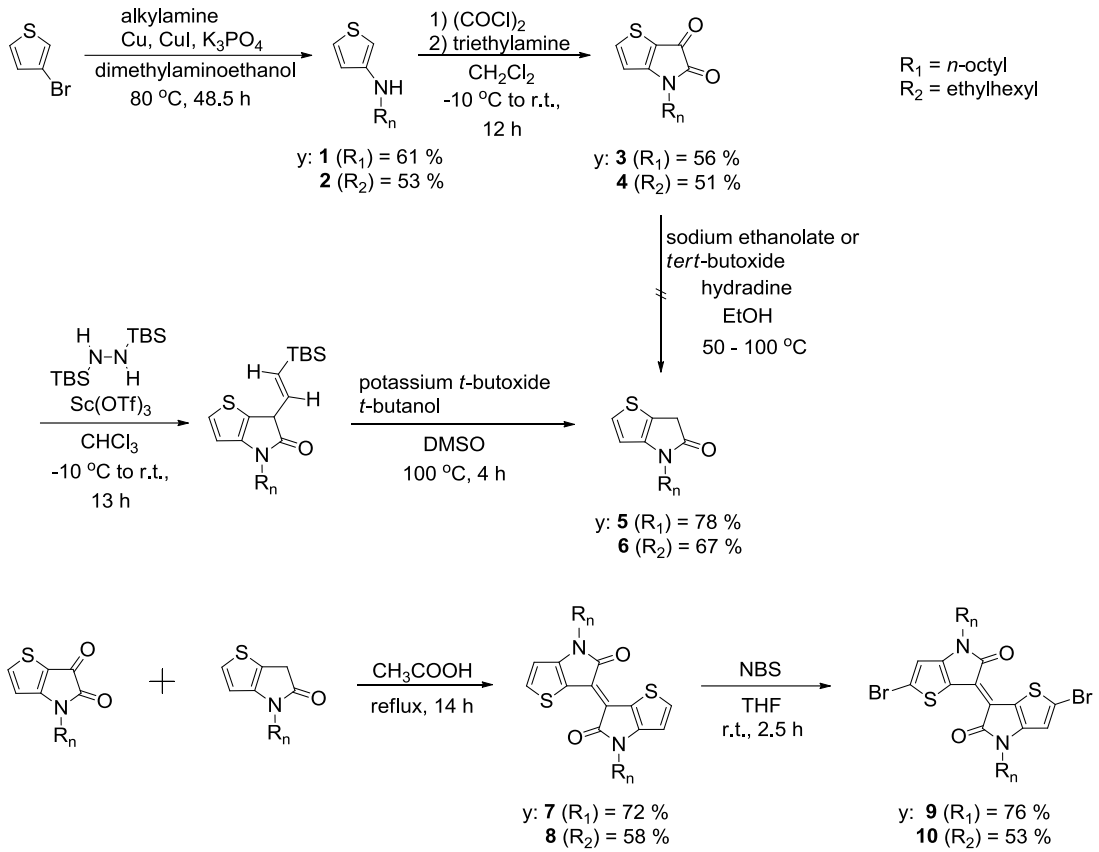

Scheme 1. Synthetic scheme for TIDG monomers. Reproduced from ref 11 with permission from the Royal Society of Chemistry.

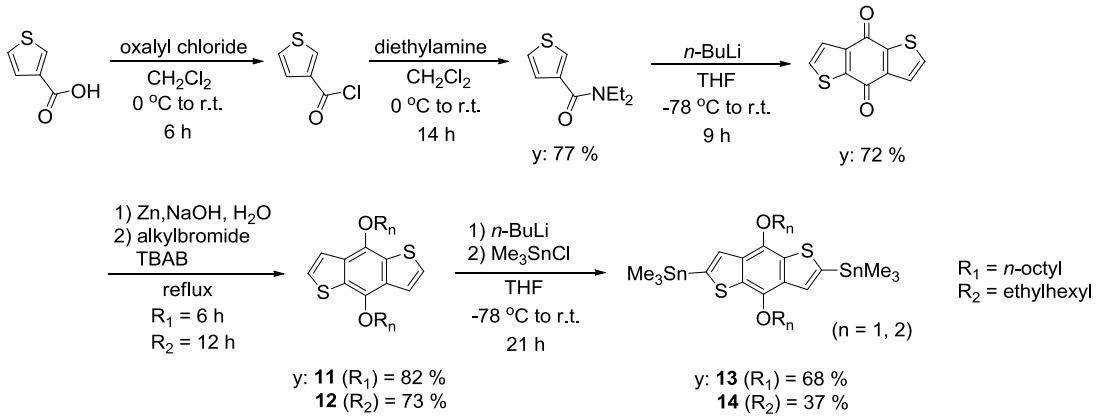

Scheme 2. Synthetic scheme for BDT monomers. Reproduced from ref 11 with permission from the Royal Society of Chemistry.

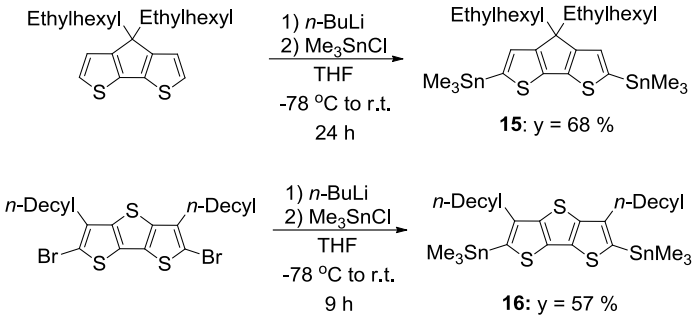

Scheme 3. Synthetic scheme for donor monomers. Reproduced from ref 11 with permission from the Royal Society of Chemistry.

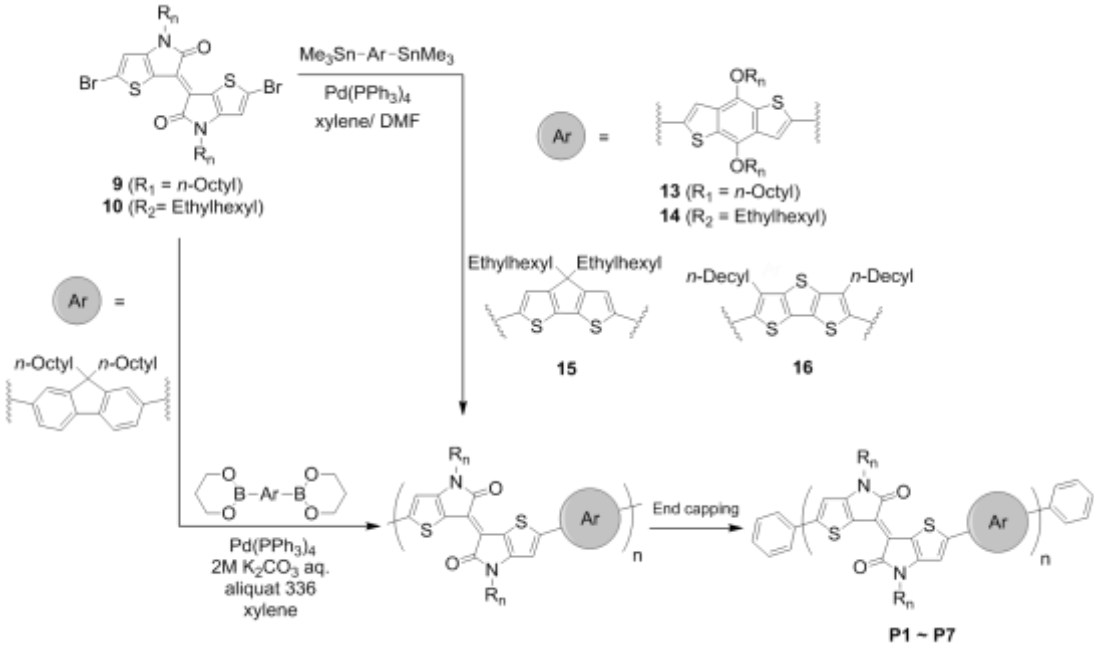

Scheme 4. Synthetic scheme for the copolymer **P1** through **P7**. Reproduced from ref 11 with permission from the Royal Society of Chemistry.

To ensure the solubility, *n*-octyl or branched 2-ethylhexyl side chains were attached to the nitrogen atom of 4,4'-bis(alkyl)-[6,6'-bithieno[3,2-b]pyrrolylidene] -5,5'(4*H*,4'*H*)-dione accepter monomer units. Starting from commercially available 3-bromothiophene, the alkylated thiophen-3-amine monomer **1** and **2** were obtained with 61 % and 53 % yields, respectively.[12] These schemes indicate two cautions: (1) in this copper-catalyzed amination in deanol, deanol byproduct was easily produced without vigorous stirring, and (2) monomer **1** and **2** quickly decomposed in presence of light and air. After the cyclization of these monomers, alkylated-4*H*-thieno[3,2-*b*] pyrrole-5,6-dione monomer **3** and **4** were obtained with 56 % and 51 % yields,

respectively. These monomers show good stability against the exposure to light and air. The author used the hydrazine reagent, 1,2-bis(tert-butyldimethylsilyl)hydrazine (BTBSH) for present Wolff-Kisher type reduction. BTBSH was prepared according to the literature method.[13] The hydrazone intermediate appended with BTBSH shows higher stability than the hydrazone intermediate prepared by the patented method,[14] as evident from the absence of de-cyclization even after heating up to 100 ˚C with strong base. Wolff-Kisher type reduction was monitored by TLC and ^{1}HNMR analysis. As a consequence, the alkylated-4*H*,6*H*-thieno[3,2-*b*]pyrrole-5-one monomer **5** and **6** were obtained as pale-yellow compounds with moderate yields of 78 % and 67 %, respectively. The monomer color, however, turned slowly to red, because of the decomposition even under ambient conditions. After the coupling reaction of alkylated-4*H*-thieno [3,2-*b*]pyrrole-5,6-dione and alkylated-4*H*,6*H*-thieno[3,2-*b*]pyrrole -5-one, the obtained monomers **7** and **8** were brominated and (*E*)-2,2'-dibromo -4,4'-bis(alkyl)-[6,6'-bithieno [3,2-b]pyrrolylidene]-5,5'(4*H*,4'*H*)-dione **9** and **10** were successfully obtained as a wine-red solid with 76 % and 53 % yields, respectively. The stanylbenzodithiophene monomers **13** and **14** were prepared according to the literature.[15] The stanyl-CPDT and DTT monomers **15** and **16** were also synthesized by following the reported procedure.[16,17] The polymerization were carried out under Stille cross coupling reactions or Suzuki-Miyaura cross coupling with 1:1 monomer ratio, using tetrakis(triphenylphosphine)palladium: $Pd(PPh_3)_4$ as the catalyst to give a green material. The crude copolymers were purified by passing through a column filled with metal removal silica gel and followed by precipitation from chloroform solution by adding methanol or acetone to yield grass green colored solids. Chemical structures of copolymers are shown in Figure 13. Copolymer **P1**, **P2**, and **P3** were soluble in common organic solvent like chloroform, chlorobenzene, and *o*-dichlorobenzene. Copolymer **P4** and **P7** were soluble in chloroform. On the other hand, the high molecular weight part of the copolymer **P5** was insoluble in any solvent and therefore only the oligomer component was purified. Copolymer **P6** containing TIDG unit with all *n*-octyl side chains was not soluble in any solvents. The chemical structures of the copolymers were verified by ^{1}HNMR spectroscopy. The weight-averaged molecular weights (M_w), number-averaged molecular weights (M_n), and polydispersity indices (PDI) of the copolymers as listed in Table 1 were determined by gel permeation chromatography (GPC) at 40 ˚C using polystyrenes as standards with tetrahydrofuran (THF) as eluent. All copolymers show strong intermolecular interaction and aggregation in THF. Thus it was necessary to prepare dilute solutions for the determination of accurate M_w and M_n reflecting the single polymer chain.

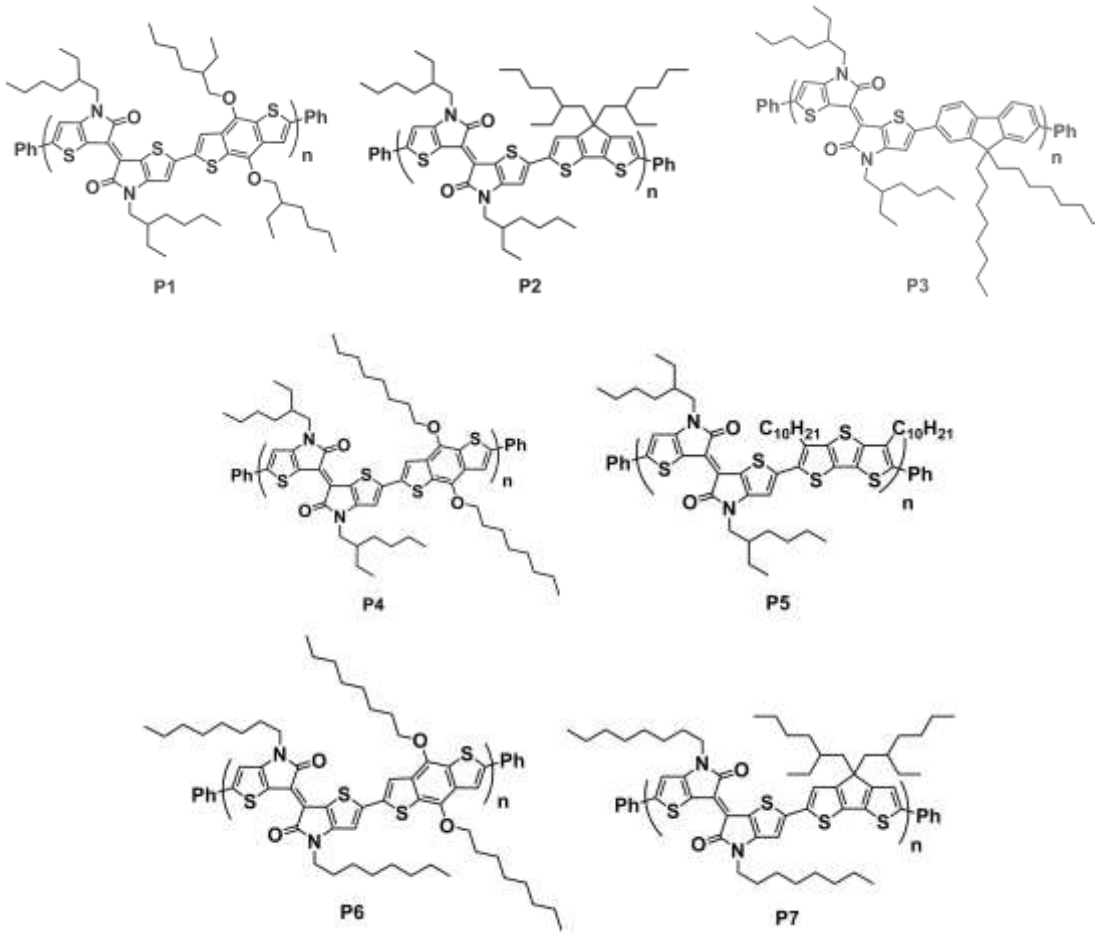

Figure 13. Chemical structures of TIDG copolymers. Reproduced from ref 11 with permission

2-3. Optical and electronic properties of TIDG copolymers

2-3-1. Polymer thermal stability

Thermal stability of polymers is a very important criterion for their use in electronic devices. Thermal analysis of the copolymers was carried out by differential scanning calorimetry (DSC) at a temperature ramp rate of 10 ˚C min^{-1}. DSC thermograms of **P1**, **P2**, and **P3** were featureless from 25 to 300 ˚C, providing no evidence of any phase transitions. This result indicates that these polymers have good thermal stability, suitable for robust organic electronic devices.

2-3-2. Optical properties.

Electronic absorption spectra of polymers in the chloroform solutions and drop-casted films were measured, and the details were summarized in Table 1. All polymers exhibited two characteristic absorption bands consisting of a sharp one at the

high energy region (350 - 550 nm) and a more intense, broader one at the low energy region (600 - 1400 nm). Molecular calculations using density functional theory (DFT, B3LYP/6-31G(d,p)) revealed that the polymer absorption consists of two distinct $\pi-\pi^*$ transitions. The lower energy band corresponds to the transition from ground state to first excited state (S_0-S_1), whereas that of the higher energy one corresponds to the transition from ground state to third excited state (S_0-S_3). The absorption spectra of **P1**-**P3** in chloroform solution are shown in Figure 14(a), which was in good agreement with that obtained from DFT calculation. The S_0-S_3 transitions of all three polymers were having similar features with absorption maximum at 434, 460, and 410 nm for **P1**, **P2**, and **P3** respectively. Interestingly, the absorption features of **P1** and **P2** corresponding to the S_0-S_1 transition (λ_{max} = 859, 971 nm respectively) are significantly different from that of the **P3** polymer (λ_{max} = 745 nm). Both **P1** and **P2** absorptions were broad and intense with highly red-shifted absorption maximum when compared to that of **P3**. Due to the broad and red-shifted nature, the absorption of **P1** and **P2** extends to NIR and IR regions, whereas that of **P3** is well within the visible region. Moreover, **P3** exhibit well resolved vibronic features implying the absence of any inter or intra polymer electronic interactions in the ground state. The nature of the absorption spectra of **P1** and **P2** at longer wavelengths indicates the possibility of internal charge transfer (ICT) states in these polymers and the absorption corresponding to the ICT state might be merged with the S_0-S_1 absorption peaks. It is known that the electron donating abilities of the donor chromophores increases in the order of FLO < BDT < CPDT.[18] Fluorene is a very weak donor and might be difficult to form ICT with TIDG acceptor. On the other hand, both BDT and CPDT are strong donors and efficiently form CT

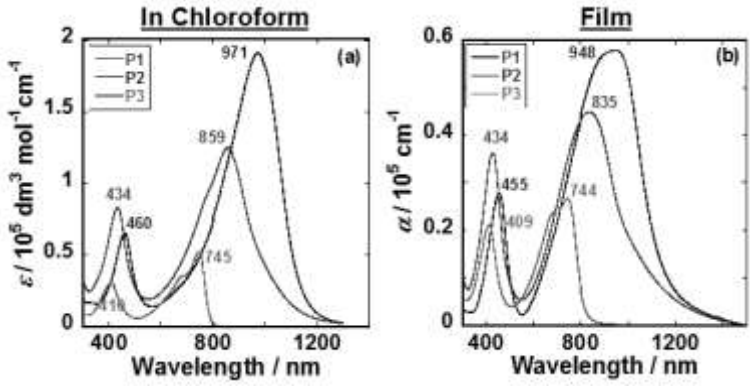

Figure 14. (a) Electronic absorption spectra of **P1** (red line), **P2** (blue line), and **P3** (green line) in chloroform at 7.86×10^{-6}, 4.95×10^{-6}, and 8.36×10^{-6} mol dm^{-3} at room temperature, respectively. (b) Electronic absorption spectra of **P1**, **P2**, and **P3** as films drop-cast from chloroform solutions. Reproduced from ref 11 with permission from the Royal Society of Chemistry.

complexes with the acceptor.

The absorption spectra of **P1**-**P3** in the film state were shown in Figure 14(b) In the case of **P1** and **P2**, the absorption at longer wavelengths showed a blue-shift of 24 nm and 23 nm respectively, when compared to that of the solution state. Similarly, the oscillator strength of the longer wavelength peak relative to the lower one was also decreased in the film state. On the other hand, no blue-shift was observed in the case of **P3** in film state. In addition to that, the relative oscillator strength of the two peaks was remained more or less same. This observation further reiterates that CT complexes were formed in **P1** and **P2**, and it was absent in **P3**. Since the CT state was highly sensitive to the environment, loss of solvation energy due to the absence of solvent could destabilizes the CT state, resulting in blue-shift of the absorption maximum and reduction of the oscillator strength. However, the onset of the absorption has red-shifted by 50 nm in **P3** and by 100 nm in **P1** and **P2** which could be attributed to the enhanced planarization and/or stacking of the copolymers in the film state. The relatively smaller shift of the onset for **P3** suggests poor stacking in these copolymers than that of **P1** and **P2**. This could be due to steric hindrance exerted by the alkyl chains at 9-position of the fluorene, which occupies orthogonal to the polymer π-plane.

Table 1. Optical, electrochemical, and polymeric properties of **P1** through **P7**.

Polymer	M_w / kg mol^{-1} [a]	M_n/ kg mol^{-1} [a]	PDI[a]	HOMO/ eV[b]	λ_{max} solution/ nm[c]	λ_{max} film/ nm	E_g^{opt}/ eV[d]	LUMO/eV[e]
P1	88.3	39.9	2.2	-4.9	434, 859	427, 835	1.1	-3.8
P2	15.0	8.6	1.7	-4.8	460, 971	455, 948	1.0	-3.8
P3	24.0	10.0	2.3	-5.4	410, 745	409, 744	1.6	-3.8
P4	11.8	5.7	2.1	-4.8	425, 788	422, 759	1.3	-3.5
P5	3.0	1.7	1.8	-5.0	417, 745	430, 705	1.1	-3.9
P6	-	-	-	-	425, 784	-	-	-
P7	13.4	7.4	1.8	-	464, 1005	459, 980	1.0	-

[a] Determined by GPC using polystyrene standards in THF as eluent. [b] Determined by UPS of the films. [c] chloroform solution. [d] Determined from the onset of the electronic absorption spectra. [e] HOMO+E_g^{opt} .

The optical band gap energies (E_g^{opt}) of the copolymers were estimated from the onset of the absorption spectra of film state. All copolymers exhibited E_g^{opt} ranging between 1.0 to 1.6 eV, and the details were summarized in Table 1. E_g^{opt} of **P1** - **P3** were found to be 1.1, 1.0 and 1.6 eV, which were much smaller than that of regioregular poly(3-hexylthiophene): P3HT (1.9 - 2.0 eV). Such low-band gaps in **P1** and **P2** could be attributed to the presence of ICT state. It must be noted that even in the case of **P3**,

where ICT state is absent, the optical band gap is significantly low, indicating the usefulness of TIDG as an acceptor unit for the development of p-type polymers for OPV.

2-3-3. Electrochemical characterization

It is well-recognized that organic semiconducting materials should have delocalized electron-density-state and appropriate levels of HOMO and LUMO to facilitate efficient transport of hole and electron, respectively. The HOMO levels of polymers were measured as the ionization threshold energy by UV photoelectron spectroscopy (UPS) and summarized in Table 1. The ionization energies were estimated as -4.9 eV, -4.8 eV, and -5.4 eV for **P1**, **P2**, and **P3**, respectively. For comparison, the ionization energy of P3HT was also measured and it was found to be -4.7 eV. The LUMO levels of the copolymers were estimated by adding E_g^{opt} to HOMO, as listed in Table 1. The energy diagrams of **P1** through **P3** and $PC_{61}BM$ are shown in Figure 15. All new copolymers demonstrate deeper HOMO levels than that of P3HT, which is beneficial for obtaining improved open-circuit voltage for the OPV devices.

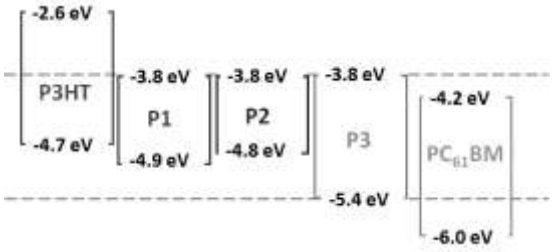

Figure 15. Energy diagram for TIDG copolymers, P3HT and $PC_{61}BM$. Reproduced from ref 11 with permission from the Royal Society of Chemistry.

2-3-4. Density functional theory (DFT) calculation

To provide more insight into the structural and electronic features of the copolymers, distribution of the HOMO and LUMO orbitals of **P1**-**P3** were calculated using DFT method at the B3LYP/6-31G(d) level and shown in エラー! 参照元が見つかりません。. Interestingly, the HOMO is mostly distributed along the polymer backbone, whereas the LUMO is localized on the TIDG moiety. This is consistent with the HOMO-LUMO distribution observed in several p-type donor-acceptor copolymers. Among the copolymers, better delocalization of HOMO was obtained for **P2**, which is in accordance with its extended electronic absorption spectrum. DFT calculations were also carried out to compare the planarity of the IDG and TIDG containing polymer backbones. The optimized structures of BDT-IDG-BDT and BDT-TIDG-BDT trimers were also presented in エラー! 参照元が見つかりません。. Their structures from the horizontal view clearly indicate that the backbone of TIDG-containing oligomer has

more planar structure than that of IDG-containing oligomer. As mentioned in the introduction, the steric effect exerted between the proton on the phenyl ring and carbonyl oxygen is responsible for the twist in the IDG unit, which is absent in the case of TIDG. Accordingly, it is clear that the red-shift in the absorption maximum as well as the absorption intensities of the longer wavelength bands were directly proportional to the strength donor moieties in these polymers (エラー! 参照元が見つかりません。). Further insights into the optical properties were obtained from the optimized geometry calculations using DFT method. It revealed that the dihedral angle between CPDT and TIDG is < 0.04˚ (**P2**), while that between BDT and TIDG is 7 ~ 12˚ (**P1**). Higher planarity between the donor and acceptor moieties in **P2** also contributed to its red-shifted absorption maximum relative to that of **P1**. In addition, the large dihedral angle of 23˚ between BDT and IDG was reduced to 7 ~ 12˚ by replacing IDG with TIDG. These observations revealed the superiority of TIDG over IDG for obtaining low-band gap copolymers with better planarity and extended conjugation length.

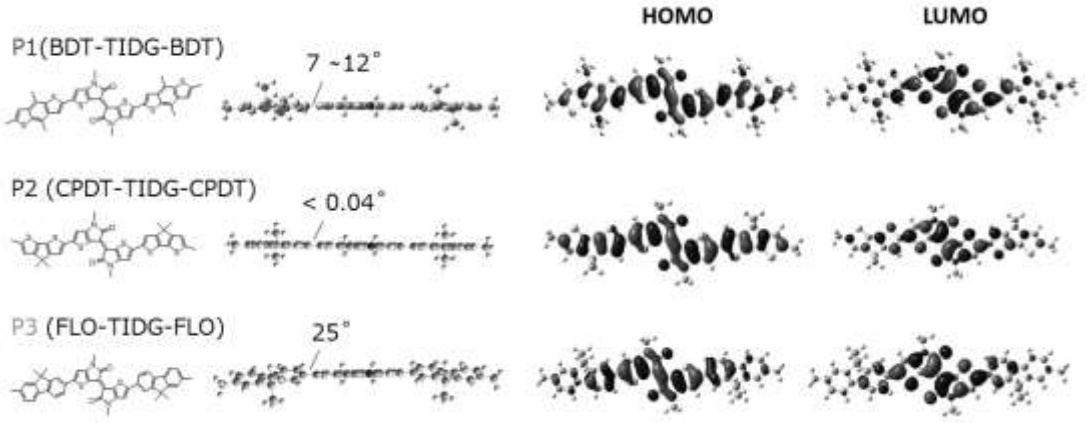

Figure 16. Optimized geometry of trimers of **P1** through **P3** obtained by DFT calculation using the B3LYP/6-31G(d) level. The alkyl chains are replaced with methyl groups for simplicity. Reproduced from ref 11 with permission from the Royal Society of Chemistry.

2-4. Hole mobility measurement by field effect transistor

The semiconducting properties of copolymers were characterized in bottom-gate/top-contact FET devices. They were fabricated by spin-coating onto a SiO_2 (200 nm)/n-doped Si substrate, where n-doped Si and SiO_2 were used as the gate electrode and dielectric insulator, respectively. In this work, copolymer films were dried under vacuum and measured before and after thermal annealing at 160 ^{o}C for 10 min. Figure 17 shows the transfer curves at a drain–source voltage (V_{DS}) of -100 V or -90 V

and output curves at a gate voltage of 0 to -100 V or 0 to -80 V. All copolymers showed p-channel FET characteristics, which is consistent with the DFT results. The hole mobility (μ_{hole}) was obtained from the saturated regime and the values are listed in Table 2. The hole mobilities were increased in the order of **P1** < **P3** < **P2**. The CPDT-TIDG copolymer (**P2**) showed the highest hole mobility of 5.3 $\times$ 10^{-3} cm^2 V^{-1} s^{-1}, reflecting the delocalization of HOMO on the planar backbone structure and consequent good intermolecular overlap of the π-orbitals. Atomic force microscopy (AFM) images of the films are shown in Figure 18, in which fiber-like morphologies are manifested in the order of **P1**, **P2**, and **P3** with surface roughness of 1.4, 1.0, and 0.47 nm, respectively. This is consistent with the more pronounced intermolecular stacking in **P1** and **P2** than **P3** suggested from optical spectroscopy and DFT calculation.

Table 2. Bottom gate/top contact field-effect transistor performance for copolymers **P1**, **P2** and **P3**. [a] No thermal annealing, channel length (L): 100 mm. [b] Thermal annealing at 160 °C for 10 min, channel length (L): 20 mm. [c] No thermal annealing, channel length (L): 20 mm. Reproduced from ref 11 with permission from the Royal Society of Chemistry.

Polymers	μ_{hole}/ 10^{-3} cm^2 V^{-1} s^{-1}	L/ μm	V_t/ V	I_{on} / I_{off}	R_a/ nm[d]	Thickness / nm
P1[a]	0.34	100	-22.5	10^2	1.4	76
P2[b]	5.3	20	33.6	10^1	1.0	68
P3[c]	1.7	20	-23.0	10^5	0.47	100

In particular, the hole mobility of **P2** was increased twice by thermal annealing compared with that without annealing. This trend was observed as well for the IDG containing copolymer.[6] The hole mobility of the BDT-TIDG (**P1**) copolymer was still two orders of magnitude smaller than that of BDT-IDG copolymers, where the latter were implemented by octadecyltrimethoxysilane (OTS) surface treatment, the use of trichloroethylene (TCE) as a solvent, and slow drying under TCE vapor.[16] So far there are few choices of the solvent for our copolymers because of the in sufficient solubility. However, it can be addressed by fine-tuning of the side chain and we believe that the mobilities would be further improved to make these polymers suitable for photovoltaic device applications.

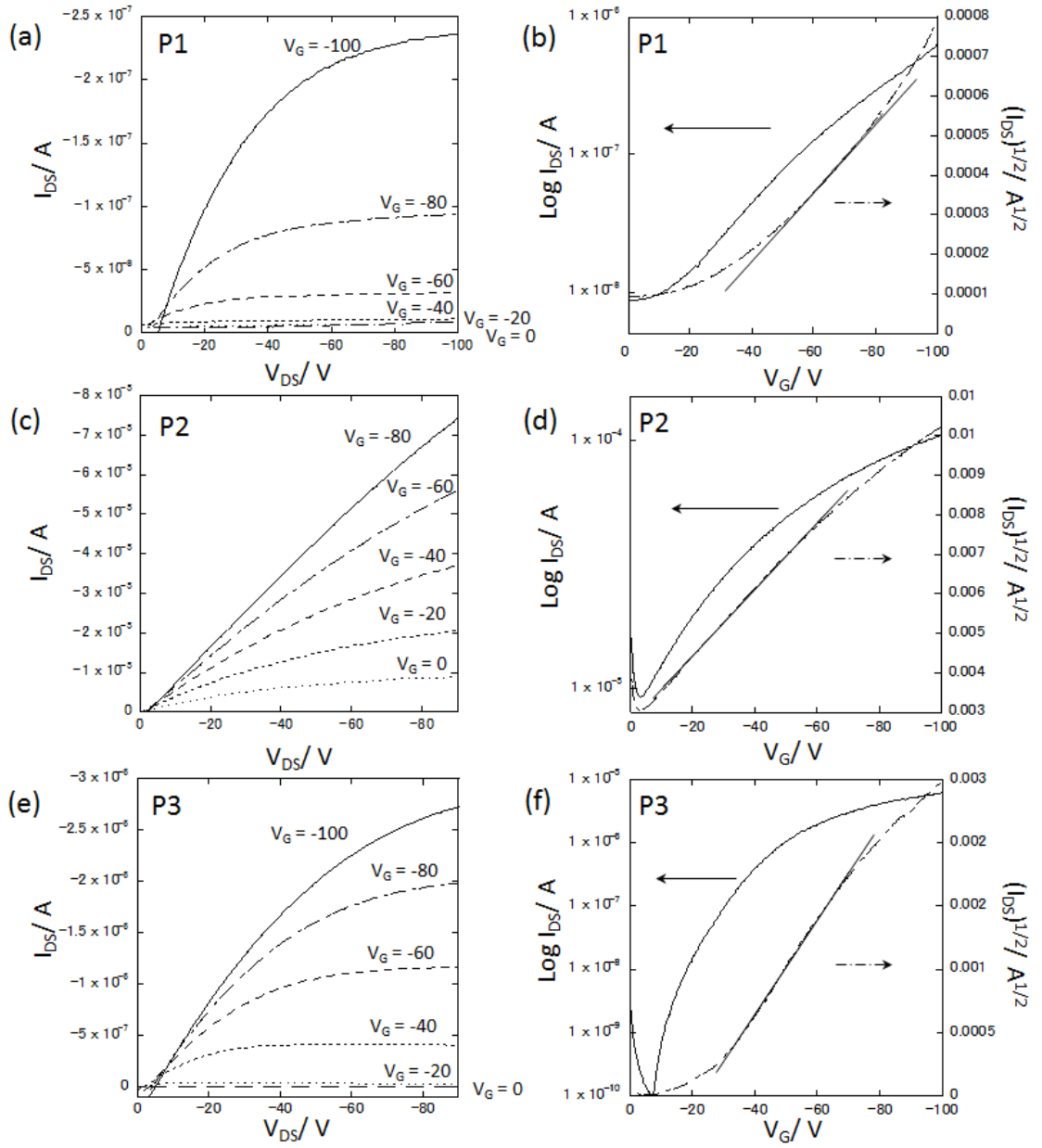

Figure 17. FET current-voltage characteristics of (a)(b) **P1**, (c)(d) **P2**, and (e)(f) **P3** copolymer (a),(c), and (e) are output curves at different gate voltages (0 to - 100 V or -80 V); (b),(d), and (f) are transfer curves at V_{DS} = -100 V for **P1** and **P3**, -80 V for **P2**. The channel length: L were 100, 20, and 20 μm for **P1**, **P2**, and **P3**, respectively; the channel width: *W* was 3 mm, and the film thicknesses were 68 ~ 100 nm. The capacitance: C_i was 17.3 nF cm-2. The measurements were carried out at room temperature. The hole mobilities of 0.34 × 10^{-3}, 5.3 × 10^{-3}, and 1.1 × 10^{-3} cm^2 V^{-1} s^{-1} were obtained for **P1**, **P2**, and **P3**, respectively, from the slopes of square-root of the drain current vs. V_G. Reproduced from ref 11 with permission from the Royal Society of Chemistry.

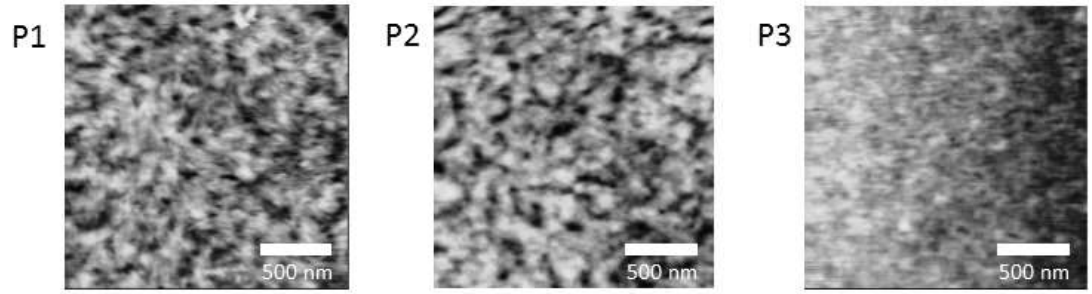

Figure 18. AFM micrographs of **P1**, **P2**, and **P3**. The sample films were prepared by spin-casting from chloroform solution for **P1** and **P3**, chlorobenzene solution for **P2**, then dried under vacuum. Films of **P1** and **P3** were no thermal annealing, that of **P2** was thermal annealed at 160 °C for 10 min. All images are 2 × 2 μm scale. The surface roughness are (**P1**) 1.4 nm, (**P2**) 1.0 nm, and (**P3**) 0.47 nm. Reproduced from ref 11 with permission from the Royal Society of Chemistry.

2-5. Application as ambipolar copolymer for all polymer solar cells

2-5-1. Introduction

Low band gap polymers are particularly important because of their feasibility to cover the broad range of wavelength including NIR and IR regions of the solar spectrum. Many p-type copolymers mixed with fullerene derivatives represented by PCBM have been reported for OPVs. On the contrary, n-type copolymers, of which the electronic absorption properties are superior to fullerenes, are limited, because they have difficulties in accepting and transporting electrons in comparison with PCBM. In 2009, naphthalene-bis(dicarboximide) (NDI) based copolymer performed the high electron mobility by OFET,[19] and developed as the n-type semiconducting copolymers for all polymer solar cell.[20,21] Several copolymers have been investigated for the aim of wide absorption,[22] and the highest PCEs of all-polymer solar cells are 8.3% by benzodithiophene-*alt*-benzotriazole with fluorine substitution.[23]

The author reviewed TIDG copolymers in the previous section, and the deep LUMOs of TIDG copolymers at -3.8 eV are realized due to remarkable electron withdrawing nature. Therefore LUMOs of TIDG copolymers were located in between LUMOs of P3HT (-2.7 eV) and $PC_{61}BM$ (-4.0 ~ -4.2 eV) (Figure 15). The heightened LUMO of the TIDG copolymers compared to $PC_{61}BM$ could enhance the open circuit voltage (V_{oc}) in the bulk heterojunction (BHJ) with P3HT for all polymer solar cell.[24]

2-5-2. Optical and electronic properties

Among TIDG copolymers, fluorene-*alt*-TIDG (**P3**) copolymer was focused, since its HOMO (-5.4 eV) is deep enough to prevent the undesired hole transfer from HOMO of P3HT (-4.8 eV).[25] Furthermore, electronic absorption spectra of P3HT and **P3** are in the excellent complementary relationship (Figure 19). Prior to device fabrication, the author performed a laser and Xe-flash time-resolved microwave conductivity (TRMC)[26,27] measurements of **P3**:P3HT blends, which predicts the best p/n blend ratio and thermal annealing effects.

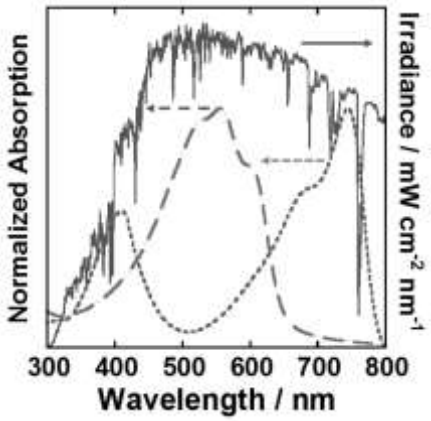

Figure 19. Normalized absorption spectra of P3HT (purple dashed line), **P3** (green dotted line), and solar spectrum (AM1.5G, gray solid line). Copyright 2013 The Society of Photopolymer Science and Technology. (ref 24)

The molecular weight of the repeating units in **P3** is 885 g mol^{-1}, leading to an

estimate of molar extinction coefficient (ε) of **P3** at the electronic absorption maximum of 745 nm as $5.2 \times 10^4\ M^{-1}\ cm^{-1}$ per a repeating unit. The constant observed for $PC_{61}BM$, as a typical n-type material, is less than $10^3\ M^{-1}\ cm^{-1}$ in the range of 700 ~ 800 nm, suggesting not only the complementary features of the electronic absorption spectrum of **P3** to cover the solar spectrum in combination with P3HT but also advantageous to effective harvesting of solar energy in substitution of $PC_{61}BM$ and fullerene derivatives.

2-5-3.Time-resolved microwave conductivity (TRMC) measurement for evaluation of blend ratio

On the basis of the quantitative analysis of the optical transitions for respective counterparts of **P3** and P3HT, the blend film of the polymers were prepared as models of active layers in OPVs and examined by TRMC measurements. Figure 20 plots the transient photoconductivity maxima ($\Delta\sigma_{max}$) of P3HT:**P3** films observed by Xe-flash TRMC at different annealing temperatures for 10 min. Apparently the annealing at both 120 and 160 ^oC gives a considerable increase in $\Delta\sigma_{max}$, and the highest $\Delta\sigma_{max}$ was observed at P3HT = 40 ~ 60 wt% irrespective of the thermal annealing. At the optimized concentration, the value of $\Delta\sigma_{max}$ becomes 2-fold after thermal annealing at 160 ^oC in comparison without thermal treatment. This suggests that the formation of appropriate BHJ network and enhanced intermolecular π-stacking of the polymers were promoted upon thermal annealing. Probably, P3HT and **P3** were homogenously mixed just after casting, which cannot provide efficient charge transport pathway. The benefit of thermal annealing has been also mentioned in other polymer:polymer solar cells.[21,28] From the process screening results by Xe-flash TRMC, it is suggested that the best PCE is obtained at p/n blend ratio of 1:1 with thermal annealing.

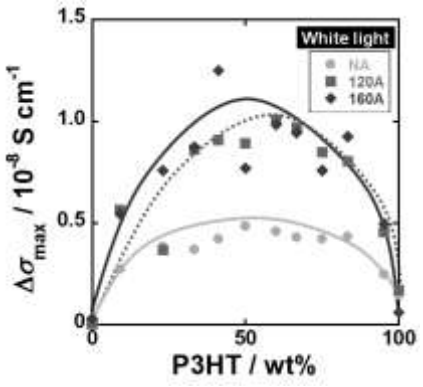

Figure 20. Xe-flash TRMC results of P3HT:**P3** blend films prepared by drop-casting chloroform: chlorobenzene = 1:1.5 w/w solutions. The NA (green circles), 120A (blue squares), and 160A (red diamonds) represent the non-thermal treatment, annealing at 120 ^oC for 10 min, and 160 ^oC for 10 min, respectively. Copyright 2013 The Society of Photopolymer Science and Technology. (ref 24)

Xe-flash TRMC provides overall optoelectronic property of BHJ film including spectrum match with the sunlight, charge carrier generation efficiency, local charge

carrier mobility, and its lifetime, which correlates well with the device performance.[27] To ascertain the charge carrier lifetime and the difference in the initial exciton formation in either P3HT or **P3** domains, the laser-flash TRMC experiments under the excitations at 500 and 680 nm were conducted. Figure 21a and Figure 21b show the $\Delta\sigma_{max}$ dependence as a function of P3HT fraction. The 500 nm excitation, attributed mainly to P3HT absorption, gave the almost similar trend with Xe-flash TRMC. This is due to that the light at ca. 500 nm is the main component of white light pulse. However, the thermal annealing did not provide a significant difference in $\Delta\sigma_{max}$ of laser-flash TRMC, in contrast to the results found in Xe-flash TRMC (Figure 20). This is suggestive of the increased lifetime of charge carrier by thermal annealing, which mediates phase separation between P3HT and **P3** and facilitates the formation of long-lived charge carriers.

At 680 nm which excites predominantly **P3** rather than P3HT, the peak position of $\Delta\sigma_{max}$ of laser-flash TRMC were shifted towards higher content of P3HT of around 80 ~ 90 wt%. This indicates that exciton formed in **P3** domain cannot smoothly migrate to the p/n interface and generate charge separated states. In other words, exciton diffusion length in **P3** is shorter than that in P3HT, as a result of short exciton lifetime and/or small diffusion constant.[29] The steric hindrance exerted by the alkyl chains at 9-position of the fluorene, which occupies orthogonal to the polymer π-plane is not advantageous for intermolecular exciton migration as well as charge transport. This is also evident from the amorphous nature observed in AFM measurement and moderate field-effect transistor (FET) hole mobility (5.3×10^{-3} $cm^2\ V^{-1}\ s^{-1}$) (see section 2-4.). In addition, these results implies the

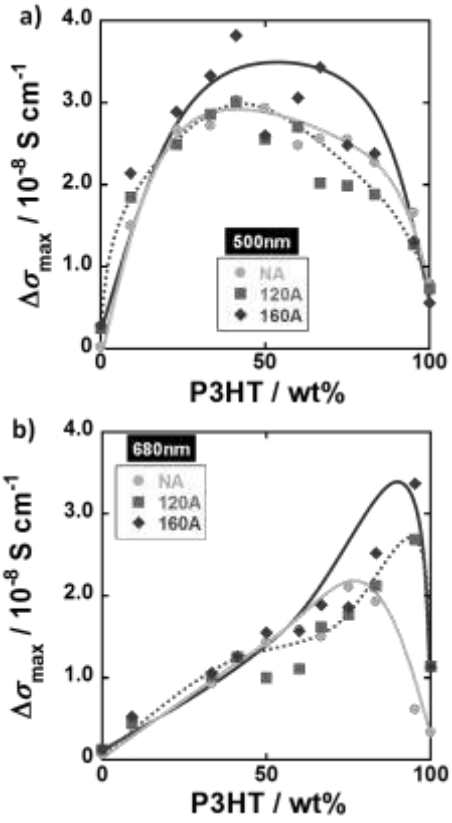

Figure 21. Laser-TRMC measurement results of P3HT:**P3** blend films prepared by drop-casting chloroform:chlorobenzene = 1:1.5 w/w solutions upon exposure to (a) 500 and (b) 680 nm. The NA (green circles), 120A (blue squares), and 160A (red diamonds) represent the non-thermal treatment, annealing at 120 °C for 10 min, and 160 °C for 10 min, respectively. Copyright 2013 The Society of Photopolymer Science and Technology. (ref 24)

overall TRMC signals are originated from the hole mobility of P3HT rather than electron mobility in **P3**. The impact of thermal annealing was similar to the 500 nm excitation, reinforcing our presumption on the primary annealing effect on the long-lived charge carriers.[30]

2-5-4. OPV performance of P3HT:P3 as all polymer solar cell

According to the Xe-flash TRMC results, we prepared P3HT:**P3** = 1:1 (w/w) devices from a chloroform solution, and examined the effects of thermal annealing. The best PCE was 0.06 % (short circuit current density, J_{sc} = 0.23 mA cm^{-2}, V_{oc} = 0.92 V, fill factor, FF = 0.31) obtained by 120 ºC annealing. The 160 ºC annealing resulted in the same performance of 0.06% (J_{sc} = 0.23 mA cm^{-2}, V_{oc} = 0.88 V, FF = 0.32). On the other hand, the device without thermal treatment did not exhibit diode characteristics at all. Surprisingly, these device characterizations are in perfect accordance with the screening results of Xe-flash TRMC (Figure 20), where both 120 and 160 ºC annealing improved $\Delta\sigma_{max}$ and the annealing temperature did not show clear difference.

The AFM topography and phase images of a blend film of P3HT and **P3** employed as an active layer in the optimized OPV device structures are shown in Figure 22. P3HT and **P3** are most likely mixed homogenously without forming large respective domains. Despite an appropriate BHJ formation, the obtained PCE of the OPV device (0.06%) is considerably lower than the highest value of polymer:polymer solar cells (~ 8.3%).[23] TRMC experiments highlight much larger $\Delta\sigma_{max}$ at the best p/n blend ratio than those of pristine P3HT or **P3**. Therefore, exciton formed in P3HT domain efficiently migrated to the p/n interface, giving rise to the total number of charge separated species. Therefore, the low electron mobility in **P3** domains might be responsible for the low PCE. The LUMO of **P3** is localized relatively on the TIDG unit. (See section 2-3-4.) This situation hampers the effective intermolecular overlap of LUMO as well as the intramolecular hopping between TIDG units. Further elongation of TIDG blocks in the backbone may provide the boosting of electron mobility, leading to the higher PCE in the present system. TIDG-based copolymers have just made its debut on the research field of organic

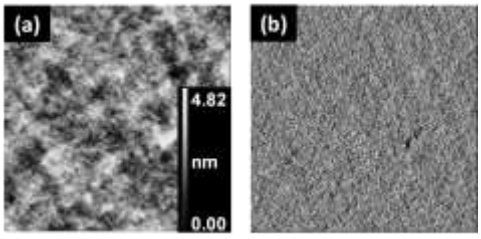

Figure 22. AFM (a) height and (b) phase images of P3HT:**P3** = 1:1 (w/w) films. The size is 2 × 2 μm^2. Copyright 2013 The Society of Photopolymer Science and Technology. (ref 24)

electronics, and thus we still have other molecular designing towards the improvement of PCE of all-polymer solar cells based on the electron-accepting TIDG unit.

2-6. Conclusion

TIDG-based new low-band gap polymers were designed and synthesized in combination with various donor units such as BDT, CPDT, FLO, and DTT. The TIDG unit acts as a strong electron acceptor and forms charge transfer complexes with BDT and CPDT. This leads to the enhancement of absorption intensity as well as extension of the absorption spectra towards NIR and IR regions (600–1400 nm), along with lowering HOMO, LUMO, and optical band gap. From the DFT calculation, the TIDG unit and its copolymers have better planarity than that of the IDG unit and its corresponding polymers. The preliminary FET experiments exhibited a moderate hole mobility of 5.3 $\times$ 10^{-3} cm^2 V^{-1} s^{-1} for **P2**, promising the application of these copolymers in organic electronic devices.

The author also investigated all-polymer solar cells using P3HT as p-type and **P3** as n-type polymers. Xe-flash TRMC revealed the best p/n blend ratio lies at around 1:1 and thermal annealing enhances the optoelectronic properties, arisen from the improvements in p/n phase separation and intermolecular π-stacking. In combination with the results of laser-flash TRMC excited at 500 and 680 nm, the thermal annealing was suggested to extend the charge carrier lifetime. The OPV device showed PCE of 0.06% with a high V_{oc} of 0.92 V in contrast to the low J_{sc} and FF. The device results are in good agreement with the Xe-flash TRMC evaluations. The low performance is probably due to the low electron mobility in **P3** phases, rationalized by its amorphous nature and localized LUMO on TIDG unit.

2-7. Experimental

Materials: All chemicals were purchased from Aldrich, Kanto Chemicals, TCI, or WAKO Chemical Co., and were used as received. The hydrazine reagent, 1,2-Bis(tert-butyldimethylsilyl)hydrazine (BTBSH), for this Wolff-Kisher-type reduction was synthesized by the literature method. [31] 2,6-bis(trimethyltin)-4,8-di(*n*-octyloxy) benzo[1,2-b:4,5b']dithiophene and 2,6-bis(trimethyltin)-4,8-di(2-ethylhexyloxy)benzo [1,2-b:4,5b']dithiophene were synthesized by adapting methods reported in the literature.[15,32] Column chromatography was carried out on Silica Gel 60N (spherical, neutral) from Kanto Chemicals, or NH silica gel from Fuji Silysia Chemical Ltd. Air- and water-sensitive synthetic steps were performed in a dried nitrogen or argon atmosphere using standard Schlenk techniques. All monomers were carefully purified prior to use in the polymerization.

Characterization: Proton nuclear magnetic resonance (^{1}HNMR) spectra and carbon nuclear magnetic resonance (^{13}CNMR) spectra were recorded on a JEOL 400SS (400 MHz) or EX-270 (270 MHz) spectrometers operating at 100 MHz for ^{13}C and 270 or 400 MHz for ^{1}H, respectively. The measurements were done at 25 °C in deuterated chloroform with tetramethylsilane or residual chloroform peaks as the internal reference standard for ^{1}H and ^{13}C chemical shifts respectively. Data were represented, as follows: chemical shift in ppm (δ = 0 ppm), multiplicity (s = singlet, d = doublet, dd = double-doublet, t = triplet, m = multiplet, br = broad), coupling constant (*J*) in Hertz (Hz), integration. Mass spectra were obtained on a FAB+ MS, JEOL the MS station JMS-700 with *m*-nitrobenzyl alcohol as the standard matrix. Elementary analysis was performed with a Yanagimoto Mfg. Co., Ltd. YANACO CHN CORDER (MT-5) for C, H, N elements, a Yanagimoto Mfg. Co., Ltd. trace element analysis instrument for S element, and a DIONEX DX-500 for Br, S elements. Molecular weights of polymers were determined using the gel permeation chromatography (GPC) method with polystyrene standards. GPC analysis was performed with polymer/tetrahydrofuran (THF) (HPLC grade) solution at a flow rate of 1 mL min^{-1} at 40 ˚C, on a HITACHI L-2130, L-2455, L-2530 chromatography instrument with Shodex KF-804L/KF-805L (Shodex Co., Japan) connected to a refractive index detector. The purification of Tin compounds was performed using the recycling preparative HPLC system on a Japan Analytical Industry Co., Ltd. LC-9210NEXT with JaiGel-1H/-2H (eluent $CHCl_3$). Differential scanning calorimetry (DSC) measurement was performed on a SEIKO Instrument Inc., EXSTAR6000 (DSC6200). Electronic absorption spectra were recorded using a JASCO V-570 UV/VIS/NIR spectrophotometer with 1 cm path length quartz cells for solution and drop-casted or spin-coated films on quartz plates for solid state

measurements.

Synthetic procedure of monomers:

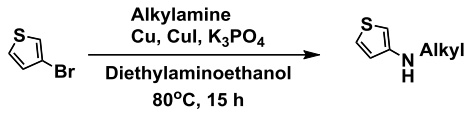

Synthesis of *N*-octylthiophen-3-amine (1): 3-bromothiophene (4.0 g, 2.45 × 10^{-2} mol), Cu (0.171 g, 2.45 × 10^{-3} mol), CuI (0.467 g, 2.45 × 10^{-3} mol), $K_3PO_4 \cdot H_2O$ (12.2 g, 4.91 × 10^{-2} mol), *n*-octylamine (6.0 mL, 3.68 × 10^{-2} mol), and deanol (24.5 mL) were added to a 100 mL dried flask at room temperature in an atmosphere of nitrogen. The reaction mixture was stirred at 80 ˚C for 48.5 h under nitrogen. After the reaction, the reaction mixture was cooled to room temperature. 20 mL of water was added and the mixture was extracted with diethylether (3 × 50 mL). The organic layer was washed with brine three times and dried over anhydrous $MgSO_4$. Solvent was removed under vacuum, and the residue was purified by column chromatography on NH silica gel, eluted with *n*-hexane. The product was obtained as a yellow liquid (3.1 g, 61 % yield) that turns red quickly on exposure to air and light.

^{1}HNMR (270 MHz, $CDCl_3$): δ 0.86-0.90 (m, 3H), 1.28-1.43 (m, 10H), 1.56-1.64 (m, 2H), 3.06 (t, J = 6.9 Hz, 2H), 3.53 (brs, 1H), 5.94 (dd, J_1= 3.0 Hz, J_2= 1.1 Hz, 1H), 6.61 (dd, J_1= 5.3 Hz, J_2= 1.4 Hz, 1H), 7.14 (dd, J_1= 5.3 Hz, J_2= 3.0 Hz, 1H)

Synthesis of *N*-(2-ethylhexyl)thiophen-3-amine (2): The synthesis of *N*-(2-ethyl hexyl)thiophen-3-amine was followed by the similar procedure as described for *N*-octylthiophen-3-amine. 3-Bromothiophene (5.0g, 3.07 × 10^{-2}mol) and 2-ethylhexyl amine (7.5 mL, 4.60 × 10^{-2}mol) was used in this procedure as amine reagent. The product was obtained as a yellow brown liquid (3.44 g, 53 % yield) that turns red quickly on exposure to air and light.

^{1}HNMR (270 MHz, $CDCl_3$): δ 0.86 -0.94 (m, 6H), 1.27-1.44 (m, 8H), 1.55 (brs, 1H), 2.98 (d, J = 5.9 Hz, 2H), 3.57 (brs, 1H), 5.92 (dd, J_1= 3.0 Hz, J_2= 1.6 Hz, 1H), 6.62 (dd, J_1= 5.3 Hz, J_2= 1.6 Hz, 1H), 7.14 (dd, J_1= 5.3 Hz, J_2= 3.2 Hz, 1H). ^{13}CNMR (100 MHz, ppm, $CDCl_3$): δ 10.97, 14.09, 23.10, 24.58, 29.05, 31.42, 39.24 49.47, 53.41, 94.79, 119.93, 124.98, 149.14.

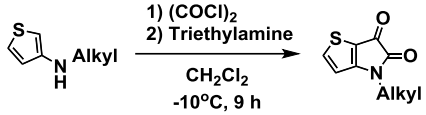

Synthesis of 4-(1-octyl)-4*H*-thieno[3,2-*b*]pyrrole-5,6-dione (3): Dichloromethane (CH_2Cl_2) (14.8 mL) and oxalyl chloride (2.0 mL, 2.37×10^{-2}mol) were added to a dried 100 mL flask under nitrogen atmosphere. The reaction solution was cooled to -15 ˚C in the salt ice bath. The dichloromethane (CH_2Cl_2) (25.3 mL) solution of *N*-octylthiophen-3-amine (3.1 g, 1.48×10^{-2} mol) was slowly added in 20 minutes. After added triethylamine (6.2 mL, 4.45×10^{-2} mol), the reaction mixture was stirred at 0 ˚C for 1 h. And then the ice bath was removed and the reaction mixture was allowed to warm to room temperature. After stirring at room temperature for 12 h, 30 mL of water was added and the mixture was extracted with CH_2Cl_2 (3 × 50 mL). The organic layer was washed with brine three times and dried over anhydrous $MgSO_4$. Solvent was removed under vacuum, and the residue was purified by flash chromatography on neutral silica gel, eluted with CH_2Cl_2/ *n*-hexane (from 1/ 1 to 5/ 1). The product was obtained as a red viscous liquid (2.2 g, 56 % yield)

^{1}HNMR (270 MHz, $CDCl_3$): δ 0.85-0.90 (m, 3H), 1.26-1.32 (m, 10H), 1.65-1.70 (m, 2H), 3.66 (t, *J* = 7.3 Hz, 2H), 6.78 (d, *J* = 4.9 Hz, 2H), 7.99 (d, *J* = 4.9 Hz, 2H). ^{13}CNMR (100 MHz, ppm, $CDCl_3$): δ 14.05, 22.61, 26.78, 28.20, 29.11, 29.13, 31.74, 42.18, 111.13, 112.93, 143.78, 161.48, 165.16, 173.06. Anal. Calcd for $C_{14}H_{19}NO_2S$: C, 63.36; H, 7.22; N, 5.28; O, 12.06; S, 12.08. Found: C, 63.56; H, 7.12; N, 5.21; S, 12.02.

Synthesis of 4-(2-ethylhexyl)-4*H*-thieno[3,2-*b*]pyrrole-5,6-dione (4): The synthesis of 4-(2-ethylhexyl)-4*H*-thieno[3,2-*b*]pyrrole-5,6-dione was followed by the similar procedure as described for 4-(1-octyl)-4*H*-thieno[3,2-*b*]pyrrole-5,6-dione. *N*-(2-ethylhexyl)thiophen-3-amine (4.18g, 1.98×10^{-2}mol) was used in this procedure. The product was obtained as a red solid (2.70 g, 51 % yield).

^{1}HNMR (270 MHz, $CDCl_3$): δ 0.88-0.95 (m, 6H), 1.27-1.43 (m, 8H), 1.69-1.78 (m, 1H), 3.54 (d, *J* = 7.0 Hz, 2H), 6.76 (d, *J* = 4.9 Hz, 2H), 7.99 (d, *J* = 4.9 Hz, 1H). ^{13}CNMR (100 MHz, ppm, $CDCl_3$): δ 10.55, 14.00, 22.98, 23.88, 28.60, 30.52, 38.33, 46.11, 111.11, 113.12, 143.65, 143.74, 161.76, 165.50, 172.99. Anal.Calcd for $C_{14}H_{19}NO_2S$: C, 63.36; H, 7.22; N, 5.28; O, 12.06; S, 12.08. Found: C, 63.46; H, 7.16; N, 5.28; S, 12.08.

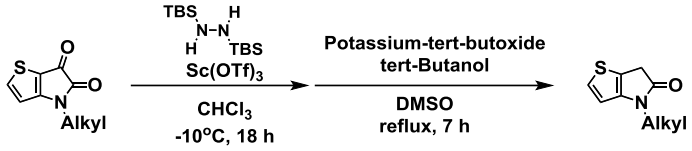

Synthesis of 4-(1-octyl)-4*H*,6*H*-thieno[3,2-*b*]pyrrole-5-one (5): Scandium Trifluoromethanesulfonate (3.7×10^{-3} g, 7.55×10^{-6}mol) and 4-(1-octyl)-4*H*-thieno[3,2-*b*]pyrrole-5,6-dione (0.1 g, 3.77×10^{-3}mol) was added to a dried 20 mL flask under nitrogen atmosphere. The flask was cooled in an ice bath. 1,2-bis(tert-butyldimethylsilyl) hydrazine (1.08 g, 4.15×10^{-3}mol) and anhydrous $CHCl_3$ (6.2 mL) were added sequentially via syringe in 15 minutes. The orange reaction mixture was stirred for 30 minutes at 0 ˚C, then the ice bath was removed and the reaction mixture was allowed to warm to room temperature. After stirring for 13 h, the chloroform was removed under vacuum using a rotary evaporator. The flask was flushed with dry nitrogen and stirred under vacuum at room temperature. After stirring for 30 minutes, the flask was flushed with nitrogen and dry *n*-hexane (10 mL) was added. The resulting red suspension was filtered through the celite to a 100 mL flask, and washed with *n*-hexane (3 × 10 mL). Solvent was removed under vacuum, and orange residue was dried under vacuum for 30 minutes. In a separate 100 mL flask, potassium *tert*-butoxide (5.07 g, 4.52×10^{-2} mol) and anhydrous dimethyl sulfoxide (37.4 mL) were charged under nitrogen atmosphere, and mixture was stirred at room temperature until all particulates had dissolved (~ 15 minutes). *tert*-Butanol (4.3 mL, 4.52×10^{-2} mol) was introduced and the resulting solution was transferred by syringe to the original flask containing the orange solid *N*-*tert*-butyldimethyl- silylhydrazone derivative under nitrogen atmosphere. The reaction flask was stirred at 100 ˚C for 7.5 h. After the reaction, the reaction mixture was extracted with ethyl acetate (twice). The organic extracts were washed with brine three times and dried over anhydrous $MgSO_4$. Solvent was removed under vacuum, and the red residue was purified by flash chromatography on neutral silica gel, eluted with CH_2Cl_2/ *n*-hexane (from 1/4 to 1/1 containing 5% triethylamine). The product was obtained as a pale-yellow viscous liquid (0.74 g, 78% yield)

^{1}HNMR (270 MHz, $CDCl_3$): δ 0.85-0.90 (m, 3H), 1.26-1.31 (m, 10H), 1.64-1.69 (m, 2H), 3.58 (s, 2H), 3.66 (t, J = 7.3 Hz, 2H), 6.76 (d, J = 5.1 Hz, 1H), 7.26 (d, J = 5.1 Hz, 1H). MS (FAB): *m*/*z* calcd for $C_{14}H_{21}NOS$: 251.13 [M^+]; found: 252.00 [M^+].

Synthesis of 4-(2-ethylhexyl)-4*H*,6*H*-thieno[3,2-*b*]pyrrole-5-one (6): 4-(2-ethylhexyl)-4*H*,6*H*-thieno[3,2-*b*]pyrrole-5-one was synthesized by following the

similar procedure as described for 4-(1-octyl)-4*H*,6*H*-thieno[3,2-*b*]pyrrole-5-one. 4-(1-ethylhexyl)-4*H*- thieno[3,2-*b*]pyrrole-5,6-dione (1.35g, 5.09 × 10^{-3}mol) was used in this procedure. The product was obtained as a dark violet liquid (0.86 g, 67 % yield). ^{1}HNMR (270 MHz, $CDCl_3$): δ 0.86-0.94 (m, 6H), 1.26-1.38 (m, 8H), 1.72-1.81 (m, 1H), 3.55 (dd, J_1= 7.4 Hz, J_2 = 2.2 Hz, 2H), 3.58 (s, 2H), 6.74 (d, *J* = 5.1 Hz, 1H), 7.24 (d, *J* = 5.1 Hz, 1H). ^{13}CNMR (100 MHz, ppm, $CDCl_3$): δ 10.61, 14.07, 23.02, 23.89, 28.67, 30.54, 36.24, 38.27, 45.73, 111.78, 111.90, 114.03, 126.29, 147.25, 177.65. MS (FAB): *m*/*z* calcd for $C_{14}H_{21}NOS$: 251.13 [M^+]; found: 252.00 [M^+].

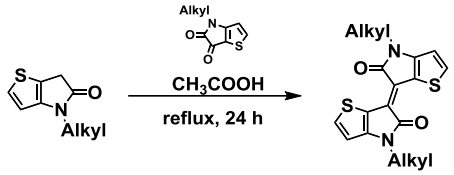

Synthesis of (*E*)-4,4'-bis(1-octyl)-[6,6'-bithieno[3,2-b]pyrrolylidene]-5,5'(4*H*,4'*H*)-dione (7): 4-(1-octyl)-4*H*-thieno[3,2-*b*]pyrrole-5,6-dione (2.89 × 10^{-2} g, 1.09 × 10^{-4}mol) and 4-(1-octyl)-4*H*,6*H*-thieno[3,2-*b*]pyrrole-5-one (2.74 × 10^{-2} g, 1.09 × 10^{-4}mol) and glacial acetic acid (1 mL) were added to a dried 20 mL Schlenk flask under nitrogen atmosphere. The reaction solution was stirred at 100 ˚C for 14 h. After the reaction, the reaction mixture was cooled to room temperature, and 10 mL of water was added. The resulting suspension was filtered. The residue was dissolved in CH_2Cl_2, and solvent was removed under vacuum. The residue was purified by column chromatography on neutral silica gel, eluted with *n*-hexane/ ethyl acetate (5/ 1). The product was obtained as a claret red solid (3.9 × 10^{-2} g, 72 % yield)
^{1}HNMR (270 MHz, $CDCl_3$): δ 0.84-0.88 (m, 6H), 1.26-1.33 (m, 20H), 1.65-1.79 (m, 4H), 3.81 (t, *J* = 7.6 Hz, 4H), 6.82 (d, *J* = 5.4 Hz, 2H), 7.54 (d, *J* = 5.1 Hz, 2H). MS (FAB): *m*/*z* calcd for $C_{28}H_{38}N_2O_2S_2$: 498.24 [M^+]; found: 498.00 [M^+].

Synthesis of (*E*)-4,4'-bis(2-ethylhexyl)-[6,6'-bithieno[3,2-b]pyrrolylidene]-5,5'(4*H*,4'*H*)-dione (8): (*E*)-4,4'-bis(2-ethylhexyl)-[6,6'-bithieno[3,2-b]pyrrolylidene]-5,5'(4*H*,4'*H*)-dione was synthesized by following the similar procedure as described for (*E*)-4,4'-bis(1-octyl)-[6,6'-bithieno[3,2-b]pyrrolylidene]-5,5'(4*H*,4'*H*)-dione.
4-(2-ethylhexyl)-4*H*-thieno[3,2-*b*]pyrrole-5,6-dione (0.90g, 3.40 × 10^{-3} mol) and 4-(2-ethylhexyl)-4*H*,6*H*-thieno[3,2-*b*]pyrrole-5-one (0.86g, 3.40 × 10^{-3} mol) were used in this procedure. The product was obtained as a dark violet liquid (0.99 g, 58% yield).

^{1}HNMR (270 MHz, $CDCl_3$): δ 0.88-0.95 (m, 12H), 1.26-1.38 (m, 16H), 1.80-1.90 (m, 2H), 3.70 (d, *J* = 6.5 Hz, 4H), 6.80 (d, *J* = 4.9 Hz, 2H), 7.53 (d, *J* = 5.1 Hz, 2H).^{13}CNMR (100 MHz, ppm, $CDCl_3$): δ 10.66, 14.07, 23.04, 23.92, 28.65, 30.48, 45.79, 111.33, 114.19, 121.07, 134.21, 151.54, 171.31. MS (FAB): *m*/*z* calcd for $C_{28}H_{38}N_2O_2S_2$: 498.24 [M^+]; found: 498.00 [M^+].

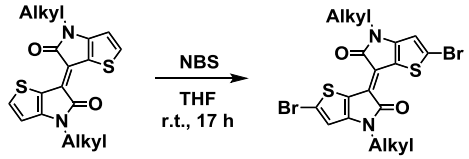

Synthesis of (*E*)-2,2'-dibromo-4,4'-bis(1-octyl)-[6,6'-bithieno[3,2-b]pyrrolylidene] -5,5'(4*H*,4′*H*)-dione (9): *N*-Bromosuccinimide (0.532 g, 2.99 × 10^{-3}mol) was added to the tetrahydrofuran (24 mL) solution of (*E*)-4,4'-bis(1-octyl)-[6,6'-bithieno[3,2-b] pyrrolylidene]-5,5'(4*H*,4'*H*)-dione (0.727 g, 1.46 × 10^{-3}mol) at room temperature in an atmosphere of nitrogen using a 50 mL flask. The reaction mixture was stirred at room temperature for 2.5 h. After the reaction, 50 mL of water was added and the mixture was extracted with CH_2Cl_2 (3 × 50 mL). The organic layer was washed with brine three times and dried over anhydrous $MgSO_4$. Solvent was removed under vacuum, and the residue was purified by flash chromatography on neutral silica gel, eluted with CH_2Cl_2/ *n*-hexane (1/ 1). The obtained violet solid was dissolved in $CHCl_3$ (15 mL) and reprecipitated from methanol (150 mL). The precipitate was filtrated using the membrane filter and dried under vacuum. The product was obtained as a wine-red solid (0.724 g, 76% yield)

^{1}HNMR (270 MHz, ppm, $CDCl_3$): δ 0.84-0.90 (m, 6H), 1.26-1.33 (m, 20H), 1.66-1.72 (m, 4H), 3.74 (t, *J* = 7.3 Hz, 4H), 6.85 (s, 2H). ^{13}CNMR (100 MHz, ppm, $CDCl_3$): δ 14.08, 22.62, 26.87, 28.58, 29.14, 29.15, 31.76, 41.90, 114.73, 114.86, 119.87, 123.29, 149.93, 170.19. MS (FAB): *m*/*z* calcd for $C_{28}H_{36}Br_2N_2O_2S_2$: 656.06 [$M^+$]; found: 656.00 [$M^+$]. Anal. Calcd for $C_{28}H_{36}Br_2N_2O_2S_2$: C, 51.22; H, 5.53; Br, 24.34; N, 4.27; O, 4.87; S, 9.77. Found: C, 51.21; H, 5.37; Br, 24.47; N, 4.28; S, 9.65.

Synthesis of (*E*)-2,2'-dibromo-4,4'-bis(2-ethylhexyl)-[6,6'-bithieno[3,2-b] pyrrolylidene]-5,5'(4*H*,4′*H*)-dione (10): (*E*)-2,2'-dibromo-4,4'-bis(2-ethylhexyl)-[6,6'-bithieno[3,2-b]pyrrolylidene]-5,5'(4*H*,4′*H*)-dione was synthesized by following the similar procedure as described for (*E*)-2,2'-dibromo-4,4'-bis(1-octyl)-[6,6'-bithieno [3,2-b]pyrrolylidene]-5,5'(4*H*,4′*H*)-dione.

(*E*)-4,4'-bis(2-ethylhexyl)-[6,6'-bithieno[3,2-b] pyrrolylidene]-5,5'(4*H*,4'*H*)-dione (0.99g, 1.98 × 10^{-3} mol) was used in this procedure. The product was obtained as a wisteria solid (0.69 g, 53% yield).
^{1}HNMR (270 MHz, $CDCl_3$): δ 0.89-0.95 (m, 12H), 1.26-1.31 (m, 16H), 1.73-1.83 (m, 2H), 3.64 (d, *J* = 7.3 Hz, 4H), 6.83 (s, 2H). ^{13}CNMR (100 MHz, ppm, $CDCl_3$): δ 10.60, 14.02, 23.04, 23.92, 28.63, 30.54, 38.56, 45.91, 114.75, 115.01, 119.80, 123.21, 150.25, 170.48. MS (FAB): *m*/*z* calcd for $C_{28}H_{36}Br_2N_2O_2S_2$: 656.06 [$M^+$]; found: 656.00 [$M^+$]. Anal. Calcd for $C_{28}H_{36}Br_2N_2O_2S_2$: C, 51.22; H, 5.53; Br, 24.34; N, 4.27; O, 4.87; S, 9.77. Found: C, 51.09; H, 5.25; Br, 24.17; N, 4.44; S, 9.50.

The synthesis of 2,6-bis(trimethyltin)-4,8-di(*n*-octyloxy)benzo[1,2-b:4,5b']dithiophene (**13**) and 2,6-bis(trimethyltin)-4,8-di(2-ethylhexyloxy)benzo[1,2-b:4,5b']dithiophene (**14**) were carried out following the literature.[15,32] The products were purified using the recycling preparative HPLC system and recrystallization with isopropanol to obtain the white solid.

2,6-Bis(trimethyltin)-4,8-di(*n*-octyloxy)benzo[1,2-b:4,5b']dithiophene (13): ^{1}HNMR (270 MHz, $CDCl_3$): δ 0.45 (s, 18H), 0.90 (t, *J* = 6.5 Hz, 6H), 1.32-1.40 (m, 20H), 1.89 (quin, *J* = 6.9 Hz, 4H), 4.30 (t, *J* = 6.5 Hz, 4H), 7.52 (s, 2H)
2,6-Bis(trimethyltin)-4,8-di(2-ethylhexyloxy)benzo[1,2-b:4,5b']dithiophene (14): ^{1}HNMR (270 MHz, $CDCl_3$): δ 0.44 (s, 18H), 0.92-0.96 (m, 6H), 1.03 (t, *J* = 7.3 Hz, 6H), 1.41-1.43 (m, 10H), 1.55-1.82 (m, 8 H), 4.19 (d, *J* = 5.4 Hz, 4H), 7.51 (s, 2H)

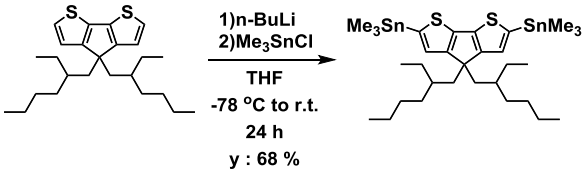

The synthesis of 4-bis(2-ethylhexyl)-2,6-bis(trimethylstannanyl)-4*H*-cyclopenta [2,1-b:3,4-b']dithiophene (15): 4-bis(2-ethylhexyl)-4*H*-cyclopenta[2,1-b:3,4-b'] dithiophene (1.01 g, 2.48 × 10^{-3}mol) and THF (24.8 mL) were added to a 100 mL flask. The reaction mixture was cooled to -78 ˚C in acetone dry ice bath, and *n*-butyllithium (2.3 mL, 2.69 M *n*-hexane solution) was added slowly via syringe in 10 minutes. After stirring at room temperature for 1 h, the reaction mixture was cooled to -78 ˚C in acetone dry ice bath again and the THF (7.4 mL) solution of trimethyltin chloride (1.48 g, 7.45 × 10^{-3}mol) was added slowly via syringe in 20 minutes. Then the dry ice bath

was removed and the reaction mixture was allowed to warm to room temperature. After stirring for 24 h, 50 mL of water was added and the mixture was extracted with *n*-hexane (3 × 50 mL). The organic layer was washed with brine three times and dried over anhydrous $MgSO_4$. Solvent was removed under vacuum, and purified using the recycling preparative HPLC system. The product was obtained as a yellow viscous liquid (1.24 g, 68 % yield)

^{1}HNMR (270 MHz, $CDCl_3$) δ 0.35 (s, 18H), 0.58 (t, *J* = 7.3 Hz, 6H), 0.74 (t, *J* = 6.8 Hz, 6H), 0.87-0.96 (m, 18H), 1.84 (t, *J* = 5.4 Hz, 4H), 6.94 (t, *J* = 2.7 Hz, 2H)

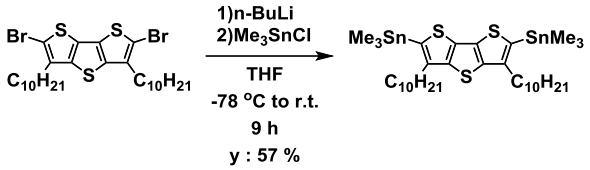

The synthesis of 2,6-bis(trimethylstannyl)-3,5-didecanyldithieno[3,2-b:2',3'-d] thiophene (16): 2,6-dibromo-3,5-didecanyldithieno[3,2-b:2',3'-d]thiophene (0.05 g, 7.88×10^{-5}mol) and THF (2.3 mL) were added to a 100 mL flask. The reaction mixture was cooled to -78 ˚C in acetone dry ice bath, and *n*-butyllithium (0.1 mL, 2.69 M n-hexane solution) was added slowly via syringe in 10 minutes. After stirring at room temperature for 2 h, the reaction mixture was cooled to -78 ˚C in acetone dry ice bath again and the trimethyltin chloride (0.047 g, 2.36×10^{-4}mol) was added slowly and stirred for 4 h. Then the dry ice bath was removed and the reaction mixture was allowed to warm to room temperature. After stirring for 3 h, 10 mL of water was added and the mixture was extracted with *n*-hexane (3 × 50 mL). The organic layer was washed with brine three times and dried over anhydrous $MgSO_4$. Solvent was removed under vacuum, and purified using the recycling preparative HPLC system. The product was obtained as a white solid (0.036 g, 57% yield)

^{1}HNMR (270 MHz, $CDCl_3$): δ 0.42 (s, 18H), 0.88 (t, 6H), 1.26-1.43(m, 28H), 1.65-1.75 (m, 4H), 2.71 (t, *J* = 8.1 Hz, 4H).

General Procedure for the Synthesis of Copolymers

The synthetic route for copolymers is shown in Scheme 4. Polymerization steps for **P1**, **P2**, **P4**, **P5**, **P6**, and **P7** were carried out through the palladium (0)-catalyzed Stille cross coupling reactions. Polymerization steps for **P3** was performed through the palladium (0)-catalyzed Suzuki-Miyaura cross coupling reaction. For Stille cross

coupling reaction, 1 equiv. of dibromo monomers and 1 equiv. of bistrimethylstannanyl monomers were added in anhydrous xylene and anhydrous *N*,*N*-dimethylformamide (9/1, 0.05 mol/dm^{-3}) into 20 mL Schlenk flask. The tetrakis (triphenylphosphine) palladium (2.5 mol %) was transferred into the mixture in a nitrogen atmosphere. The reaction mixture was stirred at 130 ˚C for 4 - 6 h, and then an excess amount of bromobenzene and trimethyl(phenyl)tin were added to end-cap the trimethylstannyl and bromo groups for 1h, respectively. After adding four times larger amount of xylene than reaction solution, the reaction mixture was cooled to 40˚C and added slowly into a vigorously stirred ten times larger volume of methanol than diluted reaction mixture. The polymers were collected by filtration and dried in vacuum. The dried crude polymers were dissolved in $CHCl_3$ (around 200 mL) and further purified by the column chromatography on neutral silica gel and the six layered interleave NH silica with NH_2 silica gel layer for removing the metallic impurities. The obtained $CHCl_3$ solution was filtered through the celite and solvent was removed under vacuum. The remained solid was dissolved in minimum amount of $CHCl_3$ and reprecipitated by six times larger amount of acetone than dissolved solution to remove oligomers. The precipitate was filtrated using the membrane filter and dried under vacuum. For Suzuki-Miyauracross coupling reaction, 1 equiv. of dibromo monomers and 1 equiv. of diboronate ester monomers were added in anhydrous xylene (0.15 mol/ dm^{-3}) into 20 mL Schlenk flask. 3 equiv. of 2 M K_2CO_3 aq. and 0.2 equiv. of Aliquat 336 were added for base and phase-transfer catalyst, respectively. After mixed all reagents without catalyst, freeze-pump-thaw cycling was carried out three times. The tetrakis(triphenylphosphine) palladium (2.5 mol %) was transferred into the mixture in a nitrogen atmosphere. The reaction mixture was stirred at 100 ˚C for 3 h. The end-cap procedure, reaction processing, and purification were same as that of Stille cross coupling reaction.

The synthesis of copolymer P1: Following the general polymerization procedure, (*E*)-2,2'-dibromo-4,4'-bis(2-ethyl hexyl)-[6,6'-bithieno[3,2-b]pyrrolylidene]-5,5'(4*H*,4'*H*)-dione **10** (0.100 g, 1.52 × 10^{-4} mol), and 2,6-Bis(trimethyltin)-4,8-di(2-ethylhexyloxy)benzo[1,2-b:4,5b'] dithiophene **14** (0.118 g, 1.52 × 10^{-4}mol) were used in this polymerization, and the polymer was obtained as grass green film like solid. (0.070 g)

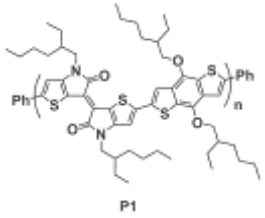

P1

^{1}HNMR (400MHz, $CDCl_3$): δ0.80-1.15 (m, 24 H), 1.06-1.49 (m, 26 H), 1.60-1.79 (m, 8 H), 1.80-1.96 (m, 4H). Number average molecular weight (M_n) = 39.9 × 10^{3}g mol^{-1}, Polydispersity index (PDI) = 2.2.

The synthesis of copolymer P2: Following the general polymerization procedure, (*E*)-2,2'-dibromo-4,4'-bis (2-ethylhexyl)-[6,6'-bithieno[3,2-b]pyrrolylidene]-5,5'(4*H*,4′*H*)-dione **10** (0.10 g, 1.52 × 10^{-4} mol), and 4-bis(2-ethylhexyl)-2,6-bis (trimethylstannanyl)-4*H*-cyclopenta[2,1-b:3,4-b']dithiophene **15** (0.111 g, 1.52 × 10^{-4} mol) were used in this polymerization, and the polymer was obtained as grass green film like solid (0.113 g).

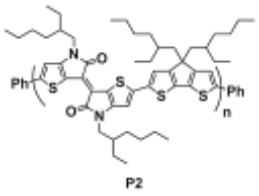

P2

^{1}HNMR (400 MHz, $CDCl_3$): δ 0.64-0.68 (m, 6H), 0.72-0.78 (m, 6H), 0.91-1.10 (m, 30H), 1.25-1.42 (m, 16H), 1.89-1.94 (m, 6H), 6.84 (brs, 2H), 7.32 (brs, 2H).M_n = 8.6 × 10^3g mol^{-1}, PDI = 1.7.

The synthesis of copolymer P3: Following the general polymerization procedure, (*E*)-2,2'-dibromo-4,4'-bis (2-ethylhexyl)-[6,6'-bithieno[3,2-b]pyrrolylidene]-5,5'(4*H*,4′*H*)-dione **10** (0.100 g, 1.52 × 10^{-4} mol) and 9,9-dioctylfluorene-2,7-diboronic acid bis(1,3-propanedid)ester (8.5 × 10^{-2} g, , 1.52 × 10^{-4} mol) were used in this polymerization, and polymer was obtained as malachite green solid. (0.117 g).

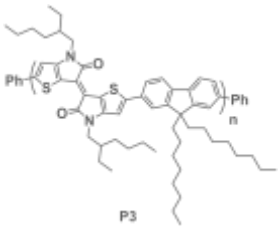

P3

^{1}HNMR (400 MHz, $CDCl_3$) δ 0.65 (brs, 4H), 0.79 (t, *J* = 7.2 Hz, 6H), 0.94 (t, *J* = 7.2 Hz, 6H), 1.00 (t, *J* = 7.2 Hz, 6H)1.10-1.19 (m, 20H), 1.38-1.43 (m, 16H), 1.99 (brs, 4H), 2.09 (brs, 2H), 3.81 (brs, 4H), 7.13 (brs, 2H), 7.73-7.77 (m, 6H). M_n = 10.0 × 10^3g mol^{-1}, PDI = 2.3.

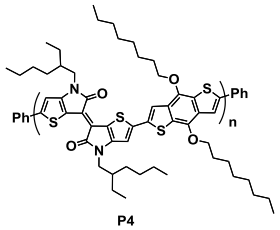

P4

The synthesis of copolymer P4: Following the general polymerization procedure, (*E*)-2,2'-dibromo-4,4'-bis(2-ethylhexyl)-[6,6'-bithieno[3,2-b]pyrrolylidene]-5,5'(4*H*,4′*H*)-dione **10** (0.100 g, 1.52 × 10^{-4}mol), and 2,6-Bis(trimethyltin)-4,8-di(2-octyloxy)benzo[1,2-b:4,5b']dithiophene **13** (0.118 g, 1.52 × 10^{-4} mol) were used in this polymerization, and the polymer was obtained as soluble green solid. M_n = 5.7 × 10^3 g mol^{-1}, PDI = 2.1.

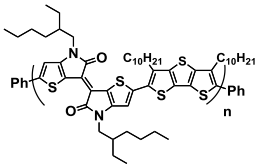

P5

The synthesis of copolymer P5: Following the general polymerization procedure, (*E*)-2,2'-dibromo-4,4'-bis(2-ethylhexyl)-[6,6'-bithieno[3,2-b]pyrrolylidene]-5,5'(4*H*,4′*H*) -dione **10** (0.029 g, 4.49 × 10^{-5} mol) and 2,6-Bis(trimethylstannyl)-3,5-didecanyl dithieno[3,2-b:2’,3’-d]thiophene **16** (0.036 g, 4.49 × 10^{-5} mol) were used in this polymerization, and the polymer was obtained as slightly soluble billiard green solid. M_n = 1.7× 10^3 g mol^{-1}, PDI = 1.8.

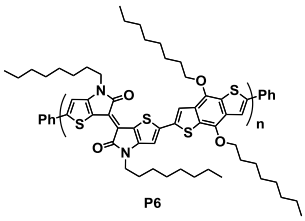

P6

The synthesis of copolymer P6: Following the general polymerization procedure, (*E*)-2,2'-dibromo-4,4'-bis(1-octyl)-[6,6'-bithieno[3,2-b]pyrrolylidene]-5,5'(4*H*,4′*H*)-dion e **9** (0.10 g, 1.52 × 10^{-4} mol) and 2,6-Bis(trimethyltin)-4,8-di(2-octyloxy) benzo[1,2-b:4,5b’]dithiophene **13** (0.117 g, 1.52 × 10^{-4} mol) were used in this polymerization, and the polymer was obtained as insoluble ivy green solid.

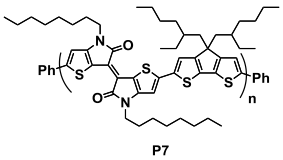

P7

The synthesis of copolymer P7: Following the general polymerization procedure, (*E*)-2,2'-dibromo-4,4'-bis(1-octyl)-[6,6'-bithieno[3,2-b]pyrrolylidene]-5,5'(4*H*,4′*H*)-dion e **9** (0.10 g, 1.52 × 10^{-4} mol) and 4-bis(2-ethylhexyl)-2,6-bis(trimethyl stannanyl)-4*H*-cyclopenta[2,1-b:3,4-b’]dithiophene **15** (0.111 g, 1.52 × 10^{-4} mol) were used in this polymerization, and the polymer was obtained as grass green solid. (0.131 g) M_n = 7.4× 10^3 g mol^{-1}, PDI = 1.8

UV photo electron spectroscopy measurement

The optical band gap was determined from the onset of the absorption band edge. The highest occupied molecular orbital (HOMO) were estimated by UV photoelectron spectroscopy (UPS) measurement. UPS was performed on an AC-2 of

RIKEN KEIKI Co., Ltd. For the UPS measurement, thin films of the polymers were drop-casted on an ITO-coated glass surface from chlorobenzene (CB) or $CHCl_3$ solution and it was completely dried before mounting on the spectrometer. Photoelectrons emitted from the film were detected after illuminating the film with UV radiation. With photon energy increased with an interval of 0.1 eV, the photoelectron counts were measured.

Fabrication and valuation of Organic Field-Effect Transistor (OFET) Devices

FETs were fabricated in a top-contact configuration on a heavily n-doped Si wafer with 200 nm thermally grown SiO_2 (the capacitance per unit area of the gate dielectric layer is C_i = 17.3 nF cm^{-2}). The substrate surface were treated with piranha solution for 10 min, subjected to cleaning using ultrasonication in deinonized water (twice), and *iso*-propanol. The cleaned substrates were dried then treated with plasma for 20 min. Thin films of the copolymer were deposited on the treated substrates by spin coating (1500 rpm) using a 0.5 wt % of **P1** and **P3** chloroform solution and 1.0 wt % of **P2** cholorobenzene solution. On top of the organic film, about 50nm thick gold was deposited as source and drain contacts through a shadow mask. The channel width (W) of drain and source is 3 mm. The drain-source channel length (L) was changed as 20, 50, 100, 200, 500μm and suitable one of them was chosen for estimating hole mobility. Characteristics of the FET devices were measured at room temperature under ambient conditions with a Keithley 4200-SCS semiconductor analyzer system. When measuring transfer curves, gate voltage (V_G) was scanned from -100 to 0 V. Field-effect hole mobility (μ_{hole}^{FET}) was estimated from the transfer curve in the saturation regime at V_D = - 100 V. A line drawn through the linear part of an $I_{DS}^{1/2}$ vs. V_G plot allowed extraction of threshold voltage (V_{th}) and field-effect mobilities using the square-low equation for the saturation regime. Current on/ off ratio (I_{on}/ I_{off}) was determined from the minimum I_{DS} (I_{off}) and the maximum I_{DS} at V_G = -100 V (I_{on}).

Fabrication of Organic photovoltaics (OPV).

OPV devices were fabricated according to the previous reports.[29)] The device configuration was ITO (120-160 nm)/PEDOT:PSS (45-60 nm)/active layer (ca. 100 nm)/Ca (10 nm)/Al (80 nm) with an active area of 7.1 mm^2. Current-voltage (J-V) curves were measured using a source-measure unit (ADCMT Corp., 6241A) under AM 1.5 G solar illumination at 100 mW cm^{-2} (1 sun) using a 300 W solar simulator (SAN-EI Corp., XES-301S).

References

[1] (a) Liang, Y.; Xu, Z.; Xia, J.; Tsai, S-T.; Wu, Y.; Li, G.; Ray, C.; Yu, L. Adv. Mater. 2010, 22, 1. (b) Najari, A.; Beaupré, S.; Berrouard, P.; Zou,Y.; Pouliot, J-R.; Pérusse,C. L.; Leclerc,M. *Adv. Funct. Mater*. **2011**, *21*, 718. (c) Liang, Y.; Feng, D.; Wu, Y.; Tsai, S-T.; Li, G.; Ray, C.; Yu, L. *J. Am. Chem. Soc*. **2009**, *131*, 7792. (d) Chu, T-Y.; Lu, J.; Beaupre, S. ; Zhang, Y.; Pouliot, J-R.; Wakim, S.; Zhou, J.; Leclerc, M.; Li, Z.; Ding, J.; Tao, Y. *J. Am. Chem. Soc*. **2011**, *133*, 4250. (e) He, F.; Wang, W.; Chen, W.; Xu, T.; Darling, S. B.; Strzalka, J.; Liu, Y.; Yu, L. *J. Am. Chem. Soc*. **2011**, *133*, 3284. (f) Ajayaghosh, A. *Chem. Soc. Rev.*, **2003**, *32*, 181. (g) Zhou, H.; Yang, L.; You, W. *Macromolecules* **2012**, *45*, 607.

[2] Deng, P.; Zhang, Q. *Polym. Chem*., **2014**, *5*, 3298–3305.

[3] Stalder, R.; Mei, J.; Graham, K. R.; Estrada, L. A.; Reynolds, J. R. *Chem. Mater*., **2014**, *26*, 664–678.

[4] Stalder, R.; Mei, J.; Reynolds, J. R. *Macromolecules*, **2010**, *43*, 8348–8352.

[5] Mei, J.; Graham, K. R.; Stalder, R.; Reynolds, J. R. *Org. Lett.* **2010**, *12*, 4, 660-663.

[6] Lei, T.; Cao, Y.; Fan, Y.; Liu, C.-J.; Yuan, S.-C. Pei, J. *J. Am. Chem. Soc*. **2011**, *133*, 6099–6101.

[7] Zhuang, W.; Bolognesi, M.; Seri, M.; Henriksson, P.; Gedefaw, D.; Kroon, R.; Jarvid, M.; Lundin, A.; Wang, E.; Muccini, M.; Andersson, M. R. *Macromolecules* **2013**, *46*, 8488−8499.

[8] Grand, C.; Baek, S.; Lai, T.-H.; Deb, N.; Zajaczkowski, W.; Stalder, R.; Müllen, K.; Pisula,W.; Bucknall, D. G. So, F.; Reynolds, J. R. *Macromolecules* **2016**, *49*, 4008−4022.

[9] Yang, Y.; Wu, R.; Wang, X.; Xu, X.; Li, Z.; Li, K.; Peng, Q. *Chem. Commun*. **2014**, *50*, 439-441.

[10] Ma, Z.; Wang, E.; Jarvid, M. E.; Henriksson, P.; Inganäs, O.; Zhang, F.; Andersson, M. R. *J. Mater. Chem*., **2012**, *22*, 2306–2314.

[11] Koizumi, Y.; Ide, M.; Saeki, A.; Vijayakumar, C.; Balan, B.; Kawamoto, M.; Seki, S. *Polym. Chem*. **2013**, *4*, 484–494.

[12] Mei, J.; Kim, D. H.; Ayzner, A. L.; Toney, M. F.; Bao, Z. *J. Am. Chem. Soc*. **2011**, *133*, 20130–20133.

[13] Ma, Z.; Wang, E.; Vandewal, K.; Andersson, M. R.; Zhang, F. *Appl. Phys. Lett*., **2011**, *99*, 143302, 1-3.

[14] Wang, E.; Ma, Z.; Zhang, Z.; Vandewal, K.; Henriksson, P.; Inganϵas, O.; Zhang, F.; Andersson, M. R. *J. Am. Chem. Soc*. **2011**, *133*, 14244–14247.

[15] Huo, L.; Hou, J. *Polym. Chem*. **2011**, *2*, 2453–2461.

[16] Lei, T.; Cao, Y.; Zhou, X.; Peng, Y.; Bian, J.; Pei, J. *Chem. Mater.* **2012**, *24*, 1762–1770.

[17] Ho, C. -C.; Chang, S. -Y.; Huang, T.-C.; Chen, C. -A.; Liao, H.-C.; Chen, Y. -F.; Su, W. -F. *Polym. Chem*. **2013**, *4*, 5351-5360.

[18] Yuan, M.-C.; Chiu, M.-Y.; Chiang, C.-M.; Wei, K.-H. *Macromolecules*, **2010**, *43*, 6270–6277.

[19] Yan, H.; Chen, Z.; Zheng, Y.; Newman, C.; Quinn, J. R.; Dötz, F.; Kastler, M.; Facchetti, A. *Nature* **2009**, *457*, 679–689.

[20] Jung, J. W.; Jo, J.; W.; Chueh, C. -C.; Liu, F.; Jo, W. H.; Russell, T. P.; Jen, A. K.-Y. *Adv. Mater.* **2015**, *27*, 3310–3317.

[21] Hwang, Y. -J.; Courtright, B. A. E.; Ferreira, A. S.; Tolbert, S. H.; Jenekhe, S. A. *Adv. Mater*. **2015**, *27*, 4578–4584.

[22] Benten, H.; Nishida, T.; Mori, D.; Xu, H.; Ohkita, H.; Ito, S. *Energy Environ. Sci*. **2016**, *9*, 135–140.

[23] Gao, L.; Zhang, Z. -G.; Xue, L.; Min, J.; Zhang, J.;Wei, Z.; Li, Y. *Adv. Mater*. **2016**, *28*, 1884–1890.

[24] Ide, M.; Koizumi, Y.; Saeki, A.; Seki, S. *J. Photopolym. Sci. Tech*. **2013**, *26*, 217–221.

[25] Hou, J.; Tan, Z.; Yan, Y.; He, Y.; Yang, C.; Li, Y. *J. Am. Chem. Soc*. **2006**, *128*, 4911–4916.

[26] Saeki, A.; Tsuji, M.; Seki, S. *Adv. Energy Mater*. **2011**, *1*, 661–669.

[27] Saeki, A.; Yoshikawa, S.; Tsuji, M.; Koizumi, Y.; Ide, M.; Vijayakumar, C.; Seki, S. *J. Am. Chem. Soc*. **2012**, *134*, 19035−19042.

[28] Jung, I. H.; Lo, W. -Y.; Jang, J.; Chen, W.; Zhao, D.; Landry, E. S.; Lu, L.; Talapin, D. V.; Yu, L. *Chem. Mater*. **2014**, *26*, 3450−3459.

[29] Shaw, P. E.; Ruseckas, A.; Samuel, I. D. W. *Adv. Mater.* **2008**, *20*, 3516–3520.

[30] Mikie, T.; Saeki, A.; Ikuma, N.; Kokubo, K.; Seki, S. *ACS Appl. Mater. Interfaces* **2015**, *7*, 12894−12902.

[31] Granström, M.; Petritsch, K.; Arias, A. C.; Lux, A.; Andersson, M. R.; Friend, R. H. *Nature* **1998**, *395*, 257-260.

[32] Balan, B.; Vijayakumar, C.; Saeki, A.; Koizumi, Y.; Seki, S. *Macromolecules* **2012**, *45*, 2709−2719.

Chapter 3: Evaluation of TIDG Copolymers through Analysis of Carrier Dynamics and Organic Photovoltaic Application

3-1. Introduction

Broadening of electronic absorption implemented by incorporating electron donor and acceptor units into the polymer backbone is a general strategy to improve the power conversion efficiency (PCE)[1], because the wider light absorption lead the enhancement of short-circuit current density (J_{sc}). However, raising its highest occupied molecular orbital (HOMO)s by narrowing bandgap of p-type polymer resulted in the decrease of open circuit voltage (V_{oc}). Besides, the energy offset of at least 0.3 eV between the lowest unoccupied molecular orbital (LUMO)s of p-type polymer and n-type fullerene derivative is empirically required as a sacrifice of efficient charge separation.[2] Therefore, the best bandgap energy of 1.37-1.45 eV for a single cell is inferred by considering overlap with the solar spectrum, the energy offset, and trade-off with V_{oc}.[3] In addition, near-infrared (NIR) absorbing polymer is a crucial prerequisite towards a high performance tandem cell[4] as a complemental photoactive layer of ultraviolet and visible light absorbing layer such as poly(3-hexylthiophene), P3HT.

In previous research, the author,[5] Ashraf *et al*.,[6] and Janssen *et al*.,[7] have reported NIR absorbing conjugated copolymers comprising of novel electron accepting unit: 4,4'-bis(alkyl)-[6,6'-bithieno[3,2-*b*]pyrrolylidene]-5,5'(4*H*,4'*H*)-dione, the so-called thienoisoindigo (TIDG). This is an analog of an isoindigo (IDG) unit,[8] where its arylenes are replaced by thiophene rings. Notably, this alternation brought about a stronger electron accepting nature along with the higher planarity than IDG, affording extensively narrow bandgap (1.0 – 1.6 eV) in conjugation with typical donor units. The hole mobility assessed by field-effect transistors (FETs) was on the order of 10^{-4} to 10^{-3} $cm^2 V^{-1} s^{-1}$,[5] reflecting the long range translational motion of holes in the thin interfacial layer parallel to the substrate. The geometry of the device in FET and OPV is nearly orthogonal with each other for the pathway of charge carriers in their active layers. The value of hole mobility derived from the face-on orientation of the materials suggests the lower limit of hole mobility in their bulk, demonstrating feasibility to use them in OPV.[9]

In this chapter, the author investigated OPV of donor-acceptor (push-pull) polymers of TIDG coupled in an alternating fashion with benzodithiophene (BDT), cyclopentadithiophene (CPDT), and fluorene (FLO) shown in Figure 23a. There is a delicate and complicated interplay of the p-type polymers and n-type fullerenes in terms of BHJ structure, mobility, and lifetime of charge carrier. To gain complementary information on the effects of thermal annealing and p/n blend ratio, the time-resolved

microwave conductivity (TRMC) measurements [10, 11] were performed using monochromic light pulse from a nanosecond laser[12] or white light pulse from a Xe flash-lamp[13] as photoexcitation sources. The present technique allows for a speedy and robust evaluation of active layer without undesired influences from electrode contact issues, impurities, and degradation of the materials themselves. Furthermore to shed light on the charge carrier generation mechanism, the author performed femtosecond transient absorption spectroscopy (TAS).[14] The present chapter focuses on the relationship among the device characterization, TRMC results, and TAS evaluation, in conjunction with active layer surface morphology and bulk structures.[15]

3-2. Optical and electrochemical properties.

The optical and electrochemical properties of TIDG-based copolymers, **P1** (BDT), **P2** (CPDT), and **P3** (FLO) were characterized by electronic absorption and photoelectron yield spectroscopies (PYS).[5] In spite of identical LUMO levels of these copolymers (-3.8 eV), their HOMOs measured by the onset of PYS were varied as, -4.9 eV for **P1**, -4.8 eV for **P2**, and -5.4 eV for **P3,** reflecting the electron-donating properties of their donor units. The bandgap energies estimated from the electronic absorption band edges in the film states were 1.1. 1.0, and 1.6 eV for **P1**, **P2**, and **P3**, respectively. The weight-averaged molecular weights of **P1**, **P2**, and **P3** are 87, 15, and 24 × 10^3 g mol^{-1} with the polydispersity indices of 5.8 (bimodal), 1.7, and 2.3, respectively.

Figure 23b shows the normalized electronic absorption spectra of the

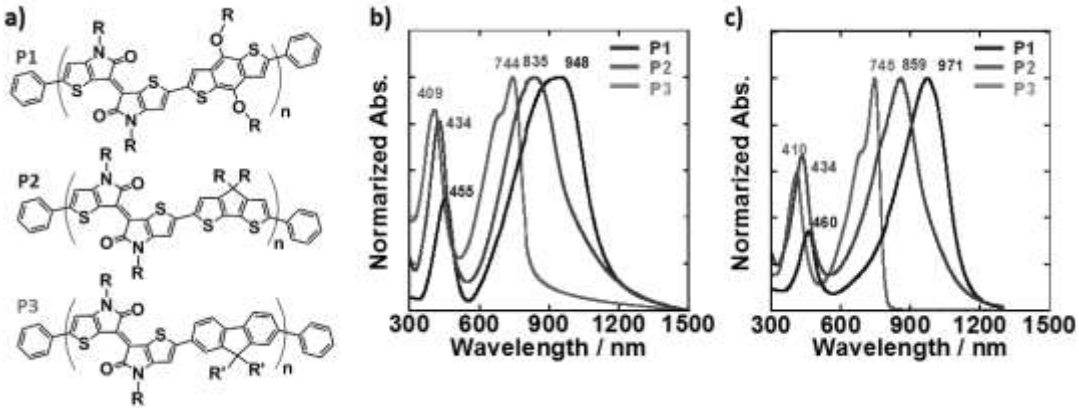

Figure 23. (a) Chemical structure of TIDG-based copolymers. R:ethylhexyl, R′ ; n-octyl. (b) Normalized electronic absorption spectra of **P1** (red), **P2** (blue), and **P3** (green) films. The values represent the peak wavelengths. (c) Electronic absorption spectra of **P1** (red), **P2** (blue), and **P3** (green) in chloroform. Reprinted with permission from ref 15. Copyright 2013 American Chemical Society.

copolymer films. Respective polymers have two absorption peaks in visible (400-460 nm) and in NIR (740-950 nm). These copolymers represent the "push-pull" effect between the donor and the acceptor (TIDG) units, which can be confirmed by their red-shifted electronic absorption compared to those in the homopolymers of the donor units with carbazole,[16] CPDT[17] and FLO,[18] respectively. The near-infrared absorptions of **P1** and **P2** in the film state were blue-shifted by about 20 nm in comparison with that in chloroform solution (Figure 23c) and the relative absorption intensity to visible region was reduced. In contrast, the electronic absorption spectrum in **P3** in the film state is almost identical in the solution. These observations indicate that **P1** and **P2** form a strong intramoleular charge transfer (ICT) state[19] between the donors and TIDG, while **P3** partially contains π-conjugation in addition to ICT character.[5] This is corroborated by the density functional theory calculations[5] and the presence of distinct vibronic feature in electronic absorption spectrum of **P3**, in contrast to its absence in **P1** and **P2**. The low-lying HOMO of FLO forms weak ICT with TIDG in comparison with the strong ICT for BDT and CPDT.

3-3. Characterization of BDT-TIDG polymer (P1).

Prior to OPV device fabrication, laser-flash and Xe-flash TRMC experiments were performed to examine the impacts of p/n blend ratio, choice of solvents, and thermal annealing. Figure 24a shows p/n blend ratio dependence of the product of photoconductivity maxima ($\Delta\sigma_{max}$) and half-lifetime ($\tau_{1/2}$) in the TRMC transients

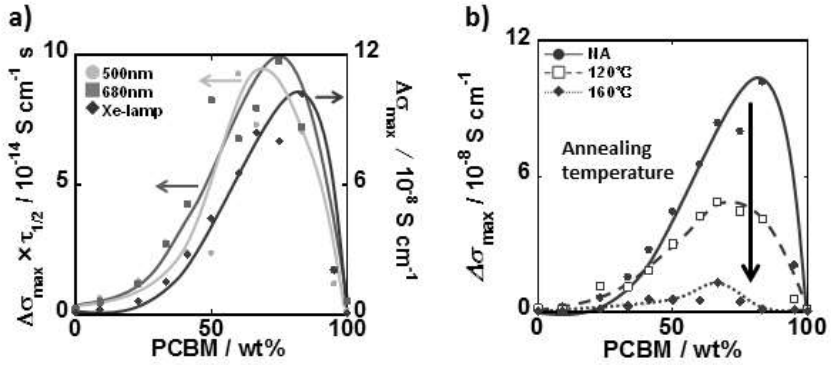

Figure 24. TRMC results of **P1**:$PC_{61}BM$ blend films prepared by dropcasting CF:CB = 3:1 w/w solutions. (a) $\Delta\sigma_{max} \times \tau_{1/2}$ of laser-flash TRMC using 500 (green circles) and 680 nm (blue squares) nanosecond laser as an excitation (left axis) are plotted as a function of PCBM content. 100 wt % PCBM represents the pure PCBM. $\Delta\sigma_{max}$ of Xe-flash TRMC using microsecond white light pulse are shown by red diamonds (right axis). (b) Thermal annealing effects on $\Delta\sigma_{max}$ of the Xe-flash TRMC. Closed circles, open squares, and closed triangles represent nonannealing and annealing at 120 and 160 °C for 10 min, respectively. Reprinted with permission from ref 15. Copyright 2013 American Chemical Society.

obtained upon exposure to 500 and 680 nm nanosecond laser pulses. Benefitting from probing vibrational motion of charge carrier by GHz electromagnetic wave, TRMC measurement provides with a direct observation of local charge carriers transport property in the materials. The larger $\Delta\sigma_{max}$ means the higher charge carrier mobility and charge carrier density, while the longer $\tau_{1/2}$ increases the probability of charge extraction before its deactivation such as charge recombination and trapping. Therefore the value of $\Delta\sigma_{max} \times \tau_{1/2}$ is a good indicator for optimization of processing condition, which has been proved to correlate with PCE of P3HT:phenyl-C_{61}-butyric acid methyl ester ($PC_{61}BM$) blends.[20] **P1**:$PC_{61}BM$ blend films were prepared by drop-casting from solutions in mixed solvent of chloroform (CF):chlorobenzene (CB) = 3:1 in weight fraction (w/w) onto a quartz plate without buffer layer. The mixing ratio of CB at 25 % is almost the upper limit of solubility for **P1**. The author examined CF solution without CB as well, but it gave seven times lower $\Delta\sigma_{max} \times \tau_{1/2}$ than the CF:CB mixture. For more specific evaluation of OPV, Xe-flash TRMC experiments using a 10 μs-width white light pulse (pseudo solar spectrum) from a Xe-flash lamp were conducted, where $\Delta\sigma_{max}$ includes not only the yield and local mobility of charge carriers but also their lifetime under the lower photo-irradiation density.[13] All of the curves in Figure 24a displayed a simple bell-shape dependence on the p/n blend ratio, the maxima of which locate at 60 - 75 wt% $PC_{61}BM$ (**P1**:$PC_{61}BM$ = 1:1.5 to 1:3). The thermal annealing at 120 and 160 ^{o}C for 10 min revealed suppression of the curves as shown in Figure 24b and Figure 25(a), indicative of the excessive phase separation or homogeneous mixing in the BHJ network. Accordingly the best PCE is expected at p/n = 1:2 to 1:3 in **P1**:$PC_{61}BM$ without thermal annealing.

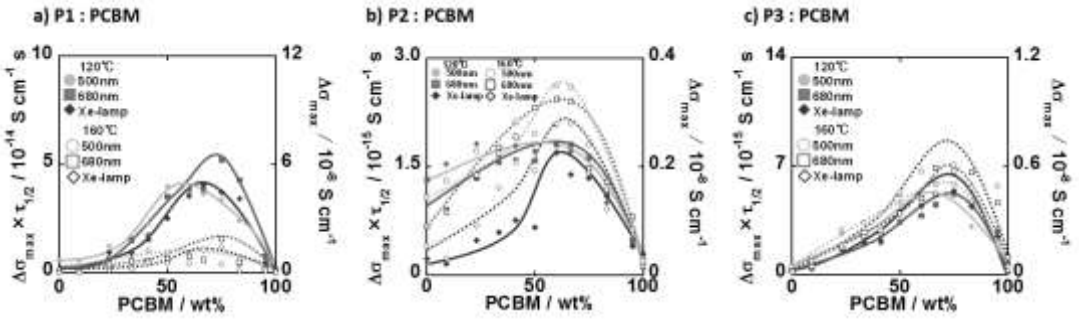

Figure 25. TRMC results of (a) **P1**:PCBM blend films prepared from CF:CB=3:1 w/w solutions (b) **P2**:PCBM blend films prepared from CB solutions and (c) **P3**:PCBM blend films prepared from CF:CB=1:1.5 solutions after thermal annealing. The solid and dotted lines correspond to 120 and 160 ^{o}C annealing, respectively. Reprinted with permission from ref 15. Copyright 2013 American Chemical Society.

Table 3 summarizes the OPV performances of **P1**:$PC_{61}BM$ processed with CF:CB = 3:1 mixed solvent. The best PCE of 0.87% (J_{sc} = 4.75 mA cm^{-2}, V_{oc} = 0.40, FF = 0.46) was obtained for a **P1**:$PC_{61}BM$ = 1:3 device without thermal annealing. **P1**:$PC_{61}BM$ = 1:1 and 1:2 blends resulted in the lower PCEs of 0.17-0.44%, and PCEs of 1:1 devices were decreased progressively with an increase of annealing temperature (0.17% for non-annealing, 0.16% for 120 °C, and 0.06% for 160 °C). Pure CF solutions were also tested, but the CF:CB mixture still gave nine-fold better PCE (PCE = 0.10%, p/n=1:3, no anneal). The trend found in these OPV devices is consistent with the TRMC results of Figure 24a-24b, iterating its essential feasibility in terms of speedy optimization and cross checking throughout the device fabrication.

Table 3. OPV performance of P1:$PC_{61}BM$.

p/n ratio	Solvent (w/w)	Anneal	PCE (%)	V_{oc} (V)	J_{sc} (mA cm^{-2})	FF
1:3	**CF:CB=3:1**	**-**	**0.87**	**0.40**	**4.75**	**0.46**
1:2	CF:CB=3:1	-	0.44	0.38	3.36	0.35
1:1	CF:CB=3:1	-	0.17	0.31	1.52	0.37
1:1	CF:CB=3:1	120 °C	0.16	0.31	1.36	0.38
1:1	CF:CB=3:1	160 °C	0.06	0.28	0.66	0.33
1:3	CF	-	0.10	0.32	0.73	0.44

Reprinted with permission from ref 15. Copyright 2013 American Chemical Society.

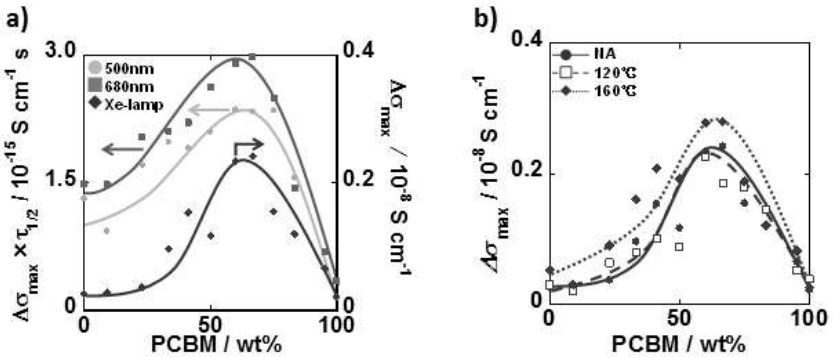

Figure 26. TRMC results of **P2**:PCBM blend films prepared by dropcasting CB solutions. (a) $\Delta\sigma_{max} \times \tau_{1/2}$ of laser-flash TRMC using 500 (green circles) and 680 nm (blue squares) nanosecond laser as an excitation (left axis) are plotted as a function of PCBM content. 100 wt % PCBM represents the pure PCBM. $\Delta\sigma_{max}$ of Xe-flash TRMC using microsecond white light pulse are shown by red diamonds (right axis). (b) Thermal annealing effects on$\Delta\sigma_{max}$ of the Xe-flash TRMC. Closed circles, open squares, and closed triangles represent nonannealing and annealing at 120 and 160 °C for 10 min, respectively. Reprinted with permission from ref 15. Copyright 2013 American Chemical Society.

3-4. Characterization of CPDT-TIDG polymer (P2).

The optoelectronic properties of **P2**:$PC_{61}BM$ blends were investigated in the same manner. Pure CB was adopted as a solvent because of enough high solubility of **P2** in CB without CF. Figure 26a plots the values of $\Delta\sigma_{max} \times \tau_{1/2}$ (laser-flash) or $\Delta\sigma_{max}$ (Xe-flash) as a function of $PC_{61}BM$ content, in which one maximum is observable at 60-67 wt% (**P2**:$PC_{61}BM$ = 1:1.5 to 1:2); however, the $\Delta\sigma_{max} \times \tau_{1/2}$ at $PC_{61}BM$ = 0 wt% is about half of the maximum. This is a sharp contrast to **P1** that indicated a drastic enhancement of $\Delta\sigma_{max} \times \tau_{1/2}$ with increasing $PC_{61}BM$ fraction (Figure 24a). Although the values of $\Delta\sigma_{max} \times \tau_{1/2}$ at $PC_{61}BM$ = 0 wt% were almost same for **P1** and **P2**, the maxima of their $PC_{61}BM$ blends are one order superior for **P1** compared with **P2**. The moderated increase in **P2** is simply explained by tedious increase of photocarrier generation yield upon addition of $PC_{61}BM$ because of the nearly constant $\tau_{1/2}$ over the range (Figure 27). The higher excitation density in TRMC measurement than that in OPV device characterization with 1 sun seems to be crucial to control the recombination processes between photo-generated electron and holes, giving considerable dependence in the conductivity signals in TRMC measurement with the transition from linear-sublinear dependence on the excitation density.[21] However, these copolymers showed almost constant recombination rate (Figure 27), suggesting strongly an unchanged relativity in the conductivity signals for the optimization of $PC_{61}BM$ concentration. This is suggestive of an ineffective photocurrent generation in the **P2** and $PC_{61}BM$ blend, due to, for example, the exciton deactivation by intermolecular charge transfer state,[22,23] photocurrent leak via prompt geminate charge recombination,[23,24] and deactivation of exciton before reaching donor:acceptor interface (details are discussed later). The thermal annealing at 120 and 160 ^{o}C for 10 min did not present a considerable change in the TRMC results (Figure 25b and Figure 26b). A weak saddle-like dependence is seen in Figure 26b, where 120 ^{o}C annealing yielded the

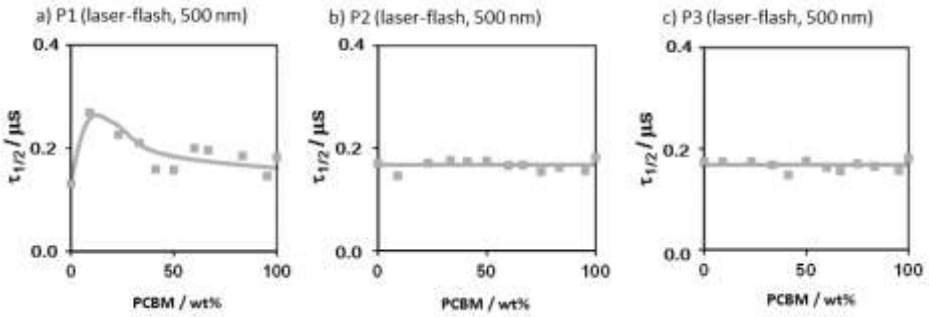

Figure 27. Half-lifetime of photoconductivity transients of a) **P1**:PCBM, b) **P2**:PCBM, and c) **P3**:PCBM blend films without anneal measured by laser-flash TRMC excited at 500 nm. Reprinted with permission from ref 15. Copyright 2013 American Chemical Society.

lowest $\Delta\sigma_{max}$. These surveys predict that the best device performance is given at **P2**:PCBM = 1:1.5 to 1:2, without thermal annealing or 160 ºC annealing.

Table 4 summarizes the OPV performance of **P2**:$PC_{61}BM$ processed from CB solutions. The best PCE of 0.23% was obtained for **P2**:PCBM = 1:2 (J_{sc} = 1.37 mA cm^{-2}, V_{oc} = 0.30, FF = 0.55) and 1:1.5 (J_{sc} = 1.23 mA cm^{-2}, V_{oc} = 0.31, FF =0.59) devices without thermal annealing. The annealing process at 120 and 160 ºC has a negative impact to some extent, resulting in PCE of 0.12 and 0.19%, respectively. Annealing at 160 ºC was slightly better than at 120 ºC, correlating to TRMC studies. **P2**:$PC_{61}BM$ = 1:1.5 devices demonstrated an almost similar trend (PCE = 0.23, 0.19, and 0.20% for non-annealing, 120, and 160 ºC, respectively), whereas the thermal annealing became less effective. On the other hand, changing of the p/n blend ratio at **P2**:$PC_{61}BM$ = 1:1 and 1:3 resulted in the decrease of OPV performances at 0.11% and 0.16%, respectively. These device data are in good correspondence with TRMC results.

Table 4. OPV performance of P2:PCBM.

p/n ratio	Solvent	Anneal	PCE (%)	V_{oc} (V)	J_{sc} (mA cm^{-2})	FF
1:2	**CB**	**-**	**0.23**	**0.30**	**1.37**	**0.55**
1:2	CB	120 ºC	0.12	0.32	1.07	0.49
1:2	CB	160 ºC	0.19	0.30	1.20	0.52
1:1.5	**CB**	**-**	**0.23**	**0.31**	**1.23**	**0.59**
1:1.5	CB	120 ºC	0.19	0.32	1.06	0.54
1:1.5	CB	160 ºC	0.20	0.32	1.13	0.55
1:1	CB	-	0.11	0.32	0.73	0.47
1:3	CB	-	0.16	0.31	0.99	0.53

3-5. Characterization of FLO-TIDG polymer (P3).

The transient photoconductivity maxima of **P3**:$PC_{61}BM$ blends are shown in Figure 28a. In the present case, mixture solution of CF:CB = 1:1.5 w/w was used, due to the low solubility of **P3**. The highest TRMC values were observed in the range from 67 to 75 wt% $PC_{61}BM$ (**P3**:$PC_{61}BM$ = 1:2 to 1:3). Upon thermal annealing at 120 and 160 ºC, the TRMC transient photoconductivity maxima curves were shifted downwards, suggesting the decrease of PCE by thermal treatment (Figure 28b and Figure 25c).

The OPV devices of **P3**:$PC_{61}BM$ were fabricated by following the pre-screening through TRMC measurement. The resultant device outputs are listed in

Table 5. The best performance of 1.42% (J_{sc} = 4.03 mA cm^{-2}, V_{oc} = 0.73, FF = 0.49) was found for **P3**:$PC_{61}BM$ = 1:2, which is superior to the other blends, 0.78% (**P3**:$PC_{61}BM$ = 1:1) , 1.17% (1:1.5), and 0.71% (1:2.5). This is in a good agreement with the TRMC prediction. However, the effect of thermal annealing is contrary to the device characterizations, where PCE was raised from 0.56% without annealing to 0.75% for 120 ºC and 1.42% for 160 ºC. The TRMC studies were performed on drop-casted thick films (ca. 1 μm), while the thin active layer in an OPV device was formed by spin-coating. Thus we examined spin-coated **P3**:$PC_{61}BM$ = 1:3 blend film (ca. 100 nm) on a PEDOT:PSS layer by Xe-flash TRMC; however, the same negative annealing effect was still observed (Figure 29a).

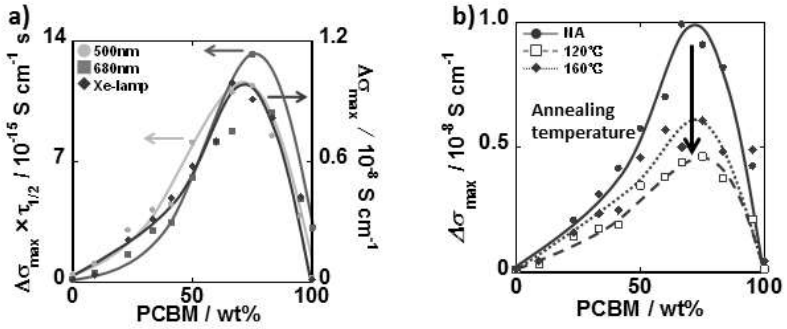

Figure 28. TRMC results of **P3**:$PC_{61}BM$ blend films prepared by dropcasting CF:CB = 1:1.5 w/w solutions. (a) $\Delta\sigma_{max} \times\tau_{1/2}$ of laser-flash TRMC using 500 (green circles) and 680 nm (blue squares) nanosecond laser as an excitation (left axis) are plotted as a function of $PC_{61}BM$ content. 100 wt % $PC_{61}BM$ represents the pure $PC_{61}BM$. $\Delta\sigma_{max}$ of Xe-flash TRMC using microsecond white light pulse is shown by red diamonds (right axis). (b) Thermal annealing effects on $\Delta\sigma_{max}$ of the Xe-flash TRMC. Closed circles, open squares, and closed triangles represent nonannealing and annealing at 120 and 160 °C for 10 min, respectively. Reprinted with permission from ref 15. Copyright 2013 American Chemical Society.

Table 5. OPV performance of P3:$PC_{61}BM$.

p/n ratio	Solvent (w/w)	Anneal	PCE (%)	V_{oc} (V)	J_{sc} (mA cm^{-2})	FF
1:1	CF:CB=1:1.5	-	0.57	0.74	2.52	0.30
1:1	CF:CB=1:1.5	160 ºC	0.78	0.75	2.53	0.41
1:1.5	CF:CB=1:1.5	160 ºC	1.17	0.74	3.02	0.52
1:2	CF:CB=1:1.5	-	0.56	0.58	2.27	0.43
1:2	CF:CB=1:1.5	120 ºC	0.75	0.69	2.71	0.40
1:2	**CF:CB=1:1.5**	**160 ºC**	**1.42**	**0.73**	**4.03**	**0.49**
1:2.5	CF:CB=1:1.5	160 ºC	0.71	0.73	2.18	0.45
1:1	CF 3v/v% DIO	-	0.85	0.70	3.70	0.33

Reprinted with permission from ref 15. Copyright 2013 American Chemical Society.

To elucidate the long-range charge transport property, hole mobilities (μ_h) of pristine **P3** film were measured by FET devices (Figure 29b). The best μ_h of 1.1 ×10 $^{-3}$ cm^2 V^{-1}s^{-1} was obtained for 20 μm channel length (L) without thermal annealing as reported previously.[5] It underwent an abrupt decrease to 4.1 ×10^{-4} cm^2 V^{-1} s^{-1} by widening L to 50 μm. FET characteristics failed to appear anymore for L > 100 μm. In contrast, the annealed samples at 200 °C exhibited almost constant μ_h of around 5 ×10^{-4} cm^2 V^{-1} s^{-1} irrespective of the channel length, indicating negligible contact resistance (transfer and output curves are provided in Appendix, Figure S1).[25] The significant decrease of μ_h with an elongation of L found for non-annealed film suggests that inter-grain connection is a predominant factor for the long range charge carrier mobility. The inter-grain connections rather than intra-grain crystallinity were most likely facilitated by thermal annealing process. This is consistent with the facts that X-ray diffraction pattern of pristine **P3** film did not change even after thermal annealing and **P3**:PC$_{61}$BM blends have apparent grain features in the AFM images (vide infra). Therefore, the exceptional mismatch between TRMC and OPV efficiency found in the annealing effect would be caused by the change in inter-grain connection, because TRMC is more sensitive to local mobility than the long-range one.

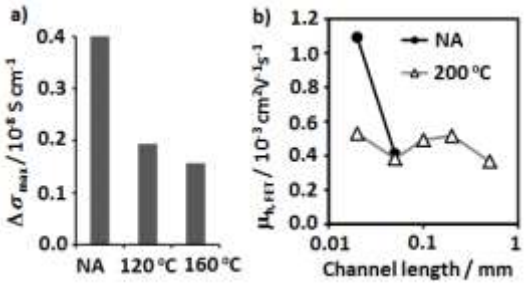

Figure 29. (a) Thermal annealing effect on **P3**:PC$_{61}$BM 1:2 film (ca. 100 nm) spun-coat on PEDOT:PSS layer measured by Xe-flash TRMC. (b) Channel length dependence of FET hole mobility of **P3**. The closed circles and open triangles correspond to nonannealed (NA) and annealed at 200 °C for 10 min samples, respectively. Reprinted with permission from ref 15. Copyright 2013 American Chemical Society.

3-6. Discussion through P1, P2, and P3.

3-6-1. V_{oc} vs. HOMO, light intensity dependence on J_{sc}, and EQE spectra.

To provide more insight into the device performances, they are discussed with HOMO levels, and TRMC results of **P1**, **P2**, and **P3**. Figure 30a shows a correlation between V_{oc} of PC$_{61}$BM-blended BHJ solar cells and HOMO levels of **P1**-**P3** along with typical p-type polymers, P3HT, [26] poly[*N*-9''-hepta-decanyl-2,7-carbazole-alt-5,5-

(4',7'-di-2-thienyl-2',1',3'-benzothiadiazole)] (PCDTBT),[27] poly[2,6-(4,4-bis-(2-ethyl hexyl)-4*H*-cyclopenta[2,1-*b*;3,4-*b*']dithiophene)-alt-4,7(2,1,3-benzothiadiazole)] (PCPDTBT),[28,29] and poly[4,8-bis-substituted-benzo[1,2-b:4,5-b']dithiophene-2,6-diyl-alt-4-substituted-thieno[3,4b]thiophene-2,6-diyl] (PTB7).[30,31] These established and high-efficient polymers indicate a linear relationship between V_{oc} and HOMO, which is well-documented that the maximum attainable V_{oc} is proportional to the energy difference between HOMO of p-type material and LUMO of n-type material with an empirical offset energy (0.3 eV) required for exciton dissociation.[32,33] In contrast, the slope interpolated for **P1**-**P3** is steeper than that of above mentioned polymers, despite V_{oc} is still proportional to HOMO levels. The V_{oc} was 0.61 V for PCPDTBT and 0.40 V for **P1**, although their HOMO levels are identical (-4.9 eV). The 0.21 eV loss found in **P1** is assumed in part as a result of nongeminate recombination that is also relating to the decrease of J_{sc} and FF.[34,35] This is supported by the fact that the device output of **P1** (J_{sc} = 4.75 mA cm^{-2}, FF = 0.46) is much lower than the high-efficient PCPDTBT (J_{sc} = 10 - 16 mA cm^{-2}, FF = 0.43-0.55). In addition, the laser-flash TRMC transients of **P1**:$PC_{61}BM$ blend exhibited a slightly shorter half-lifetime (ca. 0.2 μs) than P3HT:PCBM (0.3-0.5 μs)[12] and PCPDTBT:PCBM (0.3 μs)[13] under the same photoexcitation density. The current density-voltage curves of the best OPV performances in Figure 30b are an intuitive representation of this discussion on the loss. The photocurrent under the reverse bias (< 0V) is still increasing in **P1**, as evident from the low shunt resistance (R_{sh}, 0.38 kΩ cm^2). Meanwhile, the increase of photocurrent of **P3** is moderate, accompanying by the higher FF (0.49) and R_{sh} (0.62 kΩ cm^2).

Figure 30c shows the light intensity dependence on J_{sc} of the optimized devices. The solid lines are interpolated curves expressed by $J_{sc} = A\, I^{\alpha}$, where A is a constant, I is

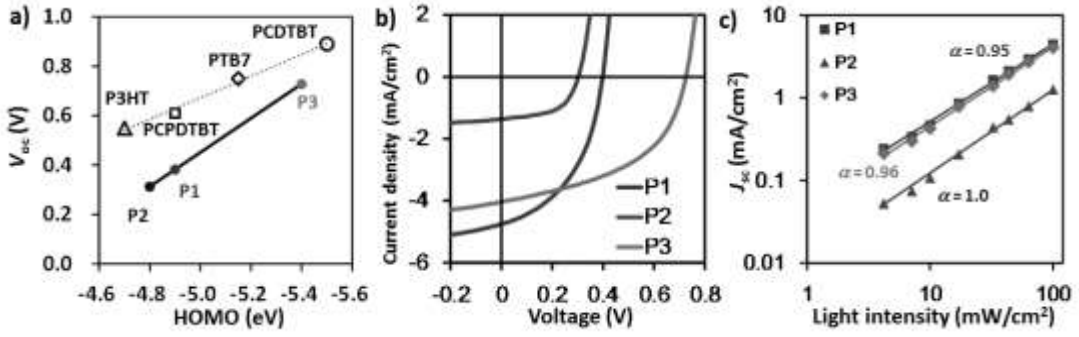

Figure 30. (a) Correlation of V_{oc} with HOMO levels of the polymers. (b) *J*−*V* curves of the best PCE of the respective polymers. **P1** (p/n = 1:3, CF:CB = 3:1, without thermal annealing). **P2** (p/n = 1:1.5, CB, without thermal annealing). **P3** (p/n = 1:2, CF:CB = 1:1.5, with 160 °C annealing). (c) Light intensity (I) dependence on J_{sc}. The α is an exponent of $J_{sc} = A\, I^{\alpha}$ fitting. Reprinted with permission from ref 15. Copyright 2013 American Chemical Society.

a light intensity, and α is an exponent. An unity of α means a weak nongeminate recombination.[36] **P1**, **P2**, and **P3** indicate α = 0.95, 1.0, and 0.96, respectively, and therefore nongeminate recombination loss is negligible for **P2**. At $V = V_{max}$ corresponding to the highest power generation point given by FF=($J_{max}V_{max}$)/($J_{sc}V_{oc}$), the fitting by $J_{max} = A\ I^{\alpha}$ resulted in α of 0.93 (**P1**), 1.0 (**P2**), and 0.95 (**P3**), where **P1** and **P3** were further decreased by 0.02 and 0.01 in spite of the constant and unity α of **P2**. This is suggestive of the involvement of nongeminate recombination loss, in particular for **P1**.

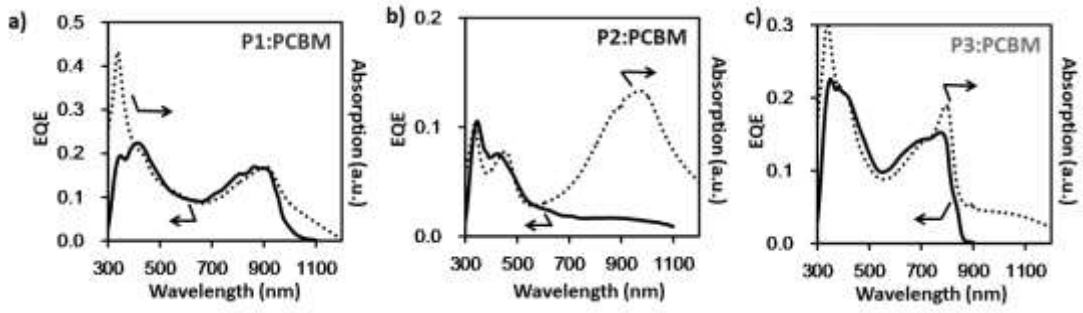

Figure 31. EQE spectra of the optimized devices (solid lines, left axis) superimposed by respective device absorption spectra (dotted lines, right axis). Note that absorption of glass/ITO is subtracted but that of PEDOT:PSS is included. Reprinted with permission from ref 15. Copyright 2013 American Chemical Society.

The external quantum efficiency (EQE) spectra of the optimized **P1**-**P3**:$PC_{61}BM$ devices are shown in Figure 31a–Figure 31c, with the superimposition of their absorption spectra. It should be noted that EQE spectra of **P1** and **P3** match their electronic absorption spectra, while absorption of **P2** does not effectively contribute to the current generation. The calculated J_{sc} from the EQE spectrum, J_{sc}^{EQE}, are 5.03, 1.18, and 4.00 mA cm^{-2} for **P1**, **P2**, and **P3**, whereas J_{sc}/ J_{sc}^{EQE} are 0.95, 1.08, and 1.01, respectively. **P3** shows the excellent correspondence between J_{sc} and J_{sc}^{EQE} with only 1% difference, indicating the precise evaluation of the device. On the other hand, the smallest J_{sc}/J_{sc}^{EQE} of 0.95 found for **P1** implies that nongeminate recombination loss may be involved, because J_{sc}^{EQE} is reconstructed from the photo-response against respective low-power monochromated light. This is consistent with the abovementioned light power dependence on J_{sc} and J_{max}, and the slightly small slope in Figure 30c for **P1** than that in **P3** is also supportive to the loss in case of the higher excitation density. The 8% higher J_{sc} than J_{sc}^{EQE} observed for **P2** is explained by the technical reason that the upper limit of our EQE measurement instrument is 1100 nm and the photocurrent generation at longer wavelength is not included in the J_{sc}^{EQE}

calculation (Figure 31b).

From the detailed device characterizations, nongeminate recombination is negligible for **P2**, but its contribution to the current loss is suggested in the case of **P1**. The V_{oc} loss is relatively high for the TIDG-based polymers compared with high efficient polymers ever reported. Importantly, the electronic absorption of **P2** polymer in the NIR region does not effectively generate photocurrent, the cause of which is discussed in the section 3-7.

3-6-2. Film morphology and orientation

Photo-generated charge transport in the active layer of BHJ structures is strongly dependent on its nanomorphology resulting from phase segregation, and the presence of non-homogeneous ultra-thin skin layer was suggested to impact phtoresponce of the OPVc system,[37] which could not be assessed by surface-topographic observation of AFM. The thin film and surface morphology of the active layers of **P1**~**P3** were examined by two-dimensional grazing-incidence X-ray diffraction (2D-GIXRD) and AFM, as given Figure 32 and Figure 33, respectively. 2D-GIXRD displays images of pristine **P1**, **P2**, and **P3** films (left panel) and their blends with $PC_{61}BM$ (right panel) prepared by device-optimized procedure. Pristine **P1** film highlights the face-on orientation with π-π stacking distance of 3.63 Å and inter-lamellar distance of 17.0 ~ 17.9 Å (Figure 32a), reflecting the planar BDT unit and polymer backbone of **P1**.[5] **P1**:PCBM film partially preserves the face-on orientation; however, the orientation was converted to bimodal (mixture of face-on and edge-on, Figure 32b). Pristine **P2** film shows a bimodal feature consisting of π-π stacking distance of 3.82 Å and inter-lamellar distance of 12.9 Å (Figure 32c) with weaker diffraction intensities than **P1**, coincident with the side-alkyl chains perpendicular to the

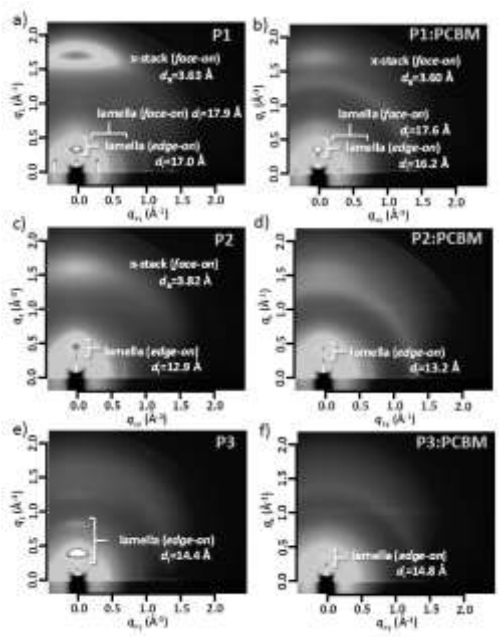

Figure 32. 2D-GIXRD images of the pristine polymers (left panel) and PCBM blend films of the optimized condition (right panel). (a,b) **P1**, (c,d) **P2**, and (e,f) **P3**. Reprinted with permission from ref 15. Copyright 2013 American Chemical Society.

CPDT plane which prevents intermolecular stacking. Mixing with $PC_{61}BM$ led to extinction of π-π stacking diffraction peak and decrease in the magnitude of inter-lamellar diffraction (Figure 32d). In contrast to **P1** and **P2**, a complete edge-on orientation was observed for **P3** with the first and second diffraction peaks corresponding to the inter-lamellar distance of 14.4 Å (Figure 32e). The situation was same for the $PC_{61}BM$ blend, while the peak intensity was further decreased (Figure 32f). These polymer orientation properties are summarized in Table 6.

Table 6. 2D-GIXRD summary of P1, P2, and P3.

Film (p/n ratio)	Orientation	π–π distance (Å)	Inter-lamellar distance (Å)
P1	face-on	3.63	17.0, 17.9
P1:$PC_{61}BM$ (1:3)	bimodal	3.60	16.2, 17.6
P2	bimodal	3.82	12.9
P2:$PC_{61}BM$ (1:1.5)	bimodal (weak)	-	13.2
P3	edge-on	-	14.4
P3:$PC_{61}BM$ (1:2)	edge-on (weak)	-	14.8

Reprinted with permission from ref 15. Copyright 2013 American Chemical Society.

The impact of thermal treatment was investigated for pristine **P1**, **P2**, and **P3** thick films. **P1** gave the most intense XRD peak at $2\theta = 5.1^{o}$ (d spacing of 17 Å), corresponding to the intermolecular distance interdigitated by the side alkyl chains. The intensity was reduced by 30% upon thermal annealing at 160 °C, being in line with the TRMC and OPV results. On the other hand, **P2** and **P3** indicate weak peaks at $2\theta = 6.7^{o}$ (d = 13 Å) and 6.0^{o} (d =15 Å), respectively. These inter-lamellar distances are consistent with those found in 2D-GIXRD (Figure 32). The thermal annealing did not give a significant change in the diffraction spectra for **P2** and **P3**, in agreement with the TRMC results.

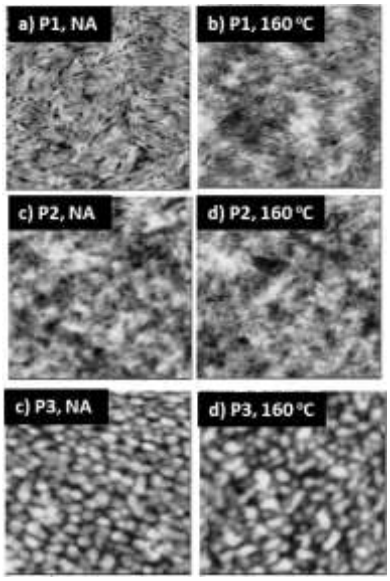

Figure 33. AFM height images (2 × 2 μm) of (a,b) **P1**:PCBM 1:3, (c,d) **P2**:PCBM 1:1.5, and (e,f) **P3**:PCBM 1:2. (a,c,e) No thermal annealing. (b,d,f) Thermal annealing at 160 °C for 10 min. Reprinted with permission from ref 15. Copyright 2013 American Chemical Society.

The highest crystalline nature of **P1** is also dictated from atomic force microscope (AFM) images. Figure 33

displays the AFM topological images of **P1**:$PC_{61}BM$ = 1:3, **P2**:$PC_{61}BM$ = 1:1.5, and **P3**:$PC_{61}BM$ = 1:2 films with and without thermal annealing at 160 ^{o}C. The corresponding phase images are shown in Figure S2. **P1** exhibits the crystalline fiber-like structures which become smaller and more miscible after thermal annealing. With respect to **P2**, no clear phase separation is seen regardless of thermal annealing, indicating the formation of BHJ structure at nanometer dimension. Spherical aggregations on one-hundred-nanometer scale appeared in **P3**, the size and shape of which did not change at all before and after thermal annealing. It is striking to note that such an aggregation is exactly an inferior example of BHJ, but the highest PCE was obtained for **P3**. This excessive phase separation in **P3** suggests the possibility of further improvement in PCE and thus, the author examined incorporation of solvent additive of 3 v/v% 1,8-diiodeocatne (DIO)[38] into CF for **P3**:$PC_{61}BM$ = 1:1 device. A marginal improvement of PCE from 0.57% to 0.85% was found (Table 5), which is mainly due to the increase of J_{sc} from 2.52 to 3.70 mA cm^{-2}. The morphology was, however, still far from an ideal structure (Figure S3).

From the AFM and 2D-GIXRD studies, **P1** was found to possess high crystallinity with face-on orientation and nanofiber-like structure. **P2** is rather amorphous with bimodal orientation, but the BHJ network is likely most optimized among the three polymers. **P3** shows edge-on orientation and large domain structure, both of which are apparently disadvantageous for OPV performance.

3-7. Transient absorption spectroscopy.

To gain access to spectroscopic and kinetic information on exciton and charge carriers, the author conducted transient absorption spectroscopy (TAS)[14] for the pristine and blend films. The transient absorption (TA) spectra of pristine **P1** through **P3** films upon excitation at 800 nm (**P1** and **P2**) or 600 nm (**P3**) are shown in Figure 34a-Figure 34c. At the end-of-pulse all of the polymers indicate the broad absorption spectra in the infrared region and bleaching in their steady-state absorption areas. Both TA and bleaching have comparable time evolutions, clearly indicative of the existence of sole intermediate. By comparing with TA spectra of polymer:$PC_{61}BM$ blends (vide infra) and observed short lifetime, the author can safely ascribe this species to polymer singlet exciton. Figure 34d presents the kinetic decays of singlet excitons of **P1-P3** at each absorption maximum. Multi-exponential analysis gave the average lifetimes of 3.1 ps (**P1**), 0.64 ps (**P2**), and 20 ps (**P3**) at room temperature (Table 7). In addition to the observed one order smaller exciton lifetime of **P3** than typical conjugated polymers (a

few hundreds of picosecond),[39] it is noteworthy that the NIR absorbing polymers, **P1** and **P2**, show extremely short exciton lifetime. The lifetime of the lowest bandgap polymer, **P2**, is competitive even with the time required for exciton diffusion to the donor–acceptor interface.

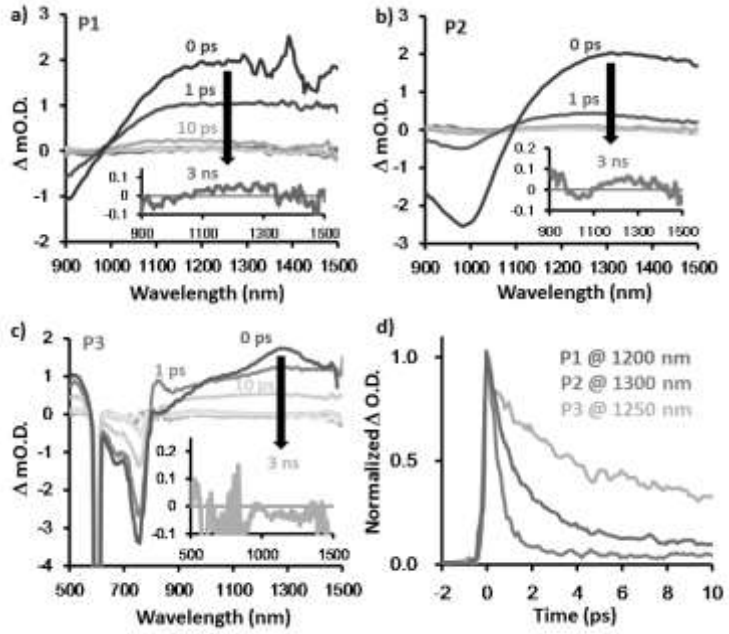

Figure 34. TA spectra of (a) pristine **P1**, λ_{ex} = 800 nm; (b) pristine **P2**, λ_{ex} = 800 nm; and (c) pristine **P3**, λ_{ex} = 600 nm. The laser power was 5 μJ cm^{-2} pulse^{-1}. The delay times are 0, 1, 10, 100, and 1000 ps corresponding from the dark to bright colors. The inset shows the TA at 3 ns (bold line). (d) Decay profiles at the TA maxima of **P1** (1200 nm), **P2** (1300 nm), and **P3** (1250 nm). They are ascribed to polymer singlet exciton. Reprinted with permission from ref 15. Copyright 2013 American Chemical Society.

Table 7. Lifetime analysis of polymer singlet exciton.

Polymer	A_1 (%)	τ_1 (ps)	A_2 (%)	τ_2 (ps)	τ_{ave} (ps)
P1	73	1.0	27	8.6	3.1
P2	100	0.64	-	-	0.64
P3	55	3.3	45	40	20

Reprinted with permission from ref 15. Copyright 2013 American Chemical Society.

The time-evolution of TA spectra of the $PC_{61}BM$ blends are shown in Figure 35a-Figure 35c. The same excitation wavelengths with Figure 34 were used, so that the polymer rather than $PC_{61}BM$ is selectively excited. The TA spectra of **P1** and **P2** at 0 ps are identical to those observed in pristine polymers, readily ascribed to singlet exciton; however, the long-lifetime components appears in the blend films at > 10 ps delay

(Figure 35d). By considering the short singlet lifetime that cannot allow conversion to triplet state and more than 100 ~ 200 nm longer wavelength than $PC_{61}BM$ radical anion (λ_{max} = 1020 nm, $\varepsilon = 6 \times 10^3$ dm^3 mol^{-1} cm^{-1}),[40] the author assigned the long-lifetime absorption to the polymer radical cation. This assignment is in accordance with the increase of TA intensity upon addition of $PC_{61}BM$. With respect to **P3**:$PC_{61}BM$, it contains both singlet exciton at 1250 nm and radical cation at 1000 nm even at 0 ps (Figure 35c), indicating the prompt charge separation within the instrument response time. A pronounced spectrum change from singlet at 1250 nm to radical cation at 1000 nm is clearly observed with the time evolution, iterating charge separation from polymer singlet exciton. It is noteworthy that the kinetic traces of radical cations (polarons) on **P1**:$PC_{61}BM$ and **P2**:$PC_{61}BM$ are overlapped with each other, as well as identical lifetimes of the charge carriers observed for both **P1**:$PC_{61}BM$ and **P2**:$PC_{61}BM$ in TRMC measurements. Only the differences in these systems are rather shorter lifetime in excitons on **P2** as confirmed in TAS for pristine state, and this is the case giving the negligible contribution of the excitons on **P2** to the EQE spectrum of **P2**:$PC_{61}BM$ (Figure 31b).

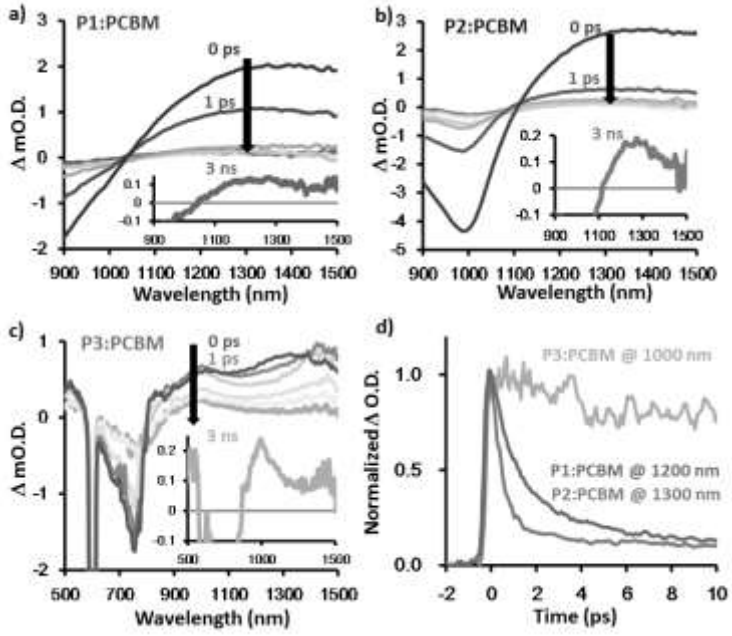

Figure 35. TA spectra of (a) **P1**:$PC_{61}BM$ (p/n 1:3), λ_{ex} = 800 nm, (b) **P2**:$PC_{61}BM$ (p/n 1:1.5), λ_{ex} = 800 nm, and (c) **P3**:$PC_{61}BM$ (p/n 1:2), λ_{ex} = 600 nm. The laser power was 10 μJ cm^{-2} pulse^{-1} for **P1** and **P2** and 5 μJ cm^{-2} pulse^{-1} for **P3**. The delay times are 0, 1, 10, 100, and 1000 ps corresponding from the dark to bright colors. The inset shows the TA at 3 ns (bold line). (d) Decay profiles at the TA maxima of **P1** (1200 nm), **P2** (1300 nm), and **P3** (1000 nm). They are ascribed to polymer singlet exciton (fast decay) and polymer radical cation (long tail). Reprinted with permission from ref 15. Copyright 2013 American Chemical Society.

Figure 36a-Figure 36c exhibit TAS results using a 400 nm laser which excites both polymer and $PC_{61}BM$. The spectral feature and time-evolution of **P3**:$PC_{61}BM$ are almost identical to those induced by exposure at 600 nm (Figure 35c), indicating normal charge separation from both **P3** and $PC_{61}BM$ singlet excitons. The TA spectra of **P1**:$PC_{61}BM$ and **P2**:$PC_{61}BM$ (Figure 36a and Figure 36b) at 0 ps are basically similar to the 800 nm excitation (Figure 35a and Figure 35b) and those at 3 ns delay are perfectly identical to the radical cations of the polymers (Figure 35a-Figure 35c). The normalized kinetics of polymer:$PC_{61}BM$ within 10 ps are presented in Figure 36d. The fraction of the fast decay (< 2 ps, polymer singlet exciton) relative to the tailing component (polymer radical cation) is reduced, because excitation at 400 nm produces both polymer and PCBM singlet excitons, which decreases the initial yield of polymer singlet exciton.

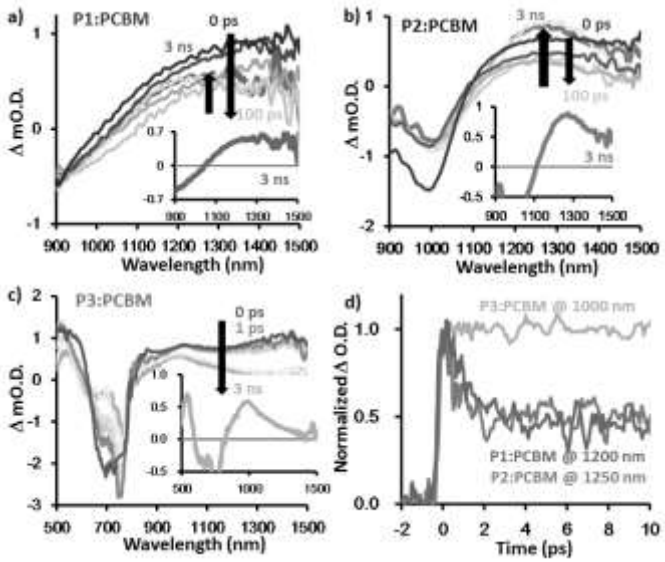

Figure 36. TA spectra of (a) **P1**:$PC_{61}BM$ (p/n 1:3), (b) **P2**:$PC_{61}BM$ (p/n 1:1.5) and (c) **P3**:$PC_{61}BM$ (p/n 1:2). The λ_{ex} = 400 nm for all films. The laser power was 30 μJ cm^{-2} $pulse^{-1}$ for **P1** and **P2** and 5 μJ cm^{-2} $pulse^{-1}$ for **P3**. The delay times are 0, 1, 10, 100, and 1000 ps corresponding from the dark to bright colors. The inset shows the TA at 3 ns (bold line). (d) Decay profiles at the TA maxima of **P1** (1200 nm), **P2** (1250 nm), and **P3** (1000 nm). They are ascribed to polymer singlet exciton (fast decay) and polymer radical cation (long tail). Reprinted with permission from ref 15. Copyright 2013 American Chemical Society.

Notably, rising kinetics from 100 ps to 1 ns were found for the 400 nm excitation of **P1**:$PC_{61}BM$ and **P2**:$PC_{61}BM$ (Figure 37a), which was not observed for the selective polymer excitation (Figure 37b). An exponential analysis revealed the rise time of 880 and 460 ps for **P1** and **P2**, respectively. These are reasonable values for the delayed charge formation from $PC_{61}BM$ singlet exciton (the lifetime was reported to be

ca. 1 ns) [41,42] expressed by

$$^{1}PCBM^{*} + Polymer \rightarrow PCBM^{-} + Polymer^{+} \quad (1).$$

The faster rise time of **P2** than **P1** is presumably due to its more homogeneous p/n mixing (Figure 33) which facilitates efficient diffusion of PCBM exciton to the p/n interface. The charge separation from PCBM singlet exciton is relevant to the photocurrent generation of the EQE spectra at the PCBM absorption. This infers that enhancing exciton diffusion length and charge separation efficiency in PCBM domains can improve the photocurrent generation efficiency in spite of the excessively shortened singlet exciton lifetime of the low bandgap polymers.

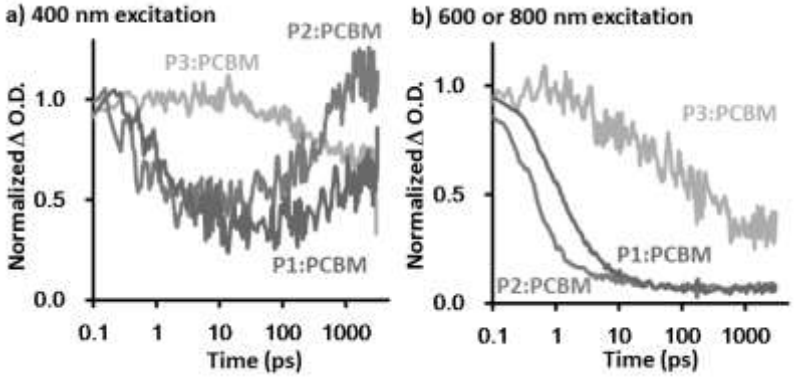

Figure 37. Normalized kinetics of **P1**:$PC_{61}BM$ (p/n 1:3), **P2**:$PC_{61}BM$ (p/n 1:1.5), and **P3**:$PC_{61}BM$ (p/n 1:2) at each absorption maximum. (See Figure 35 and Figure 36.) (a) λ_{ex} = 400 nm and (b) λ_{ex} = 800 nm for **P1** and **P2**, 600 nm for **P3**. Reprinted with permission from ref 15. Copyright 2013 American Chemical Society.

In wrapping up section 3.7, **P1** demonstrated a highly-crystalline nature and face-on orientation, giving the highest TRMC signal and J_{sc} (4.75 mA cm^{-2}); however, nongeminate recombination is supposed to deteriorate J_{sc} and FF (0.46) as inferred from light intensity dependence. This is underlined by that the boundaries among the crystalline fibers impaired the FET hole mobility (0.34×10^{-3} cm^2 V^{-1} s^{-1}). The bandgap of **P2** is excessively narrowed to 1.0 eV along with shallow HOMO level. TRMC signal was the lowest even in the presence of high amount of PCBM, due to the short singlet exciton lifetime (0.64 ps) revealed by TAS, which is competitive with charge separation. These properties and optical window in the visible region led to the lowest V_{oc} (0.30 V) and J_{sc} (1.37 mA cm^{-2}) in spite of a relatively high FF (0.55-0.59) and FET hole mobility (5.3×10^{-3} cm^2 V^{-1} s^{-1}). Although **P3** possesses appropriate HOMO-LUMO levels and moderate FET hole mobility (1.1×10^{-3} cm^2 $V^{-1}s^{-1}$), satisfied OPV efficiency

has not been achieved due to the inferior BHJ network and edge-on orientation. An emphasis is given to that LUMO levels of **P1**-**P3** are almost constant at -3.8 eV regardless of the coupled donor units, which is close to the LUMO of ideal polymer (-3.9 eV) and indicative of the benefit of TIDG. We believe that an appropriate selection of donor units and solubilizing side chains, that concurrently ensure the deep HOMO and optimized BHJ network, could enhance the OPV performance of TIDG-based copolymers.

3-8. Conclusion

OPV devices were characterized with low-band gap polymers bearing a novel electron accepting moiety, TIDG. The optoelectronic properties of blend films of **P1** (TIDG-BDT), **P2** (TIDG-CPDT), and **P3** (TIDG-FLO) with $PC_{61}BM$ were investigated by laser and Xe-flash TRMC, which served effectively as a pre-screening and cross-checking of p/n blend ratio, thermal annealing, and solvent choice. The maximized PCE of **P1**, **P2**, and **P3** were 0.87, 0.23, and 1.42% at p/n=1:2-1:3, respectively. The highest J_{sc} was obtained for **P1**, concomitant with the largest TRMC signal by virtue of face-on orientation and high crystallinity. Rather amorphous-like **P2** had a moderate mixing with $PC_{61}BM$, the highest FET mobility, and the superior FF; however, TRMC and OPV revealed the worst. Along with the lowest V_{oc}, the primary cause is the extremely short singlet lifetime of the polymer (0.64 ps) which suppresses the EQE at the polymer absorption. Interestingly, delayed charge formation from $PC_{61}BM$ singlet exciton was observed in the TAS studies of **P1** and **P2** at 400 nm excitation. **P3** presented balanced J_{sc}, V_{oc}, and FF, consequently the highest PCE. However, a large phase separation was observed and not fully mitigated by thermal annealing and solvent additive. Despite the unsatisfied PCEs of the novel TIDG-based polymers, their LUMO levels are fixed at around -3.8 eV, which is only 0.1 eV above from the *ideal* OPV polymer. Engineering alkyl side chain and/or replacing coupled donor unit could improve the PCE. Thus the author anticipates further evolution of the TIDG families, by rational designing of counter donor and solubilizing group. Importantly, the author elucidated that singlet exciton lifetimes of the polymers were significantly short, which might be intimately related to their NIR absorbing properties and must be considered in their photocurrent generation mechanisms.

3-9. Experimental

General. Steady-state photoabsorption spectroscopy was performed using a Jasco V-570 UV-vis spectrophotometer. Molecular weights of polymers were determined using the gel permeation chromatography (GPC) method with polystyrene standards. GPC analysis was performed with polymer/ tetrahydrofuran (THF) (HPLC grade) solution at a flow rate of 1 cm^3 min^{-1} at 40 ˚C, on a HITACHI L-2130, L-2455, L-2530 chromatography instrument with Shodex KF-804L/ KF-805L (Shodex Co., Japan) connected to a refractive index detector. PYS experiments were carried out by a RIKEN Keiki Co. Ltd. model AC-2. XRD measurements were done on a Rigaku RINT ultra X18SAXS-IP (Cu Kα: 1.5418 Å). GIXRD experiments were conducted at the SPring-8 on the beam line BL19B2 using 12.39 keV (λ = 1 Å) X-ray. The GIXRD patterns were recorded with a 2-D image detector (Pilatus 100K).[43] AFM observations were performed by a Seiko Instruments Inc. model Nanocute OP and Nanonavi II.

Materials. The polymers were synthesized according to our previous reports.[5] $PC_{61}BM$ and solvents were purchased from Frontier Carbon Inc. and Kishida Chemical Inc., respectively, and used as received.

Time-resolved microwave conductivity (TRMC). A resonant cavity was used to obtain a high degree of sensitivity in the conductivity measurement. The resonant frequency and microwave power were set at ca. 9.1 GHz and 3 mW, respectively, so that the electric field of the microwave was sufficiently small to not disturb the motion of charge carriers. Nanosecond laser pulse at 500 nm and 680 nm from an optical parametric oscillator (Continuum Inc., Panther) seeded by third harmonic generation (THG; 355 nm) of a Nd:YAG laser (Continuum Inc., Surelite II, 5-8 ns pulse duration, 10 Hz) or microsecond white light pulse from a Xe flash lamp was used as an excitation source. The photoconductivity $\Delta\sigma$ was obtained by $\Delta P_r/(AP_r)$, where ΔP_r, A, and P_r are the transient power change of reflected microwave from a cavity, the sensitivity factor, and the reflected microwave power, respectively. The nanosecond laser intensity at 500 and 680 nm were set at 2.5 mJ cm^{-2} $pulse^{-1}$ (6.4×10^{15} and 8.7×10^{15} photons cm^{-2} $pulse^{-1}$), respectively. The power of the white light pulse was 0.3 mJ cm^{-2} $pulse^{-1}$. The samples were drop-casted on a quartz plate from solutions of polymer and $PC_{61}BM$ and dried in a vacuum oven. After the preparation of thin films, the films were thermally annealed on a hot plate. The TRMC experiments were performed under an ambient condition at room temperature.

Organic photovoltaic cell (OPV). A PEDOT:PSS layer was cast onto the cleaned ITO layer by spin-coating after passing through a 0.45 μm filter. The substrate was annealed on a hot plate at 120 °C for 10 min. After the substrate was annealed on a hot plate at

180 °C for 10 min, an active layer were cast on top of the PEDOT:PSS buffer layer in a nitrogen glove box by spin-coating after passing through a 0.2 μm filter. The thickness was around 100 nm. A cathode consisting of 10 nm Ca and 100 nm Al layers was sequentially deposited through a shadow mask on top of the active layers by thermal evaporation in a vacuum chamber. The resulting device configuration was ITO (120-160 nm)/PEDOT:PSS (45-60 nm)/active layer (ca. 100 nm)/Ca (10 nm)/Al (100 nm) with an active area of 7.1 mm^2. Current-voltage (*J*-*V*) curves were measured using a source-measure unit (ADCMT Corp., 6241A) under AM 1.5 G solar illumination at 100 mW cm^{-2} (1 sun, monitored by a calibrated standard cell, Bunko Keiki SM-250KD) from a 300 W solar simulator (SAN-EI Corp., XES-301S). The EQE spectra were measured by a Bunko Keiki model BS-520BK equipped with a Keithley model 2401 source meter. The monochromated light power was calibrated by a silicon photovoltaic cell, Bunko Keiki model S1337-1010BQ.

Field-effect transistor (FET). FETs were fabricated in a top-contact configuration on a heavily n-doped Si wafer with 200 nm thermally grown SiO_2 (the capacitance per unit area of the gate dielectric layer is C_i = 17.3 nF cm^{-2}). The substrate surface were treated with piranha solution for 10 min, subjected to cleaning using ultrasonication in deionized water (twice), and isopropanol (twice). The cleaned substrates were dried then treated with UV/ozone for 20 min. Thin films of the copolymer were spin-coated on the treated substrates from chloroform solution. On top of the organic film, about 50 nm thick gold was deposited as source and drain contacts through a shadow mask. The channel width (*W*) of drain and source is 3 mm. Characteristics of the FET devices were measured in a vacuum chamber at room temperature with a Keithley 4200-SCS semiconductor analyzer system.

Transient absorption spectroscopy (TAS). The pump and probe femtosecond transient absorption spectroscopy system consists of a transient absorption spectrometer (Ultrafast Systems, Helios) and a regenerative amplified Ti:sapphire laser (Spectra-Physics, Hurricane). The amplified Ti:sappire laser provided 800-nm fundamental pulses at a repetition rate of 1 kHz with an energy of 0.8 mJ and a pulse width of 100 fs (FWHM), which were split into two optical beams with a beam splitter to generate pump and probe pulses. One fundamental beam was converted into pump pulses at 400 nm with a second harmonic generator (Spectra-Physics, TP-F) or pump pulses at other wavelengths with an ultrafast optical parametric amplifier (Spectra-Physics, TOPAS). The other fundamental beam was converted into white light continuum pulses employed as probe pulses in the wavelength region from 400 to 1700 nm. The details of the system have been reported in the literature.[14]

Appendix

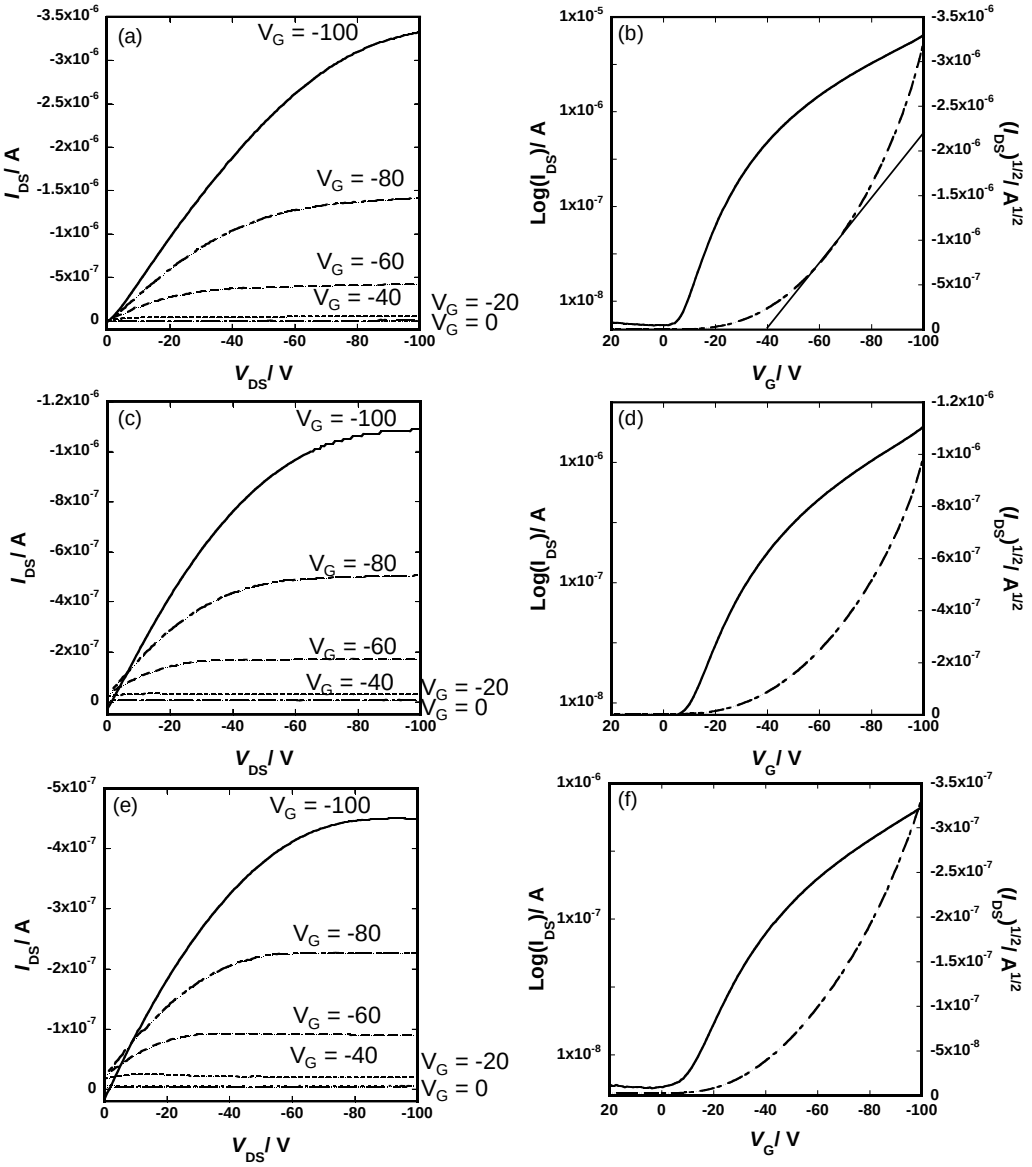

Figure S1. FET current-voltage characteristics of **P3**. The channel lengths were (a)(b) 20 μm, (c)(d) 50 μm, and (e)(f) 200 μm; the channel width: *W* was 3 mm; the film thicknesses were around 60 nm. Figures (a), (c), and (e) are output curves at different gate voltages (0 to - 100 V or -80 V); (b),(d), and (f) are the transfer curves. The capacitance: Ci of the device was 17.3 nF cm^{-2}. All the measurements were carried out at room temperature. Reprinted with permission from ref 15. Copyright 2013 American Chemical Society.

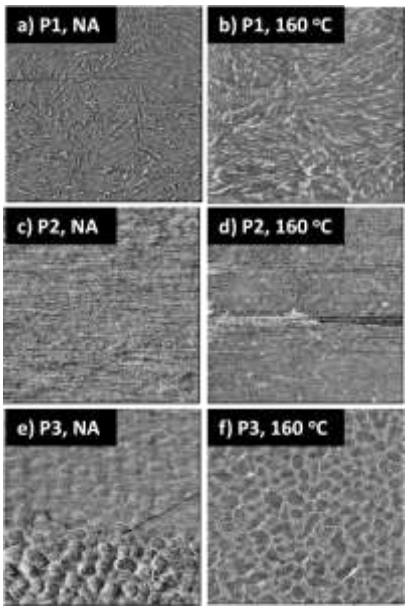

Figure S2. AFM phase images (2 × 2 μm) of a) b) **P1**:$PC_{61}BM$=1:3, c) d) **P2**:$PC_{61}BM$=1:1.5, and e) f) **P3**:$PC_{61}BM$=1:2. a) c) and e) no thermal annealing. b) d) f) thermal annealing at 160 ºC for 10 min. Reprinted with permission from ref 15. Copyright 2013 American Chemical Society.

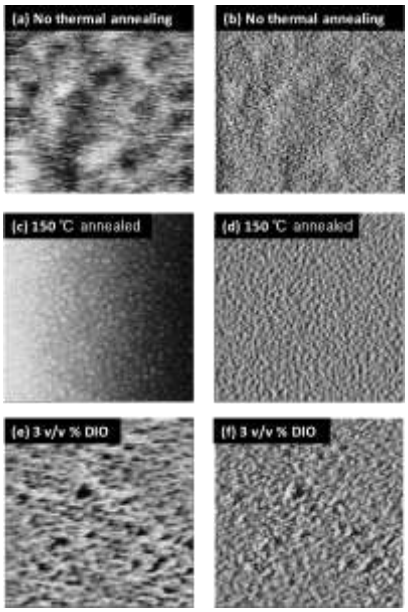

Figure S3. AFM images (4 × 4 μm) of **P3**:$PC_{61}BM$ = 1:1 with a) b) no thermal annealing, c) d) thermal annealing at 150 ºC for 10 min, and e) f) used the 3 v/v % DIO as additives and no thermal annealing. a) c) and e) topological images. b) d) f) phase images. Reprinted with permission from ref 15. Copyright 2013 American Chemical Society.

References

[1] Dou, L.; Liu, Y.; Hong, Z.; Li, G.; Yang, Y. *Chem. Rev*. **2015**, *115*, 12633−12665.

[2] Scharber , M. C.; Mühlbacher, D.; Koppe , M.; Denk , P.; Waldauf, C. Heeger, A. J.; Brabec, C. J. *Adv. Mater.* **2006**, *18*, 789-794.

[3] Zhou, E.; Wei, Q.; Yamanaka, S.; Zhang, Y.; Tajima, K.; Yang, C.; Hashimoto, K. *Macromolecules*, **2010**, *43*, 821-826.

[4] C.-C. Chen, W. -H. Chang, K. Yoshimura, K. Ohya, J. You, J. Gao, Z. Hong, Y. Yang *Adv. Mater*. **2014**, *26*, 5670–5677.

[5] Koizumi, Y.; Ide, M.; Saeki, A.; Vijayakumar, C.; Balan, B.; Kawamoto, M.; Seki, S. Thienoisoindigo-Based Low-Band Gap Polymers for Organic Electronic Devices. *Polym. Chem.* **2013**, *4*, 484-494.

[6] Ashraf, R. S.; Kronemeijer, A. J.; James, D. I. ; Sirringhaus, H.; McCulloch, I. A New Thiophene Substituted Isoindigo Based Copolymer for High Performance Ambipolar Transistors. *Chem. Commun*. **2012**, *48*, 3939- 3941.

[7] Van Pruissen, Gijs W. P.; Gholamrezaie, F.; Wienk, M. M.; Janssen, R. A. J. Synthesis and Properties of Small Band Gap Thienoisoindigo Based Conjugated Polymers. *J. Mater. Chem.* **2012**, *22*, 20387-20393.

[8] Stalder, R.; Mei, J.; Graham, K. R.; Estrada, L. A.; Reynolds, J. R. *Chem. Mater*. **2014**, *26*, 664–678.

[9] Tomassetti, M.; Ouhib, F.; Wislez, A.; Duwez, A. -S.; Penxten, H.; Dierckx, W.; Cardinaletti, I.; Bovee, R. A. A.; van Pruissen, G. W. P.; Jérôme, C.; Manca, J.; Maes, W.; Detrembleur, C. *Polym. Chem.* **2015**, *6*, 6040–6049.

[10] Saeki, A.; Koizumi, Y.; Aida, T.; Seki, S. *Acc. Chem. Res.* **2012**, *45*, 1193-1202.

[11] Grozema, F. C.; Siebbeles, L. D. A. Charge Mobilities in Conjugated Polymers Measured by Pulse Radiolysis Time-Resolved Microwave Conductivity: From Single Chains to Solids. *J. Phys. Chem. Lett.* **2011**, *2*, 2951-2958.

[12] Saeki, A.; Tsuji, M.; Seki, S. *Adv. Energy Mater.* **2011**, *1*, 661-669.

[13] Saeki, A.; Yoshikawa, S.; Tsuji, M.; Koizumi, Y.; Ide, M.; Vijayakumar, C.; Seki, S. *J. Am. Chem. Soc.* **2012**, *134*, 19035-19042.

[14] Guo, J.; Ohkita, H.; Benten, H.; Ito, S. *J. Am. Chem. Soc.* **2009**, *131*, 16869–16880.

[15] Ide, M; Koizumi, Y.; Saeki, A.; Izumiya, Y.; Ohkita, H.; Ito, S.; Seki, S. *J. Phys. Chem. C* **2013**, *117*, 26859−26870.

[16] Yasutani, Y; Honsho, Y; Saeki, A; Seki, S, *Synthetic Metals*, **2012**, *162(17-18)*, 1713-1721.

[17] Cremer, L. D; Vandeleene, S; Maesen, M; Verbiest, T; Koeckelberghs, G. *Macromolecules* **2008**, *41*, 591–598.

[18] Scherf, U; List, E. J. W. *Adv. Mater*., **2002**, *14*, 477–487.

[19] Cheng, Y. –J.; Yang, S. –H.; Hsu, C.-S. *Chem. Rev.* **2009**, *109*, 5868–5923.

[20] Saeki, A.; Tsuji, M.; Seki, S. *Adv. Energy Mater.* **2011**, *1*, 661–669.

[21] Savenije, T. J; Grzegorczyk, W. J; Heeney, M; Tierney, S; McCulloch, I; Siebbeles, L, D, A; *J. Phys. Chem. C* **2010**, *114*, 15116–15120.

[22] Nelson. J.; Kwiatkowski. J. J.; Kirkpatrick. J.; Frost. J. M. *Acc. Chem. Res.* **2009**, *42*, 1768–1778.

[23] Kaake, L. G.; Jasieniak, J. J.; Bakus, II, R. C.; Welch, G. C.; Moses, D.; Bazan, G. C.; Heeger, A. J. *J. Am. Chem. Soc*. **2012**, *134*, 19828–19838.

[24] Ohkita, H.; Cook, S.; Astuti, Y.; Duffy, W.; Tierney, S.; Zhang, W.; Heeney, M.; McCulloch, I.; Nelson, J.; Bradley, D. D. C. *J. Am. Chem. Soc.* **2008**, *130*, 3030–3042.

[25] Gundlach, D. J.; Zhou, L.; Nichols, J. A.; Jackson, T. N.; Necliudov, P. V.; Shur, M. S. *J. Appl. Phys.* **2006**, *100*, 024509/1–13.

[26] Tsoi. W. C.; Spencer. S. J.; Yang. L.; Ballantyne. A. M.; Nicholson. P. G.; Turnbull. A.; Shard. A. G.; Murphy. C. E.; Bradley. D. D. C.; Nelson. J. *Macromolecules*, **2011**, *44*, 2944–2952.

[27] He, Z.; Zhong, C.; Huang, X.; Wong, W.-Y.; Wu, H.; Chen, L.; Su, S.; Cao, Y. *Adv. Mater.* **2011**, *23*, 4636–4643.

[28] Lee, J. K.; Ma, W. L.; Brabec, C. J.; Yuen, J.; Moon, J. S.; Kim, J. Y.; Lee, K.; Bazan, G. C.; Heeger, A. J. *J. Am. Chem. Soc.* **2008**, *130*, 3619–3623.

[29] Peet, J.; Kim, J. Y.; Coates, N. E.; Ma, W. L.; Moses, D.; Heeger, A. J.; Bazan, G. C. *Nature Mater.* **2007**, *6*, 497–500.

[30] Liang, Y.; Xu, Z.; Xia, J.; Tsai, S.-T.; Wu, Y.; Li, G.; Ray, C.; Yu, L. *Adv. Mater.* **2010**, *22*, E135-E138.
[31] He, Z.; Zhong, C.; Su, S.; Xu, M.; Wu, H.; Cao, Y. *Nat. Photo*. **2012**, *6*, 591–595.
[32] Kim, J. Y.; Kim, S. H.; Lee, H.-H.; Lee, K.; Ma, W.; Gong, X.; Heeger, A. J. *Adv. Mater.* **2006**, *18*, 572-576.
[33] Tsoi. W. C.; Spencer. S. J.; Yang. L.; Ballantyne. A. M.; Nicholson. P. G.; Turnbull. A.; Shard. A. G.; Murphy. C. E.; Bradley. D. D. C.; Nelson. J. *Macromolecules*, **2011**, *44*, 2944-2952.
[34] Mauer, R.; Howard, I. A.; Laquai, F. *J. Phys. Chem. Lett.* **2010**, *1*, 3500-3505.
[35] Dibb, G. F. A.; Kirchartz, T.; Credgington, D.; Durrant, J. R.; Nelson, J. *J. Phys. Chem. Lett.* **2011**, *2*, 2407-2411.
[36] Koster, L. J. A.; Kemerink, M.; Wienk, M. M.; Maturová, K.; Janssen, R. A. J. *Adv. Mater.* **2011**, *23*, 1670-1674.
[37] Hamadani, B.H.; Jung,S.; Haney, P.M.; Richter,L.J.; Zhitenev, N. B. *Nano Letters*, **2010**, *10*, 1611-1617.
[38] Lee, J. K.; Ma, W. L.; Brabec, C. J.; Yuen, J.; Moon, J. S.; Kim, J. Y.; Lee, K.; Bazan, G. C.; Heeger, A. J. *J. Am. Chem. Soc.* **2008**, *130*, 3619-3623.
[39] Yamamoto, S.; Ohkita, H.; Benten, H.; Ito, S. *J. Phys. Chem. C* **2012**, *116*, 14804-14810.
[40] Yamamoto, S.; Guo, J.; Ohkita, H.; Ito, S. *Adv. Funct. Mater.* **2008**, *18*, 2555-2562.
[41] Antonietta Loi, M.; Toffanin, S.; Muccini, M.; Forster, M.; Scherf, U.; Scharber, M. *Adv. Funct. Mater.* **2007**, *17*, 2111-2116.
[42] Veldman, D.; Ípek, Ö.; Meskers, S. C. J.; Sweelssen, J.; Koetse, M. M.; Veenstra, S. C.; Kroon, J. M.; van Bavel, S. S.; Loos, J.; Janssen, R. A. J. *J. Am. Chem. Soc.* **2008**, *130*, 7721-7735.
[43] Osaka, I.; Kakara, T.; Takemura, N.; Koganezawa, T.; Takimiya, K. *J. Am. Chem. Soc*. **2013**, *135*, 8834−8837.

Chapter 4: Molecular Engineering of Benzothienoisoindigo Copolymers: Control of Backbone Orientation

In this chapter, the author presents new strategies to improve the power conversion efficiency for organic photovoltaics by using new pigment, benzothienoisoindhigo (BTIDG) as the acceptor unit. In the previous chapter, TIDG copolymers demonstrated interesting properties as well as many issues to be overcome, for example, a low solubility, control of morphology, and the excessive near-infrared absorption due to the high planarity of five-membered ring backbone. Unsymmetric structure of BTIDG helps to realize a synthesis of a new copolymer to achieve a highe power conversion efficiency. A large π-core size of donor unit supports the face-on orientation of BTIDG copolymers, which make it possible to enhance the crystallinity and charge transport. The author also summarized the relationships between hole mobility and ratio of face-on orientation of BTIDG copolymers.

4-1. Introduction

In previous chapter, thienoisoindigo (TIDG) copolymers[1,2] showed properties to absorb in a broad range of wavelength including NIR region of solar spectrum and their edge of absorption reached 1400 nm which has small bandgap from 1.0 to 1.6 eV. However, TIDG resulted in excessively-narrow optical bandgap (E_g^{opt}, 1.0–1.1 eV) in conjugation with the benchmark donors (benzodithiophene and cychlopentadithiophene).[3] In the Chapter 3, the unsatisfactory PCE of 1.4 % was obtained as the best value in the blend of [6,6]-Phenyl-C_{61}-butyric acid methyl ester ($PC_{61}BM$) and fluorene-TIDG polymer (E_g^{opt} = 1.6 eV). In addition to their mismatches in energy alignment, the extremely short exciton lifetime induced the energy loss via bulk charge recombination, and unfavorable orientation/morphology partly associated with insufficient solubility.[4] Therefore, simultaneous control of these factors through molecular engineering or processing is a crucial prerequisite towards boosting PCE of TIDG-based polymer, however, this is a challenging theme shared by all disciplines.

One of the synthetic routes of TIDG unit is the dimerization of mono-keto and di-keto precursors in acetic acid, the former of which was prepared by reacting the di-keto precursor with hydrazine reagent followed by Wolff-Kishner type reduction. Inspired from this quantitative and heterotic dimerization scheme, the author attempted synthesis of half-TIDG and half-IDG unit from their relevant two precursors. This would bring moderate electron accepting nature with a good solubility as a result of its asymmetric half-distorted π-plane. In the course of the research, M. S. Chen *et al.*[5]

reported this benzothienoisoindigo (BTIDG)-based polymers synthesized by the almost similar route and demonstrated the large improvement of PCE (4.7%) in terthiophene-BTIDG copolymer. Notably, they realized selective manipulation of edge-on or face-on orientation of polymer by controlling the backbone planarity (IDG or BTIDG) suitable for field-effect transistor (FET) or OPV, respectively. However, the high-performing BTIDG copolymer still includes some portions of edge-on contribution, suggestive of an extra room for enhancing the portion of face-on orientated polymer crystallite where considerable improvement has been reported in both charge carrier transport and overall PCE of OPV devices.[6]

The author synthesized novel BTIDG-based copolymers in combination with benzodithiophene (BDT) as same as TIDG copolymers. Molecular weight improved by introducing the BTIDG acceptor with longer alkyl chain, thus it was possible to fabricate the OPV devices from chlorobenzene solution. However, the film morphology of BDT-BTIDG copolymers was not suitable to the charge transport in OPV devices thus power conversion efficiency (PCE) was similar to BDT-TIDG copolymer.[7] Based on this knowledge, BTIDG acceptor was coupled with benzobisthiazole (BBTz)[8,9] and thiazolothiazole (TzTz),[10,11] where BBTz and TzTz which are normally electron acceptors[12,13]. This molecular design is intended to provide both optimal E_g^{opt} (ideally 1.37–1.45 eV from the calculation)[14] and HOMO level.[15] Furthermore, the author exemplified the synergetic impact of alkylthiophene spacer on the control of polymer orientation and OPV output. These molecular designs of BTIDG copolymers could overcome the defects of TIDG copolymers in terms of solubility, molecular weight,

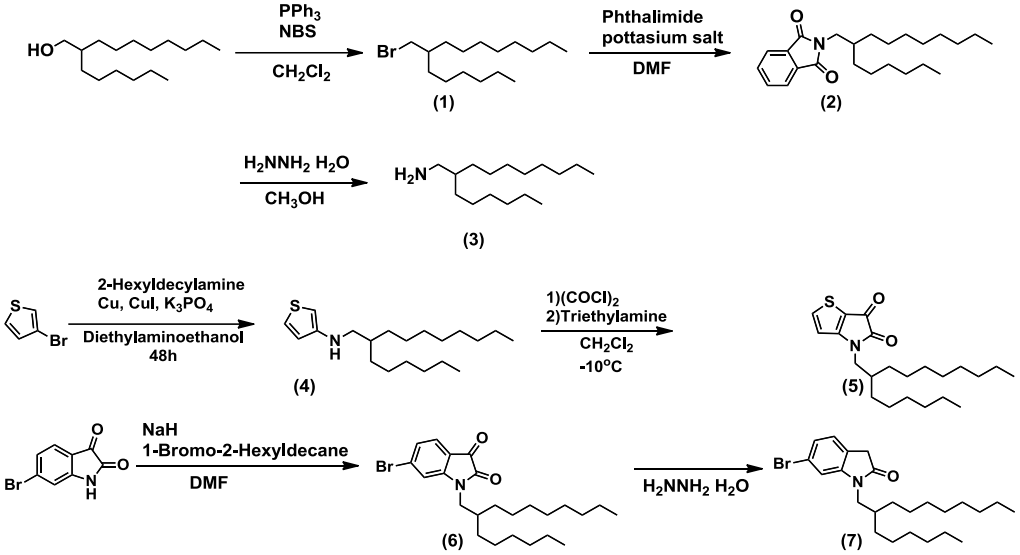

Scheme 5. Synthesis procedures of side chain and BTIDG monomer. Reproduced from ref 15 with permission from the Royal Society of Chemistry.

orientation and energy level tuning. BTIDG copolymers tend to form the face-on orientation even after blending with PCBM.

4-2. Synthesis procedure of benzothienoisoindigo copolymers

Synthesis procedures of BTIDG monomer, copolymers and donor moiety were summarized in Scheme 5 - Scheme 7.

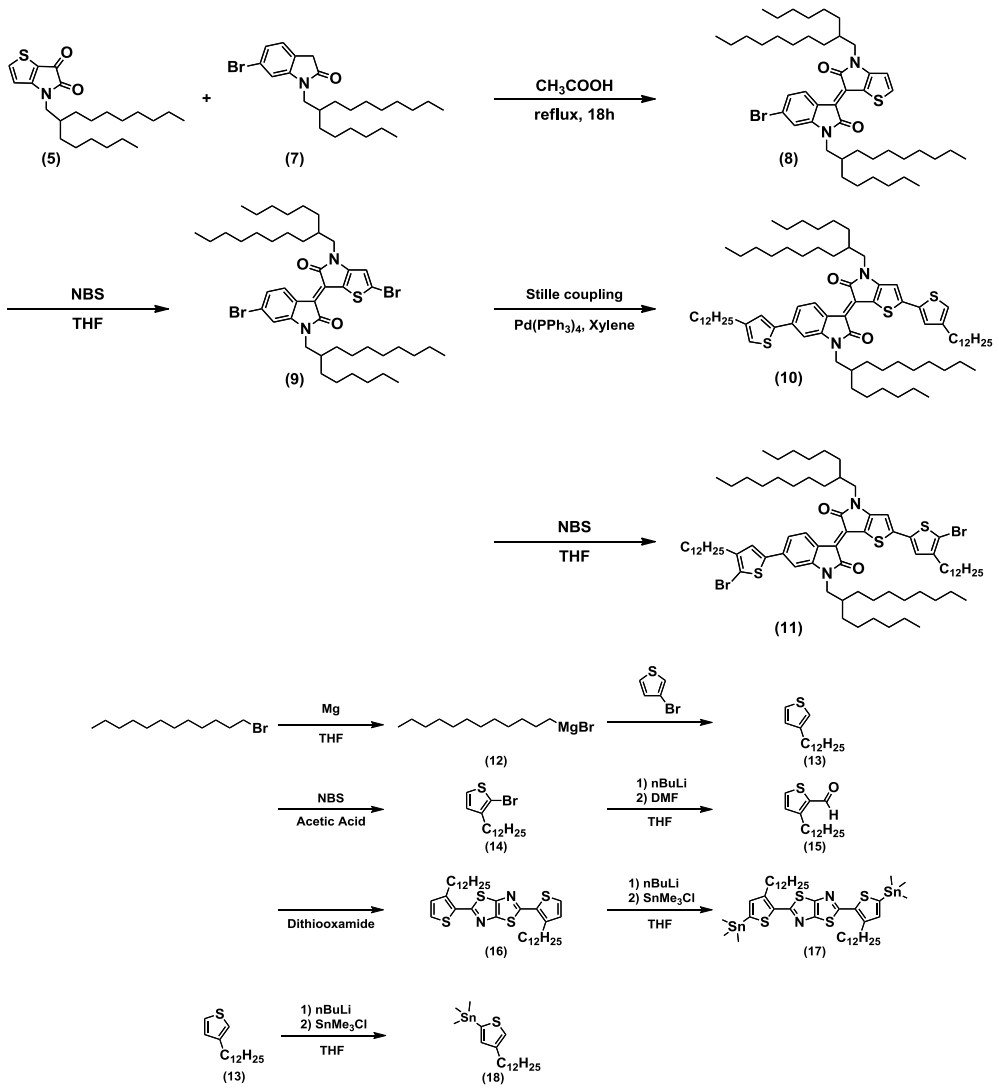

Scheme 6. Synthesis procedures of BTIDG monomer and donor. Reproduced from ref 15 with permission from the Royal Society of Chemistry.

4-3. Optical and electrochemical properties of BTIDG copolymers

The brominated BTIDG monomer **9** and alkylthiophene-BTIDG monomer **11** were synthesized according to the route of Scheme 1. Synthesis and characterization of

the compounds **1**-**8** including ^{1}H NMR and mass spectroscopy data are provided in Experimental section. The BTIDG-based copolymers were polymerized by Stille coupling reaction (Scheme 7).

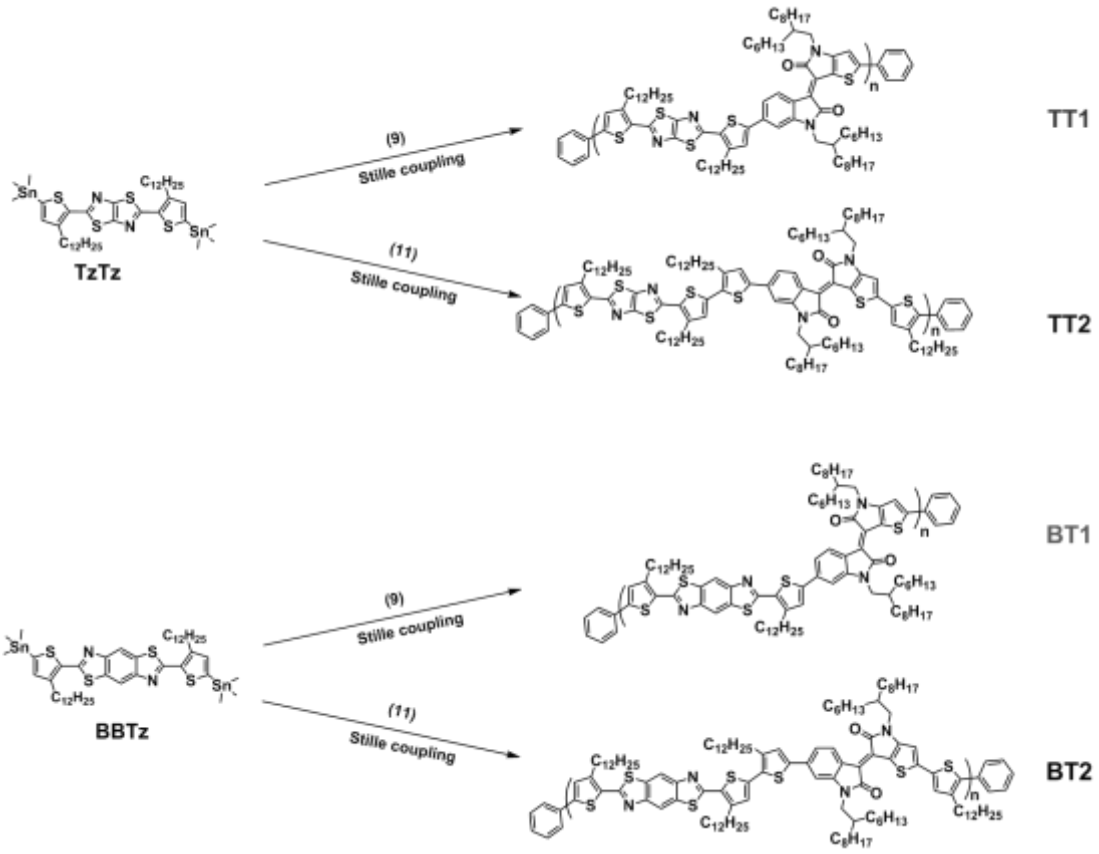

Scheme 7. Synthesis procedures of BTIDG copolymers. Reproduced from ref 15 with permission from the Royal Society of Chemistry.

The chemical structures of BTIDG-based copolymers were shown in Scheme 7: **TT1**, **TT2**, **BT1**, and **BT2**, in which the number (1 or 2) represents the length of alkylthiophene spacer (thiophene or bithiophene). Electronic absorption spectra of BTIDG polymers were measured in chloroform solution (Figure 39a) and thin film (Figure 39b). The BTIDG polymers indicate the absorption edges at ca. 820–880 nm corresponding to the E_g^{opt} of 1.41–1.52 eV (Table 8). These E_g^{opt} are finely tuned to the aforementioned ideal value for single cell OPV polymer,[16] which is a notable advantage over the previous near-infrared absorbing TIDG polymers. In addition, the weight-averaged molecular weights (M_w) of BTIDG polymers are as high as 127–231 kg mol^{-1} (Table 8) except for **TT1** (32 kg mol^{-1}), which is much higher than the previous TIDG polymers (15–87 kg mol^{-1}). This is because that the solubility was significantly

improved by virtue of the long linear alkyl chains of thiophene spacer and branched ones of asymmetric BTIDG.

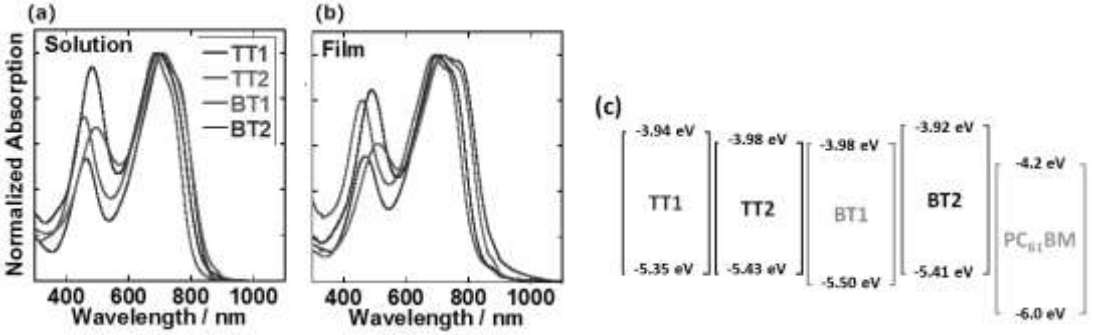

Figure 39. (a) Electronic absorption spectra of **TT1** (red line), **TT2** (blue line), **BT1** (green line) and **BT2** (black line) in chloroform solution at room temperature, respectively. (b) Electronic absorption spectra of **TT1**, **TT2**, **BT1** and **BT2** as films dropcast from chloroform solution. (c) HOMO and LUMO energy levels of **TT1**, **TT2**, **BT1**, **BT2**, and $PC_{61}BM$. Reproduced from ref 15 with permission from the Royal Society of Chemistry.

Table 8. Optical and Electrochemical Properties of BTIDG Polymers.

Polymer	M_w / kg mol^{-1} (PDI)	HOMO /eV [a]	LUMO /eV [b]	λ_{max} /nm[c]	E_g^{opt} / eV [d]
TT1	32 (1.7)	-5.35	-3.94	718	1.41
TT2	127 (3.5)	-5.43	-3.98	719	1.45
BT1	142 (2.1)	-5.50	-3.98	690	1.52
BT2	231 (3.9)	-5.41	-3.92	699	1.49

[a] Determined by PYS of drop-casted films. [b] HOMO + E_g^{opt}. [c] In film states. [d] Determined from onset of the electronic absorption spectra in film states. Reproduced from ref 15 with permission from the Royal Society of Chemistry.

Photoelectron yield spectroscopy (PYS, Figure 38) was performed to estimate the HOMO levels of polymer films, giving almost identical HOMO (-5.35– -5.50 eV) and slightly-varying the lowest unoccupied molecular orbital (LUMO, -3.92– -3.98 eV). (Figure 39c) These HOMOs are indeed much deeper than those of our previous TIDG polymers (HOMO: -4.7– -5.4 eV, LUMO: -3.8 eV), while the LUMO-LUMO offsets between polymer and PCBM (-4.2 eV)[17] became close to or even less than the empirically-required minimum value (0.3 eV).

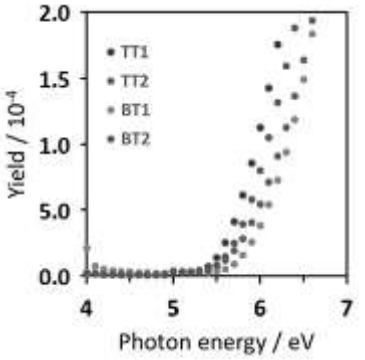

Figure 38. The results of PYS measurement for BTIDG copolymers. HOMO levels are evaluated as -5.5 eV for **BT1** and -5.4 eV for **TT1**, **TT2** and **BT2**. Reproduced from ref **15** with permission from the Royal Society of Chemistry.

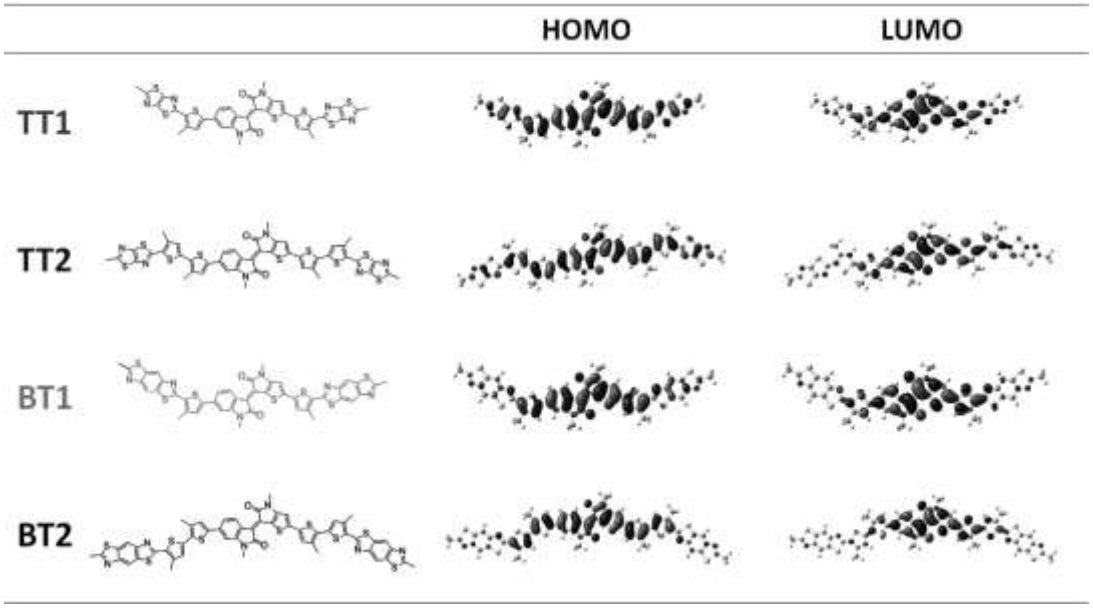

Figure 40. Molecular orbitals of BTIDG trimers optimized by DFT B3LYP/6-31G(d). The alkyl chains are replaced with methyl groups for simplicity. Reproduced from ref 15 with permission from the Royal Society of Chemistry.

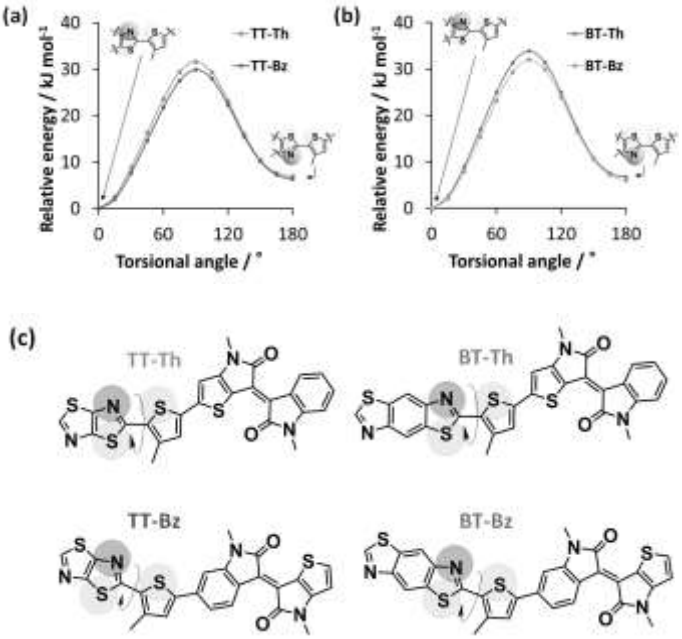

Figure 41. Torsional energy potential profiles of neutral states of (a) TzTz-BTIDG and (b) BBTz-BTIDG dimers. Two isomers for each dimer, benzene-side or thiophene-side coupling, were examined as illustrated in (c), because BTIDG moiety is asymmetric structure. However, the difference among the isomers was negligible. The molecular geometry were optimized by DFT calculation using B3LYP/6-31G* level. The alkyl chains were replaced by methyl group for simplicity. The donor unit (TT or BT) was rotated along the arrowed bond. Reproduced from ref 15 with permission from the Royal Society of Chemistry.

Electron withdrawing nature of BTIDG unit is clearly evident from the density functional theory (DFT) calculation shown in Figure 40. The LUMO is localized on the BTIDG unit, while the HOMO is spread over the polymer backbone of donor (BT or TT), spacer (thiophene), and BTIDG, similar to the TIDG and IDG[18] polymers. Thanks to the inherently high coplanarity and low LUMO, TIDG-thiophene and -naphthalene copolymers have uncovered ambipolar charge transport (μ_h = 0.18 $cm^2 V^{-1} s^{-1}$ and μ_e = 0.03 $cm^2 V^{-1} s^{-1}$)[19] and ultrahigh hole mobility up to 14 $cm^2 V^{-1} s^{-1}$,[20] respectively. In addition, nonbonding Coulomb interaction arisen from the difference in electronegativity of sulfur atom of spacer thiophene and nitrogen atom of TT and BT could facilitate coplanarity of π-conjugated polymer backbone. This is supported by DFT calculation exhibiting that the total energy of N…S conformation is 7 kJmol-1 lower than S…S conformation (Figure 41), consistent with chalcogen (S…O)[19] and N…S interactions[21] reported previously.

4-4. Polymer orientation measured by 2D-GIXRD

Polymer orientation in pristine and $PC_{61}BM$ blend films were characterized by two-dimensional grazing-incidence X-ray diffraction (2D-GIXRD) shown in Figure 42. Thin spun-coat pristine films (ca. 60 nm) contained intense tail of direct X-ray overlapping the weak diffraction of polymer in the out-of-plane low angle diffraction region. This hampers the quantitative analysis of face-on and edge-on orientation and thus the thick pristine films (ca. 1 μm) prepared by drop-casting were evaluated. It needs to be mentioned, though, that the π–π stacking distance and face-on/edge-on orientations were mostly unchanged between spun-coat and drop-cast films. The blend films were prepared in the same way with the optimal OPV devices fabrication (vide infra). Surprisingly, all of the pristine polymers indicate profound face-on orientation with negligibly small edge-on peaks. The π-π stacking distances are moderate, ranging from 3.57 Å for **BT1** to 3.67 Å for **TT2** (Table 9). Although the π-π stacking distances did not display obvious variations by the molecular structure, the lamellar packing distances were rationally increased from mono-thiophene spacer (24.8 Å for both **TT1** and **BT1**) to bis-thiophene one (26.1 Å for **TT2** and 25.4 Å **BT2**).

The ratio of face-on orientation ($R_{face\text{-}on}$ in %) was evaluated by $I_{ip}/(I_{ip}+I_{op})$, where I_{ip} and I_{op} are the peak intensities of (100) diffraction in the in-plane and out-of-plane directions, respectively. It should be noted that $R_{face\text{-}on}$ is an approximation of face-on fraction in XRD-active crystalline part,[22] and thus $R_{face\text{-}on}$ is not directly associated with crystallinity of polymer. Besides, out-of-plane diffraction tend to appear

with higher intensity than its actual composition, due to the combination of the thin film geometry and the constraint of one axis to the sample plane in polar figure.[23] By taking these into account, $R_{face\text{-}on}$ evaluation in this study is supposed to be slightly underestimated, since the out-of-plane diffraction at the small scattering vector attributed to edge-on orientation could be stronger than is the actual case. As listed in Table 9, pristine **BT2** shows a pronounced $R_{face\text{-}on}$ as high as 95% (the ratio of face-on to edge-on, I_{ip}/I_{op} is ca. 19). To the best of our knowledge, this is the top-class preferential

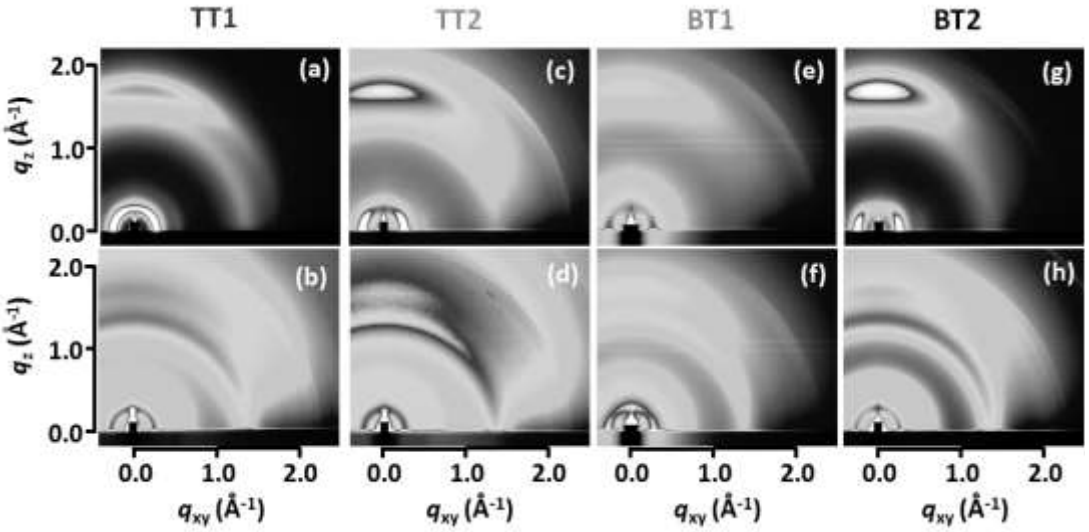

Figure 42. 2D-GIXRD patterns of pristine (a) **TT1**, (c) **TT2**, (e) **BT1** and (g) **BT2** drop-cast on ITO substrate. (b) (d) (f) (h) are the patterns of optimal OPV devices (polymer and $PC_{61}BM$ blends). Reproduced from ref 15 with permission from the Royal Society of Chemistry.

Table 9. 2D-GIXRD and SCLC data of BTIDG polymers.

Film (p/n ratio)	π-π/Å [a]	IL/Å [b]	$R_{face\text{-}on}$ [c]	μ_h /10^{-5} cm^2 V^{-1} s^{-1}
TT1	3.64	24.8	67%	1.0
TT1:$PC_{61}BM$ (1:1)	3.64	24.8	40%	6.8
TT2	3.67	26.1	80%	5.9
TT2:$PC_{61}BM$ (1:2)	3.71	26.1	73%	10
BT1	3.57	24.8	93%	0.18
BT1:$PC_{61}BM$ (1:2)	3.54	23.7	68%	4.9
BT2	3.66	25.4	95%	120
BT2:$PC_{61}BM$ (1:2)	3.64	24.8	75%	12

[a] Calculated from the (010) peaks in the out-of-plane direction. [b] Interlamellar distance calculated from the (100) peaks in the in-plane direction. [c] Calculated by $I_{ip}/(I_{ip}+I_{op})$. Reproduced from ref 15 with permission from the Royal Society of Chemistry.

face-on orientation reported so far in OPV polymers. Examples of high $R_{face\text{-}on}$ polymer are thiazolothiazole (91%) [24] and dicarboximide-dithiophene (PBTI3T, 93%, face-on:edge-on = 14)[25] polymers. We extracted the $R_{face\text{-}on}$ of 94% for pristine PTB7 from its 2D-GIXRD image,[26] corroborating the high face-on orientation of the successful polymer. Since the face-on orientation is advantageous for vertical charge transport in OPV cells,[6,11,25] recent development of high performance LBPs is directed to control of the polymer orientation as well as bandgap engineering. The second highest $R_{face\text{-}on}$ of 93% was found for **BT1**, which is followed by **TT2** (80%) and **TT1** (67%).

Due to the complicated factors affecting the polymer orientation, a rational molecular design of face-on polymer remains poorly understood. Solubility, shape of solubilizing alkyl chains (branched one is likely more favorable for face-on than linear one), and the length of alkyl chains have been supposed as the premiere factors that control polymer orientation. In the present study, the sizes of π-plane (BT >TT) and spacer (bithiophene:2 > thiophene:1) were found to have an impact on improving face-on orientation. In sharp contrast, mixing with $PC_{61}BM$ significantly decreased the face-on orientation. The similar trend appeared in all blend films, where $R_{face\text{-}on}$ dropped by 10–20 % (Table 9). For instance, the most face-on-preferred **BT2** indicate the $R_{face\text{-}on}$ of 75% in the PCBM blend, accompanying with a decrease of diffraction intensity.

4-5. Hole mobility measured by SCLC

Hole mobilities (μ_h) of BTIDG polymers and their blends with $PC_{61}BM$ were measured by space-charge limited current (SCLC) technique[27] (Table 9 and Figure 43.). Remarkably, the most face-on-orientated pristine **BT2** demonstrated the highest μ_h of 1.2×10^{-3} cm^2 V^{-1} s^{-1}, while the other polymers gave 2–3 orders of magnitude smaller values (10^{-5}–10^{-6} cm^2 V^{-1} s^{-1}). **BT2**:$PC_{61}BM$ blend film showed the μ_h of 1.2×10^{-4} cm^2 V^{-1} s^{-1} decreased by one order of magnitude; however, this is still higher than the other polymer blends (10^{-4}–10^{-5} cm^2 V^{-1} s^{-1}). Despite the reduced diffraction intensities upon mixing with $PC_{61}BM$, the π-π stacking and

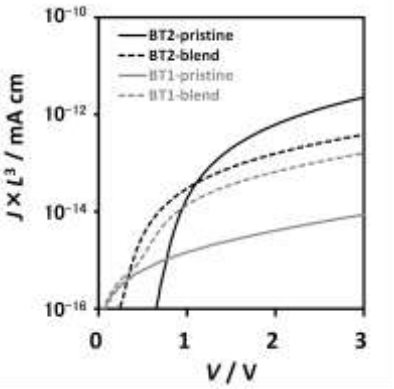

Figure 43. *J-V* curves of hole only devices measured by SCLC for pristine and blend films of **BT1** (dotted) and **BT2** (solid). Reproduced from ref 15 with permission from the Royal Society of Chemistry.

lamellar packing distances were mostly unchanged, indicative of no intercalation into the polymer crystallites. Interestingly, μ_h of $PC_{61}BM$-blended **TT1**, **TT2**, and **BT1** are comparable to or even higher than those of pristine polymers, regardless of the deceased $R_{face\text{-}on}$. Although the cause of the enhanced μ_h in the blend films is unclear, this might merit the OPV performance which prefers a high μ_h in the vertical direction.

4-6. Evaluation of p/n blend ratio and thermal annealing effect by TRMC measurement

The TRMC measurements could provide the photovoltaic performance of an organic semiconductor effectively without fabricating a device. A white light pulse from a Xe-flash lamp induces photoconductivity transient, the maximum of which ($\Delta\sigma_{max}$) includes the information about charge carrier lifetime, local charge carrier mobility, and charge carrier density.[28] In Xe-flash TRMC measurement shown in Figure 44, the blend ratio of the BTIDG copolymers and $PC_{61}BM$ were screened thus the blending film demonstrated almost ten times higher photoconductivity than pristine copolymers. All of BTIDG copolymers showed downward tendency by thermal annealing of films processed from chlorobenzene solution with 1,8-diiodeoctane (DIO) additive. The p/n blend ratio at around 1/3 demonstrates highest photoconductivity, thus resulting highest PCE in OPV devices. (see section 4-7) **BT2**:$PC_{61}BM$ blend film showed the highest photoconductivity 1.8×10^{-8} S/cm and dropped to 3.5×10^{-9} S/cm after thermal annealing at 160 ^{o}C for 10 minutes. In addition, the inclination of TRMC photoconductivity indicates that the thermal annealing of films drop-casted from chlorobenzene solution without DIO is a drawback of OPV devices.

On the other hand, the results of TRMC photoconductivity with DIO (Figure 45) revealed opposite trend in **BT2** for thermal annealing, that the $\Delta\sigma_{max}$ increased by thermal annealing. For example, **TT2** and **BT2** illustrated the increment tendency from neat film to thermal annealed film at 160 ^{o}C. These significant increment suggest that the additive performs better by thermal annealing in blend film. Interestingly, although **BT2** demonstrated higher photoconductivity by rising the annealing temperature, **TT2** increased its photoconductivity after annealing at 120 ^{o}C, but again it decreased its photoconductivity after thermal annealing at 160 ^{o}C as same as **BT2**. This trend is completely opposite to **BT1** which include a thiophene spacer, thus it suggests that number of thiophene spacer to control not only the orientation but also the morphology might be crucial factor to improve the PCE in OPV devices.

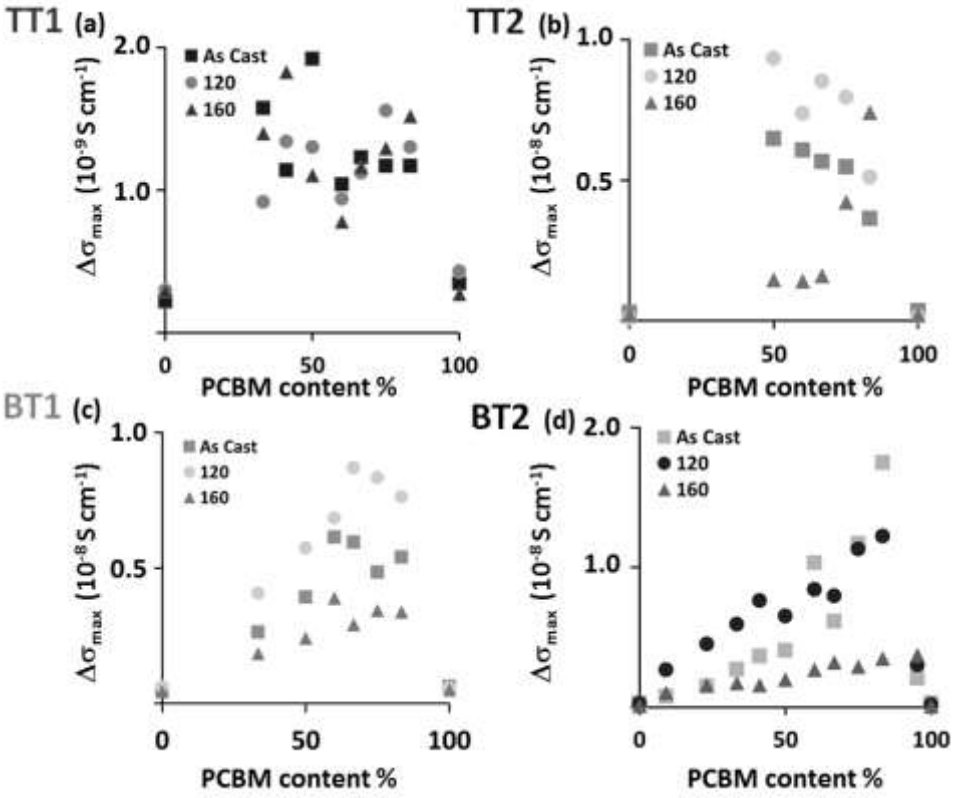

Figure 44. TRMC results of (a) **TT1**, (b) **TT2**, (c) **BT1**, and (d) **BT2** with $PC_{61}BM$ blend films drop-casted from chlorobenzene solutions without DIO (square). The thermal annealing was proceeded at 120 ^{o}C (circle), and 160 ^{o}C (triangle) respectively.

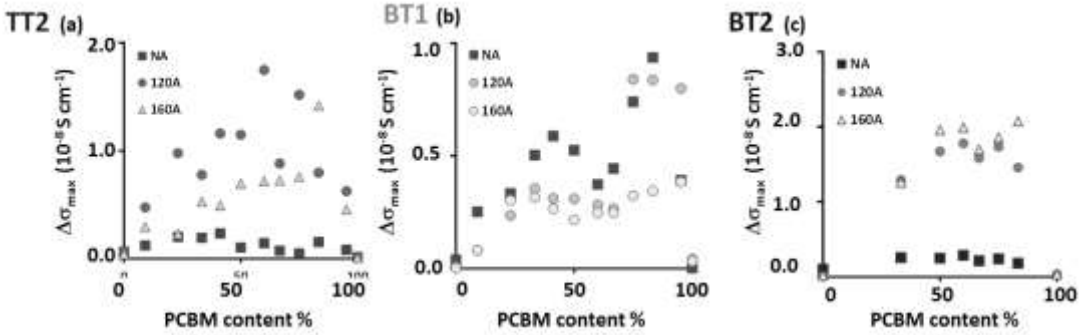

Figure 45. TRMC results of (a) **TT2**, (b) **BT1** and (c) **BT2** with $PC_{61}BM$ blend films drop-casted from chlorobenzene solutions with DIO (square). $\Delta\sigma_{max}$ of Xe-flash TRMC using microsecond white light pulse are shown. The thermal annealing was proceeded at 120 ^{o}C (circle), and 160 ^{o}C (triangle) respectively.

Laser-flash TRMC experiments shows p/n blend ratio dependence of the product of photoconductivity maxima ($\Delta\sigma_{max}$) and half-lifetime ($\tau_{1/2}$) obtained upon exposure to 355 and 500 nm nanosecond laser pulses. Benefitting from probing vibrational motion of charge carrier by gigahertz electromagnetic wave, TRMC measurement provides a direct observation of local charge-carrier transport property in the materials.[4] Accordingly **BT2** demonstrated as similar trend as WL-TRMC (Figure 46) thus the thermal annealing of devices without DIO could improves the OPV performance.

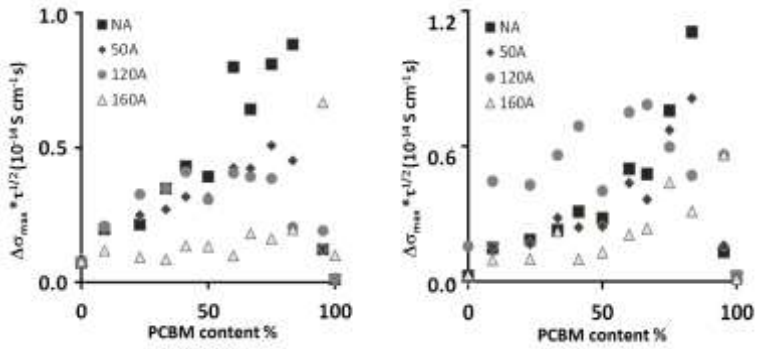

Figure 46. TRMC results of **BT2**:$PC_{61}BM$ blend films prepared by dropcasting CB solutions without DIO additive. $\Delta\sigma_{max} \times \tau_{1/2}$ of laser-flash TRMC using (a) 355 and (b) 500 nm nanosecond laser as an excitation are plotted as a function of $PC_{61}BM$ content. 100 wt % $PC_{61}BM$ represents the pure $PC_{61}BM$.

4-7. OPV performance of BTIDG copolymers

Figure 47 shows the highest performing current-voltage curves of BTIDG copolymers and PCBM blend films in normal cell structure (PEDOT:PSS/active layer/Ca/Al). The active layers were prepared from chlorobenzene (CB) solution with 3 vol% solvent additive of either 1,8-diiodeoctane (DIO) or 1-chloronaphthalene (CN). We have examined the p/n blend ratio (1:1~1:5), film thickness, and thermal annealing effect (80, 120, and 150 ˚C). The optimal device parameters are summarized in Table 10, where the best blend ratio depends on the polymer (from 1:1 to 1:3) and no thermal annealing is preferred for all the polymers. Except for the low PCE of **TT1** (0.60%), **TT2**, **BT1**, and **BT2** indicated the comparable PCEs from 3.3 to 3.7%. The best PCE of 3.74% (average 3.47%) was achieved for **BT2**:$PC_{61}BM$ = 1:2 with the open-circuit voltage (V_{oc}) of 0.62 V, J_{sc} of 10.07 mA cm^{-2}, and fill factor (FF) of 0.66. The external quantum efficiency (EQE) spectra of **TT2**, **BT1**, and **BT2** shown in Figure 47b present

almost identical features corresponding to the superposition of polymer and $PC_{61}BM$ absorption spectra. The calculated J_{sc} (= J_{sc}^{calc}) from the EQE spectra are in excellent agreement with J_{sc} under 1 sun (Table 10), indicative of the appropriate evaluation. The lowest- performing **TT1** shows a suppressed EQE spectrum and low J_{sc}, arisen from the lowest face-on orientation ($R_{face\text{-}on}$ = 40%) and molecular weight.

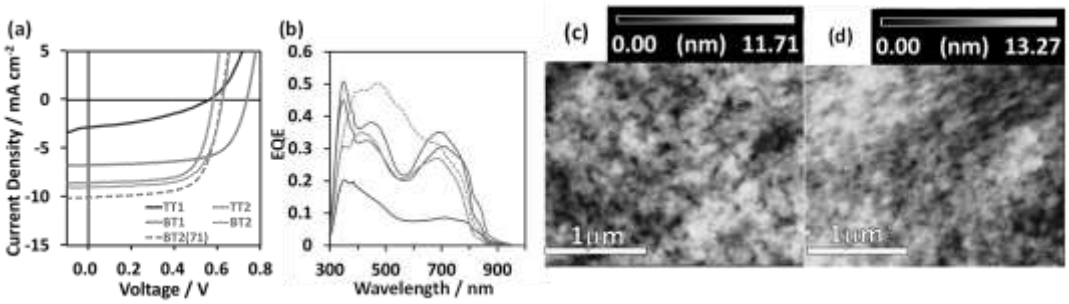

Figure 47. (a) *J-V* curves and (b) EQE spectra of the best-performing OPV devices. AFM topology images (2 × 2 μm) of (c) **BT2**:$PC_{61}BM$ = 1:2 and (d) **BT2**:$PC_{71}BM$ = 1:2. The scale bar at the bottom is 1 μm. Reproduced from ref 15 with permission from the Royal Society of Chemistry.

The film morphologies observed by atomic force microscopy (AFM) are almost similar (Figure 47c, d and Figure 48) and BTIDG copolymers does not demonstrate the specific aggregation observed in TIDG copolymers. V_{oc} are presumably proportional to the energy difference between HOMO of p-type polymer and LUMO of n-type fullerene with the energy loss ranging from 0.8 to 1.3 eV.[41] The highest V_{oc} of 0.73 V was obtained for **BT1** (HOMO = -5.50 eV), while those of other polymers having the almost same HOMO of -5.35– -5.43 eV were ca. 0.56–0.62 V, consistent with 0.1 V lower HOMOs.

Table 10. Organic photovoltaic performance of the polymer solar cells fabricated by ITO/ PEDOT:PSS/ Polymers:PCBM/Ca/Al devices. The active layer was spun-coat from a chlorobenzene/ DIO(3 v/v%) solution.

Blend	p/n ratio	*L* / nm	PCE (average) /%	V_{oc} / V	J_{sc} / mA cm^{-2}	FF
TT1:$PC_{61}BM$	1:1	79	0.60 (0.48)	0.56	2.83	0.38
TT2:$PC_{61}BM$	1:2	150	3.40 (3.22)	0.58	8.54	0.69
BT1:$PC_{61}BM$	1:3	84	3.29 (3.21)	0.73	6.72	0.67
BT2:$PC_{61}BM$	1:2	89	3.74 (3.47)	0.62	9.01	0.66
BT2:$PC_{71}BM$	1:2	90	4.18 (3.92)	0.62	10.07	0.67

Reproduced from ref 15 with permission from the Royal Society of Chemistry.

To improve the PCE of the best-performing **BT2**-based OPV, $PC_{61}BM$ was replaced by $PC_{71}BM$ which has higher absorption in the visible region than the former. As a result, **BT2**:$PC_{71}BM$ boosted the PCE to 4.18% (average 3.92%), due to the increased J_{sc} of 10.1 mA cm^{-2} without sacrifices of V_{oc} (0.62 V) and FF (0.67). The film morphologies of **BT2**:$PC_{61}BM$ and **BT2**:$PC_{71}BM$ were almost identical as visualized in the AFM images of Figure 47c and Figure 47d. We also examined a thicker film of **BT2**:$PC_{61}BM$, because the updating high PCE of 9–10% was achieved for the thick active layers (ca. 300 nm) composed of crystalline polymer.[6,29,30] The PCE of 300 nm-thick **BT2**:$PC_{61}BM$ was 3.51%, being equal to the 120 nm-thick film (3.50%). Despite the identical V_{oc} (0.61 V), the J_{sc} and FF of the 300 nm-thick film were increased to 13.38 mA cm^{-2} and decreased to 0.43, respectively, indicative of the typical trade-off relationship.[11] On the manufacturing stage of OPV via high-throughput inkjet printing, a polymer without strong thickness dependence is highly favorable[31] in which **BT2** could be relevant to this criterion.

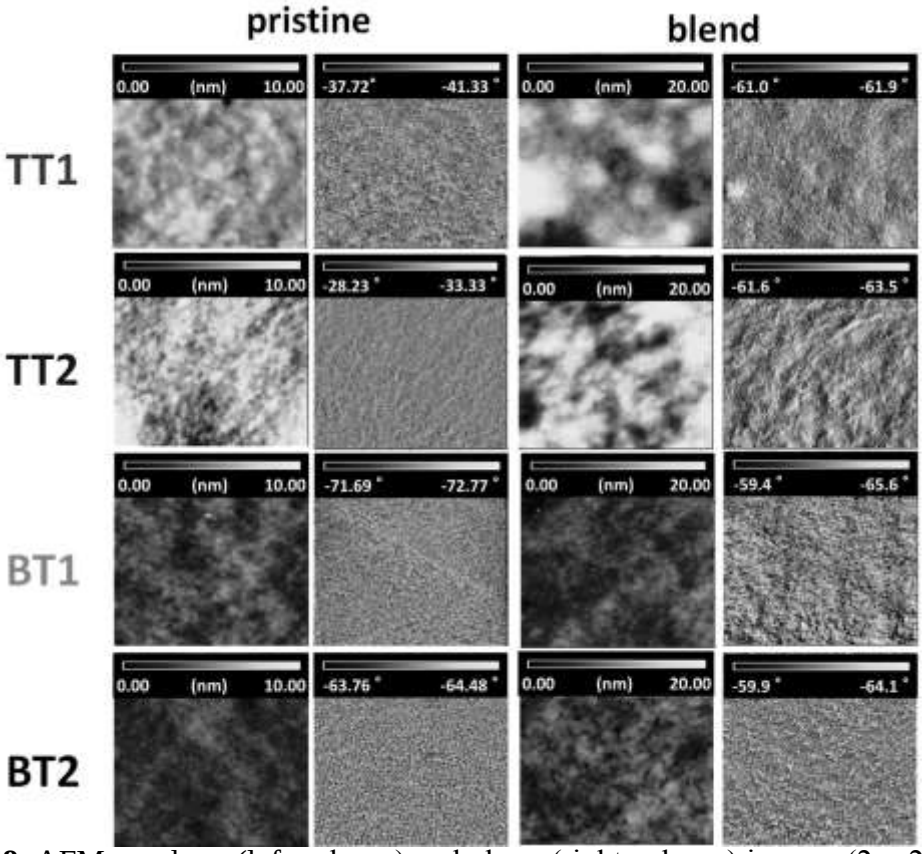

Figure 48. AFM topology (left column) and phase (right column) images (2 × 2 μm) of pristine films of BTIDG polymers and blend films with $PC_{61}BM$ as photovoltaic devices. No thermal annealing proceeded and devices were fabricated with 3 % DIO additives. Reproduced from ref 15 with permission from the Royal Society of Chemistry.

4-8. Evaluation of BDT-BTIDG copolymer : Comparison with TIDG copolymer

4-8-1. Introduction

Unsymmetricity of BTIDG moiety is attractive to improve the PCE of OPV composed of BTIDG copolymers in terms of solubility, because of their molecular structure has slight torsion in phenyl part of BTIDG. This design strategy provides optimal bandgap and HOMO level, concomitant with the highly planar structure facilitated by S…O interaction.[19] The author examined the improvement of coarse morphology of BDT-BTIDG:$PC_{61}BM$ films by appropriate selection of solvent and additive, thus compared the electronic properties to the BDT-TIDG copolymer (**P1**) in order to investigate the effect of unsymmetricity.

4-8-2. Optical and electronic properties of BDT-BTIDG

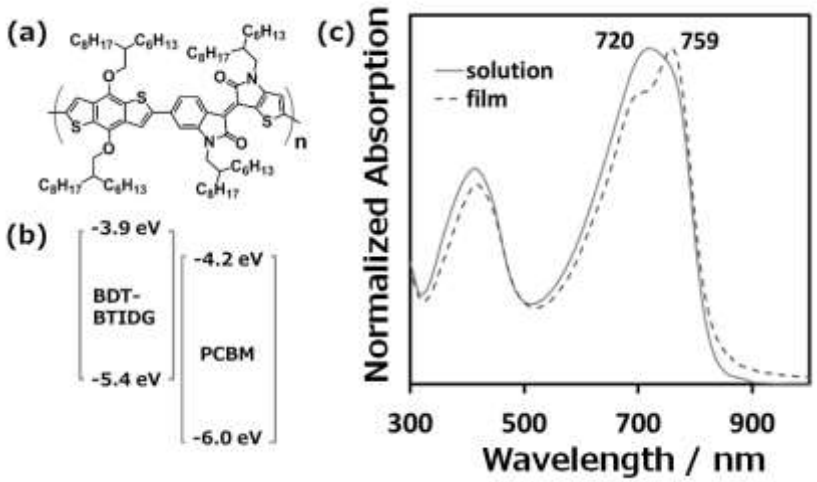

Figure 49. (a) Chemical structure of BDT-BTIDG copolymer. (b) Energy diagram of BDT-BTIDG and PCBM. (c) Normalized absorption spectra of BDT-BTIDG in chloroform solution (solid line) and film (dotted line). Copyright 2016 The Society of Photopolymer Science and Technology. (ref 7)

BDT-BTIDG was synthesized by following the previous procedures (Figure 49a, yield: 42%). The weight and number-averaged molecular weights were 9.2×10^4 and 3.6×10^4 g mol^{-1}, respectively. Optical and electrochemical properties of BDT-BTIDG were evaluated by UV-vis absorption spectroscopy and PYS (Figure 49b and c), giving the HOMO of -5.4 eV and the optical bandgap of 1.5 eV (835 nm absorption onset). Absorption in the near-infrared region is blue-shifted compared to the TIDG analogue[3], because of the weak electron-accepting and unsymmetrical BTIDG[15]. This observation is in line with the previous results on BTIDG copolymers employing benzobisthiazole as a weak donor.[15] The absorption maximum in the film state is

red-shifted by ca. 40 nm from that in solution with the appearance of vibronic peak. This is contrary to the TIDG copolymer,[3] and explained by moderated intramolecular charge transfer interaction between donor and BTIDG units and extension of π-conjugation.

Computer calculation by density functional theory (DFT) using B3LYP/6-31G* level was performed on a model trimer (Figure 50). The HOMO is distributed over the entire trimer backbone, while the lowest unoccupied molecular orbital (LUMO) is localized on the BTIDG unit. TIDG oligomer demonstrates the higher planarity than IDG oligomer,[3] because of the reduced steric hindrance between hydrogen atom on phenyl ring and oxygen atom on ketone group. As a consequence, BTIDG unit indicates the middle planarity between TIDG and IDG.

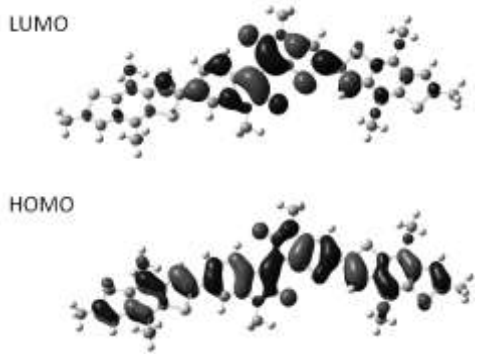

Figure 50. Optimized geometry and HOMO/LUMO distributions calculated by DFT 6-31G*. For simplicity, the alkyl chains were replaced by methyl. Copyright 2016 The Society of Photopolymer Science and Technology. (ref 7)

4-8-3. OPV performance of BDT-BTIDG:PCBM

According to the electrochemical measurement and DFT calculation, BTIDG moiety works as the weaker acceptor than TIDG unit, and thereby, BDT-BTIDG is likely to show higher open circuit voltage (V_{oc}) than TIDG copolymer (HOMO: -4.9 eV). BDT-BTIDG is dissolved in common halogenated solvents. We fabricated OPV devices of BDT-BTIDG:PCBM = 1:2 blend from CF or CB solution. As listed in Table 11, OPV devices prepared from CB solution show only 0.57 % PCE with V_{oc} = 0.75 V, short circuit current density (J_{sc}) = 1.17 mAcm^{-2}, and fill factor (FF) = 0.65, which is

Table 11. OPV performances of BDT-BTIDG:PCBM.

p/n	Solvent	Anneal	PCE (%)	V_{oc} (V)	J_{sc} (mA cm^{-2})	FF
1:2	CB	-	0.57	0.75	1.17	0.65
1:2	CB	120 °C	0.44	0.76	1.15	0.50
1:2	CB*	-	0.62	0.79	1.49	0.53
1:2	CF	-	0.45	0.77	1.10	0.53
1:2	**CF***	**-**	**0.83**	**0.77**	**2.22**	**0.49**

*DIO concentration was 3 vol %. Copyright 2016 The Society of Photopolymer Science and Technology. (ref 7)

lower than the previous TIDG analogue (0.87 %, V_{oc} = 0.40 V, J_{sc} = 4.75 mAcm^{-2}, FF = 0.46).[4]

Atomic force microscopy (AFM) visualizes the large phase separation over 200 nm with sea-island structures (Figure 51a), which causes yellow-greenish structural color at specific reflection angle. Such a large phase separation is sometimes observed in non-optimized OPVs, while a pronounced one with distinct structural color is a rarity.

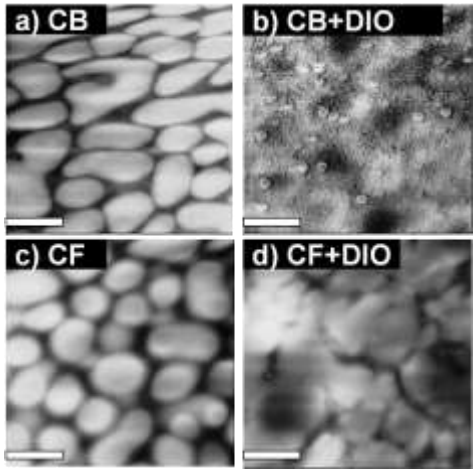

Figure 51. AFM height images (2 × 2 μm) of BDT-BTIDG:PCBM = 1:2 spun-coat from (a) CB, (b) CB + 3 vol% DIO, (c) CF, and (d) CF + 3 vol% DIO. The scale bar indicates 500 nm. Copyright 2016 The Society of Photopolymer Science and Technology. (ref 7)

Addition of 1,8-diiodeoctane (DIO) in CB solution was attempted to improve morphology. As a result, distinct boundary and coarse phase separation disappeared with the slightly improved PCE of 0.64 % (Figure 51b). In order to promote further mixing, a low-concentrated CF solution was examined, since the evaporation speed is faster than CB. Although BDT-BTIDG:PCBM film spun-coat from CF solution without DIO still formed the similar phase separation (Figure 51c), the CF with DIO solution led to the better surface morphology (Figure 51d). Consequently, the PCE was enhanced to 0.83 % with V_{oc} = 0.77 V, J_{sc} = 2.22 mAcm^{-2}, and FF = 0.49. The V_{oc} is higher than the

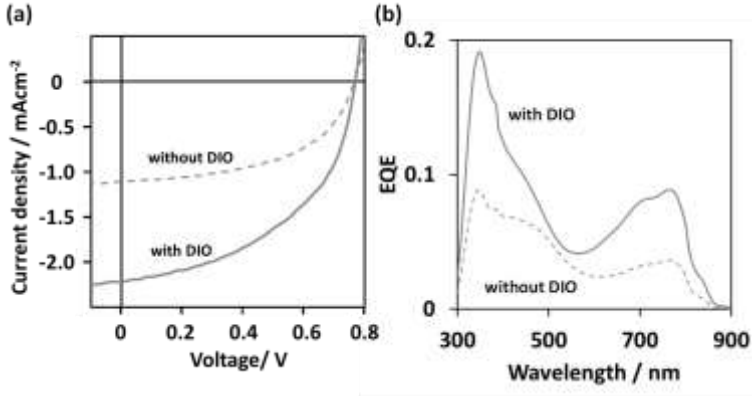

Figure 52. (a) *J*-*V* curves and (b) EQE spectra of the OPV devices spin-coated from CF solution with or without DIO. Copyright 2016 The Society of Photopolymer Science and Technology. (ref 7)

BDT-TIDG copolymer (0.40 V), consistent with the deeper HOMO level of BDT-BTDIG, but still lower than an ideal value expected from the energetics.[19]

The J_{sc} was increased by two-fold from 1.10 to 2.22 mAcm^{-2} upon addition of DIO (Figure 52a). This corresponds to the increase in the whole external quantum efficiency (EQE) spectra as shown in Figure 52b. The EQEs are roughly identical to the shape of photoabsorption spectra. Therefore, the lifetime of single exciton is unlikely a limiting factor of low J_{sc}, in contrast to the situation that near-infrared absorbing TIDG copolymer indicate significant suppression of EQE at the polymer-absorbing region.[4]

Although DIO facilitated intermixing of polymer and PCBM on the sub-hundred nanometer scale, J_{sc} was still the half of BDT-TIDG (J_{sc} = 4.75 mAcm^{-2}). Hence, the lowering of J_{sc} is probably caused by the incomplete formation of bulk heterojunction, which has not been fully optimized by just changing solvent and additive. In addition, FF of 0.49 is unsatisfactory, even though this is slightly higher than the analogous copolymers, BDT-TIDG (0.46)[4] and BDT-IDG (0.37). [32] Interestingly, the OPV device showing sea-island morphology (Figure 51a) yields a good FF of 0.65. The similar morphology, but having indistinct boundaries, resulted in the decreased FF of 0.53 (Figure 51c). Therefore, the mixed domain of polymer and PCBM is presumed to accelerate charge recombination.

4-8-4. Morphology engineering by selection of solvent

Polymer orientation and crystallite structures were characterized by 2D-GIXRD. Although the intensity of diffraction peak is not so strong due to its amorphous nature, the pristine BDT-BTIDG film exhibits face-on orientation with the π–π distance ($d_{\pi-\pi}$) of 3.85 Å and interlamellar distance (d_{IL}) of 22.1 Å (Figure 53a). The polymer:PCBM blend film under the device-optimized condition was changed to almost random orientation and rather amorphous pattern (Figure 53b). The previous BDT-TIDG copolymer showed obvious face-on orientation in the pristine film ($d_{\pi-\pi}$=3.65 Å and d_{IL}=17.0 Å), but was also turned to random orientation after blending with PCBM.[4] The expanded d_{IL} of BDT-BTIDG compared to BDT-TIDG is readily

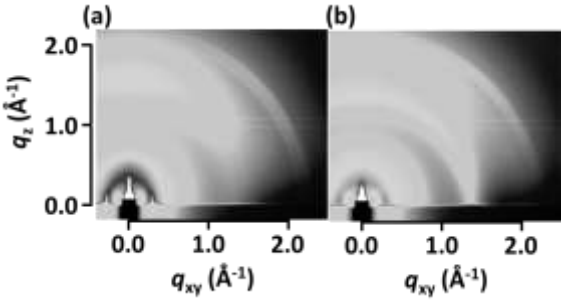

Figure 53. 2D-GIXRD images of (a) the pristine polymer and (b) PCBM blend films of the OPV device-optimized condition. Copyright 2016 The Society of Photopolymer Science and Technology. (ref 7)

understood by the longer side alkyl chain (hexyldecanyl) than the latter (ethylhexyl). BTIDG itself is able to keep a short $d_{\pi-\pi}$ (3.56−3.66 Å), if it is coupled with appropriate donor unit such as benzobisthiazole[15] and oligothiophene.[26] However, the use of BDT as the donor could not maintain the strong π–π stacking. Thereby, in addition to optimization of alkyl chain length, introducing spacer between BDT and BTIDG is expected as alternative approach to improve morphology and orientation.[33]

4-9. Conclusion

In conclusion, the author designed and synthesized new LBPs composed of asymmetric BTIDG acceptor and weak donors, affording suitable E_g^{opt} and HOMO levels. The 2D-GIXRD measurements revealed that the polymer orientation is molecularly controlled by the size of the donor p-plane and the number of alkylthiophene spacers, among which the top-class face-on orientation ($R_{face\text{-}on}$ = 95%) was demonstrated in pristine **BT2**. The best PCE of 4.2% was achieved in **BT2**:$PC_{71}BM$ without significant thickness dependence. Since the polymer : $PC_{71}BM$ films still suffer from a large decrease in face-on orientation by 10–20%, BTIDG-based polymers underpin further evolution of efficient OPV devices in which our work provides a useful design guide on polymer face-on orientation.

In the section 4-8, the author synthesized the new conjugated copolymer composed of BDT and unsymmetrical BTIDG unit in order to compare the influence of unsymmetricity. BDT-BTIDG copolymer exhibited the good solubility along with moderate electrochemical property (bandgap of 1.5 eV and HOMO level of -5.4 eV). However, a large phase separation unsuitable for OPV was found for the films processed from CB or CF solution. Solvent additive (DIO) improved the coarse morphology, but the maximized PCE was compelled to lie in the low level of 0.83%. Thiophene spacer between donor and acceptor and/or side chain engineering might lead to the formation of better bulk heterojunction. The emphasis of BDT-BTIDG copolymer is that solubility is possible to increase by the unsymmetricity and side chain length, but the further molecular engineering strategies are necessary to achieve the ideal morphology for OPV.

4-10. Experimental

General measurements. Weight and number-averaged molecular weights for the three polymers were measured by gel permeation chromatography (GPC) using tetrahydrofuran eluent and polystyrene standard. Photoelectron yield spectroscopy (PYS) measurements of polymer films on an ITO glass were performed by a Sumitomo Heavy Industry Co. PCR-202. Atomic force microscopy (AFM) was performed by a Seiko Instruments Inc. model Nanocute OP and Nanonavi II. The 2-dimensional grazing-incidence X-ray diffraction (2D-GIXRD) experiments were conducted at the SPring-8 (Japan Synchrotron Radiation Research Institute, JASRI) on the beam line BL19B2 using 12.39 keV (λ = 1 Å) X-ray..

OPV device fabrication. OPV devices were fabricated according to the previous report.[16)] The device configuration was ITO/PEDOT:PSS (45-60 nm)/active layer (ca. 100 nm)/Ca (10 nm)/Al (80 nm) with an active area of 7.1 mm^2. PCBM was purchased from Frontier Carbon Inc. and used as received. Current density-voltage (*J*-*V*) curves were measured using a source-meter unit (ADCMT Corp., 6241A) under AM 1.5 G solar illumination at 100 mW cm^{-2} (1 sun, monitored by a calibrated standard cell, Bunko Keiki SM-250KD) using a 300 W solar simulator (SAN-EI Corp., XES-301S).

Compound (1), (2) and (3) in Scheme 5 were synthesized according to the previous report.[34] Synthesis procedures of other compounds are described in reference 15.

General procedure of synthesis of the copolymers. The synthetic route for copolymers (**TT1**, **TT2**, **BT1**, and **BT2**) is shown in Scheme 7. The specific condition of each copolymer is given in Electronic Supplementary Information. Polymerization steps for BTIDG polymers were carried out through the palladium(0)-catalyzed Stille cross-coupling reactions. For Stille cross-coupling reaction, 1 equiv. of dibromo monomers and 1 equiv. of bistrimethylstannyl monomers were added into anhydrous xylene in a 20 mL Schlenk flask. Tetrakis- (triphenylphosphine)palladium(0) (0.05 eqiv.) was transferred into the mixture in a nitrogen atmosphere. The reaction mixture was stirred at 150 ˚C for 1-2 h, and then an excess amount of bromobenzene and trimethyltin benzene were added to end-cap the trimethylstannyl and bromo groups for 30 min, respectively. After adding a four-fold larger amount of xylene than the reaction solution, the reaction mixture was cooled to 40 ˚C and added slowly into a vigorously stirred ten-fold larger volume of methanol than the diluted reaction mixture. The polymers were collected by filtration and dried under vacuum. The dried crude polymers were dissolved in $CHCl_3$ (200 mL) and further purified by column

chromatography on neutral silica gel and six layered interleave NH silica with a NH_2 silica gel layer to remove the metallic impurities. The obtained $CHCl_3$ solution was filtered through celite and the solvent was removed under vacuum. The remaining solid was dissolved in a minimum amount of $CHCl_3$ and reprecipitated by six-fold larger amount of acetone than dissolved solution to remove oligomers. The precipitate was filtered using a membrane filter and dried under vacuum.

Polymerization of TT1, TT2, BT1, BT2.

Synthesis of copolymer TT1. Following the general polymerization procedure, bis[5-(trimethylstannyl)-3-undecylthiophen-2-yl]-[1,3]thiazolo[5,4-d][1,3]thiazole (0.035 g, 3.6×10^{-5} mol) and compound (9) (0.035 g, 4.1×10^{-5} mol) were used in this polymerization, and the polymer was obtained as a green film like solid (0.010 g). Weight averaged molecular weight (M_w) = 32 kg mol^{-1}, polydispersity index (PDI) = 1.7.

Synthesis of copolymer TT2. Following the general polymerization procedure, bis[5-(trimethylstannyl)-3-undecylthiophen-2-yl]-[1,3]thiazolo[5,4-d][1,3]thiazole (0.026 g, 2.7×10^{-5} mol) and compound (11) (0.038 g, 2.7×10^{-5} mol) were used in this polymerization, and the polymer was obtained as a dark purple film like solid (0.037 g). M_w = 127 kg mol^{-1}, PDI = 3.5.

Synthesis of copolymer BT1. Following the general polymerization procedure, 5,11-bis[5-(trimethylstannyl)-3-undecylthiophen-2-yl]-4,10-dithia-6,12-diaza tricyclo[7.3.0.$0^{3,7}$]dodeca-1,3(7),5,8,11-pentaene (0.053 g, 5.2×10^{-5} mol) and compound (9) (0.046 g, 5.2×10^{-5} mol) were used in this polymerization, and the polymer was obtained as a glass green solid (0.052 g). M_w = 142 kg mol^{-1}, PDI = 2.1.

Synthesis of copolymer BT2. Following the general polymerization procedure, 5,11-bis[5-(trimethylstannyl)-3-undecylthiophen-2-yl]-4,10-dithia-6,12-diaza tricyclo[7.3.0.$0^{3,7}$]dodeca-1,3(7),5,8,11-pentaene (0.029 g, 2.9×10^{-5} mol) and compound (11) (0.040 g, 2.9×10^{-5} mol) were used in this polymerization, and the polymer was obtained as a dark green film like solid (0.049 g). M_w = 231 kg mol^{-1}, PDI = 3.9.

References

[1] Ashraf, R. S.; Kronemeijer, A. J.; James, D. I.; Sirringhaus, H.; McCulloch, I. *Chem. Commun*. **2012**, *48*, 3939−3941.

[2] Van Pruissen, G. W. P.; Gholamrezaie, F.; Wienk, M. M.; Janssen, R. A. J.; *J. Mater. Chem*. **2012**, *22*, 20387−20393.

[3] Koizumi, Y.; Ide, M.; Saeki, A.; Vijayakumar, C.; Balan, B.; Kawamoto, M.; Seki, S. *Polym. Chem*. **2013**, *4*, 484-494.

[4] Ide, M; Koizumi, Y.; Saeki, A.; Izumiya, Y.; Ohkita, H.; Ito, S.; Seki, S. *J. Phys. Chem. C* **2013**, *117*, 26859−26870.

[5] Chen, M. S.; Niskala, J. R.; Unruh, D. A.; Chu, C. K.; Lee, O. P.; Fréchet,J. M. J.; *Chem. Mater.*, **2013**, *25*, 4088–4096.

[6] Vohra, V.; Kawashima, K.; Kakara, T.; Koganezawa, T.; Osaka, I.; Takimiya, K.; Murata, H. *Nat. Photo*. **2015**, *9*, 403–409.

[7] Ide, M.; Koizumi, Y.; Saeki, A. *J. Photopolym. Sci. Tech*. **2016**, *29*, 565–569.

[8] Ren, G.; Schlenker, C. W.; Ahmed, E.; Subramaniyan, S.; Olthof, S.; Kahn, A.; Ginger, D. S.; Jenekhe, S. A. *Adv. Funct. Mater*. **2013**, *23*, 1238–1249.

[9] Bhuwalka, A.; Mike, J. F.; He, M.; Intemann, J. J.; Nelson, T.; Ewan, M. D.; Roggers, R. A.; Lin, Z.; Jeffries-EL, M. *Macromolecules*, **2011**, *44*, 9611–9617.

[10] Subramaniyan, S.; Xin, H.; Kim, F. S.; Shoaee, S.; Durrant, J. R.; Jenekhe, S. A. *Adv. Energy Mater*. **2011**, *1*, 854–860.

[11] Osaka, I.; Saito, M.; Koganezawa, T.; Takimiya, K. *Adv. Mater*. **2014**, *26*, 331–338.

[12] A. Saeki, M. Tsuji, S. Yoshikawa, A. Gopal, S. Seki, J. Mater. Chem. A, 2014, 2, 6075–6080.

[13] A. Gopal, A. Saeki, M. Ide, S. Seki, ACS Sustainable Chem. Eng. 2014, 2, 2613–2622.

[14] D. Veldman, S. C. J. Meskers, R. A. J. Janssen, Adv. Funct. Mater. 2009, 19, 1939–1948.

[15] Ide, M.; Saeki, A.; Koizumi, Y.; Koganezawa, T.; Seki, S. *J. Mater. Chem. A* **2015**, *3*, 21578–21585.

[16] Veldman, D.; Meskers, S. C. J.; Janssen, R. A. J. *Adv. Funct. Mater*. **2009**, *19*, 1939 – 1948.

[17] Larson, B. W.; Whitaker, J. B.; Wang, X. –B.; Popov, A. A.; Rumbles, G.; Kopidakis, N.; Strauss, S. H.; Boltalina, O. V.; *J. Phys. Chem. C* **2013**, *117*, 14958−14964.

[18] Lei, T.; Cao, Y.; Zhou, X.; Peng, Y.; Bian, J.; Pei, J. *Chem. Mater*. **2012**, *24*, 1762−1770.

[19] Dutta, G. K.; Han, A-R.; Lee, J.; Kim, Y.; Oh, J. H.; Yang, C. *Adv. Funct. Mater*. **2013**, *23*, 5317–5325.

[20] Kim, G.; Kang, S.-J.; Dutta, G. K.; Han, Y. –K.; Shin, T. J.; Noh, Y. Y.; Yang, C. *J. Am. Chem. Soc*. **2014**, *136*, 9477−9483.

[21] Bronstein, H.; Hurhangee, M.; Fregoso, E. C.; Beatrup, D.; Soon, Y. W.; Huang, Z.; Hadipour, A.; Tuladhar, P. S.; Rossbauer, S.; Sohn, E.-H.; Shoaee, S.; Dimitrov, S. D.; Frost, J. M.; Ashraf, R. S.; Kirchartz, T.; Watkins, S. E.; Song, K.; Anthopoulos, T.; Nelson, J.; Rand, B. P.; Durrant, J. R.; McCulloch, I.; *Chem. Mater.* **2013**, *25*, 4239−4249.

[22] Rivnay, J.; Mannsfeld, S. C. B.; Miller, C. E.; Salleo, A.; Toney, M. F. *Chem. Rev*. **2012**, *112*, 5488−5519.

[23] DeLongchamp, D. M.; Kline, R. J.; Herzing, A. *Energy Environ. Sci.* **2012**, *5*, 5980-5993.

[24] Osaka, I.; Saito, M.; Koganezawa, T.; Takimiya, K. *Adv. Mater*. **2014**, *26*, 331–338.

[25] Guo, X.; Zhou, N.; Lou, S. J.; Smith, J.; Tice, D. B.; Hennek, J. W.; Ortiz, R. P.; Navarrete, J. T. L.; Li, S.; Strzalka, J.; Chen, L. X.; Chang, R. P. H.; Facchetti, A.; Marks, T. J. *Nature Photo*. **2013**, *7*, 825–833.

[26] Zhou, E.; Nakano, M.; Izawa, S.; Cong, J.; Osaka, I.; Takimiya, K.; Tajima, K.; *ACS Macro Lett*. **2014**, *3*, 872−875.

[27] Blom, P. W. M.; de Jong, M. J. M.; Vleggaar, J. J. M.; *Appl. Phys. Lett*. **1996**, *68*, 3308–3310.

[28] Saeki, A.; Yoshikawa, S.; Tsuji, M.; Koizumi, Y.; Ide, M.; Vijayakumar, C.; Seki, S. *J. Am. Chem. Soc*. **2012**, *134*, 19035−19042.

[29] Liu, Y.; Zhao, J.; Li, Z.; Mu, C.; Ma, W.; Hu, H.; Jiang, K.; Lin, H.; Ade, H.; Yan, H.; *Nature Commun*. **2014**, *5*, 5293/1−8.

[30] Nguyen, T. L.; Choi, H.; Ko, S.-J.; Uddin, M. A.; Walker, B.; Yum, S.; Jeong, J.-E.; Yun, M. H.; Shin, T. J.; Hwang, S.; Kim, J. Y.; Woo, H. Y. *Energy Environ. Sci*. **2014**, *7*, 3040−3051.

[31] Søndergaard, R.; Hösel, M.; Angmo, D.; Larsen-Olsen, T. T.; Krebs, F. C.; *Mater. Today* **2012**, *15*, 36−49.

[32] Ma, Z.; Wang, E.; Jarvid, M. E.; Henriksson, P.; Inganäs, O.; Zhang, F.; Andersson, M. R. *J. Mater.*

Chem., **2012**, *22*, 2306–2314.

[33] Tomassetti, M.; Ouhib, F.; Wislez, A.; Duwez, A. -S.; Penxten, H.; Dierckx, W.; Cardinaletti, I.; Bovee, R. A. A.; van Pruissen, G. W. P.; Jérôme, C.; Manca, J.; Maes, W.; Detrembleur, C. *Polym. Chem*. **2015**, *6*, 6040–6049.

[34] Guo, X.; Ortiz, R. P.; Zheng, Y.; Kim, M.; Zhang, S.; Hu, Y.; Lu, G.; Facchetti, A.; Marks, T. J.; *J. Am. Chem. Soc.* **2011**, *133*, 13685–13697.

Chapter 5: Conclusion of this dissertation

The present thesis was focused on the molecular design of electron accepting unit for organic photovoltaics. The results obtained through this work are summarized as follows.

Chapter 1 reviewed the background of organic photovoltaics and development of electron-accepting pigments for conjugated copolymers. Strong electron withdrawing property affects both the energy level and π-stack, as well as the orientation of polymer backbone in the thin film.

Chapter 2 summarized the synthesis of the electron-accepting thienoisoindigo (TIDG) and its copolymers. Some of the TIDG copolymers showed the large absorptions in near infrared region due to the high planarity and small dihedral angle between the donor and acceptor units. High planarity observed for cyclopentadithiophene (CPDT)-TIDG copolymer is associated with the small bandgap of around 1.0 eV and relatively high hole mobility. The TIDG copolymer coupled with fluorene was also found to work as the n-type semiconducting copolymer by blending with poly(3-hexylthiophene) (P3HT) and achieved 0.06% PCE. The low-lying LUMO levels of TIDG copolymers are suggestive of the ambipolar use in organic photovoltaics.

Chapter 3 provided an insight into the carrier dynamics of TIDG copolymers in OPV devices. The fill factors (FF) of **P1** and **P3** were less than 0.5, due to the influence of bulk recombination in the blend film. On the other hand, **P2** reached the relatively high FF of 0.57, in spite of the low current density (~1.67 mA cm^{-2}). External quantum efficiency measurement revealed that the near infrared absorption of **P2** does not contribute to the generation of photocurrent density in OPV devices. By using transient absorption spectroscopy, the singlet lifetime of **P2** was found extremely short, which is competitive with the time required for exciton diffusion to the p-type/n-type semiconductor interface. This chapter provided the important insight into the tradeoff between absorption region and lifetime of singlet exciton, which is termed as the energy gap law. Among the three TIDG-copolymers, **P3** achieved the highest PCE of 1.4% with [6,6]-phenyl-C_{61}-butyric acid methyl ester ($PC_{61}BM$) because of comparatively longer singlet exciton lifetime than **P1** or **P2**. However, **P3** showed the edge-on orientation, which is not advantageous for carrier transporting in OPV devices, and thus the author

expected that there are many spaces for further improvements.

Chapter 4 described the synthesis of benzothienoisoindigo (BTIDG) copolymers based on the molecular design to simultaneously address the issues found in TIDG copolymers. Through the selection of the rigid donor unit and thiophene spacers, BTIDG copolymers ensured the high solubility, optimized energy level, and face-on orientation suitable for OPV. **BT2**, the copolymer of benzobisthiazole and BTIDG, achieved 4.2% PCE for the blends with $PC_{71}BM$. The BTIDG copolymers demonstrated the strong face-on orientation, and its ratio increased up to 95% in pristine **BT2**, because the large donor π-plane merits the formation of crystallites. The high face-on orientation ratio in the film state correlated with the hole mobility measured by using SCLC. Although the BDT-BTIDG copolymer showed the comparative PCE with that of BDT-TIDG, there is still a room to improve the PCE by controlling morphology and solubility by introducing thiophene spacer and side chain.

As above, this study exemplified the molecular design and evaluation of optoelectronic properties from the aspects of symmetricity, planarity, solubility, spacer, backbone orientation, and energy level of copolymers, all of which parameters are of importance for the high power conversion efficiency of OPV. Since TIDG copolymers indicated the absorption in near infrared region in spite of low PCE, the author expects the possibility to apply them to transparent photovoltaics. Additionally the present work proposes the feasibility to make a use of TIDG copolymers as the n-type buffer materials, because their LUMO levels are relatively deep. BTIDG copolymers demonstrated the high face-on orientation ratio in thin film and guide a new molecular design for polymer semiconducting materials.

List of Publication

1. Koizumi, Y.; Ide, M.; Saeki, A.; Vijayakumar, C.; Balan, B.; Kawamoto, M.; Seki, S. "Thienoisoindigo-based Low-band Gap Polymers for Organic Electronic Devices" *Polym. Chem.* **2013**, *4*, 484–494.

2. Ide, M.; Koizumi, Y.; Saeki, A.; Seki, S. "Ambipolar Low-bandgap Copolymers Consisting of Dhithienoketopyrrole for All-Polymer Solar Cells" *J. Photopolym. Sci. Technol.* **2013**, *26*, 217–221.

3. Ide, M.; Koizumi, Y.; Saeki, A.; Izumiya, Y.; Ohkita, H.; Ito, S.; Seki, S. "Near-Infrared Absorbing Thienoisoindigo-Based Copolymers for Organic Photovoltaics" *J. Phys. Chem. C* **2013**, *117*, 26859–26870.

4. Ide, M.; Saeki, A.; Koizumi, Y.; Koganezawa, T.; Seki, S. "Molecular Engineering of Benzothienoisoindigo Copolymers Allowing Highly Preferential Face-on Orientations" *J. Mater. Chem. A* **2015**, *3*, 21578–21585.

5. Ide, M.; Koizumi, Y.; Saeki, A. "Control of Phase Separation of Benzothienoisoindigo-Benzodithiophene Copolymer for Organic Photovoltaics" *J. Photopolym. Sci. Tech.* **2016**, *29*, 565–569.

List of Supplementary Publication

1. Saeki, A.; Yoshikawa, S.; Tsuji, M.; Koizumi, Y.; Ide, M.; Vijayakumar, C.; Seki, S.
"A Versatile Approach to Organic Photovoltaics Evaluation Using White Light Pulse and Microwave Conductivity"
J. Am. Chem. Soc. **2012**, *134*, 19035–19042.

2. Gopal, A.; Saeki, A.; Ide, M.; Seki, S.
"Fluorination of Benzothiadiazole–Benzobisthiazole Copolymer Leads to Additive-Free Processing with Meliorated Solar Cell Performance"
ACS Sustainable Chem. Eng. **2014**, *2*, 2613–2622.

3. Minami, S.; Ide, M.; Hirano, K.; Satoh, T.; Sakurai, T.; Kato, K.; Tanaka, M.; Seki, S.; Miura, M.
"2,6-Diphenyl- and -distyryl-capped 3,7-Dialkoxybenzo[1,2-b:4,5-b']dithiophenes and Their Dithieno-annulated Higher Homologs: Structural Phase Transition with Enhanced Charge Carrier Mobility"
Phys. Chem. Chem. Phys. **2014**, *16*, 18805-18812.

4. Al-Naamani, E.; Ide, M.; Gopal, A.; Saeki, A.; Osaka, I.; Seki, S.
"Study of Photoelectric Conversion in Benzotrithiophene-Based Conjugated Semiconducting Polymers"
J. Photopolym. Sci. Tech. **2015**, *28*, 605-610.

5. Al-Naamani, E.; Ide, M.; Gopal, A.; Saeki, A.
"Insight into the Energy Loss in Organic Solar Cells Based on Benzotrithiophene Copolymers: A Dark Current Analysis at Low Temperature"
Jpn. J. Appl. Phys. **2016**, *55*, 022303/1–4.

6. Shimata, Y.; Ide, M.; Tashiro, M.; Katouda, M.; Imamura, Y.; Saeki, A.
"Charge Dynamics at Heterojunction between Face-on/Edge-on PCPDTBT and PCBM Bilayer: Interplay of Donor/Acceptor Distance and Local Charge Carrier Mobility"
J. Phys. Chem. C **2016**, *120*, 17887–17897.

7. Kumano, M.; Ide, M.; Seiki, N.; Shoji, Y.; Fukushima, T.; Saeki, A.
"A Ternary Blend of Polymer, Fullerene, and Insulating Self-Assembling Triptycene Molecules for Organic Photovolatics"
J. Mater. Chem. A **2016**, *4*, 18490–18498.

Acknowledgements

This study is supported by many people. The author would like to express her most sincere gratitude to her supervisor, Associate Professor Akinori Saeki at Department of Applied Chemistry, Graduate School of Engineering, Osaka University. The author believes that she could not complete her study without his insightful suggestions, invaluable institutions and hearty encouragement. The author also would like to express gratefully appreciation to Dr. Yoshiko Koizumi for informative suggestion and dedicated support for her experiments from the beginning of this research. Her sincerity for research inspires the author and encouraged this research progress. The author wishes to make a grateful acknowledgement to Professor Shu Seki at Department of Molecular Engineering, Graduate School of Engineering, Kyoto University. His advanced insights and sophisticated thinking process influenced her researcher's life.

The author is grateful to Professor Yoshio Aso and Professor Masahiro Miura for reviewing this dissertation and providing critical comments. The author is deeply indebted to Assistant Professor Kyoko Inoue and Specially Appointed Researcher Hiroshi Moriguchi in Analytical Instrumentation Facility for their support in NMR and MALDI TOF MASS measurement. The author also is indebted to Mr. Kunihiko Kamon and Mr. Hiromi Ohi for Elemental Analysis center for elemental analysis measurement.

This study is supported by collaborators, and thus the author deeply appreciates Prof. Itaru Osaka at Hiroshima University and Dr. Tomoyuki Koganezawa at Japan Synchrotron Radiation Research Institute (JASRI) for 2D-GIXRD measurement, and Prof. Hideo Ohkita, Mr. Yuta Izumiya, Prof. Shinzaburo Ito at Kyoto University for TAS measurement.

The author also gives thankful for members in her laboratory, Ms. Eman Al-Naamani Rashid Said, Mr. Naoki Ishida, Mr. Yoshiki Shimata, Mr. Ryosuke Nishikubo, Mr. Shinji Nagasawa, Mr. Frank Elias Caraballo Hidalgo, Mr. Kenta Aoshima, Mr. Kento Yamada, Professor Motohiro Nakano, Dr. Kazuyuki Enomoto, Dr. Katsuyoshi Takano, Dr. Haruyuki Baba, Dr. Yoshihito Honsho, Dr. Anesh Gopal, Dr. Tsubasa Mikie, Dr. Takahiro Fukumatsu, Dr. Tsuneaki Sakurai, Dr. Daisuke, Sakamaki, Dr. Chakooth Vijayakumar, Dr. Bijitha Balan, Dr. Masaaki Omichi, Dr. Wakana Matsuda, Mr. Yuta Maeyoshi, Ms. Hiromi Marui, Mr. Takenori Fujiwara, Mr. Masashi Tsuji, Mr. Yoshihiro Yasutani, Mr. Michael T Tang, Ms. Saya Yoshikawa, Mr. Sho Yamanaka, Ms. Tomoyo Miyakai, Mr. Wasin Tuchinda, Mr. Cheng Hoi Lok, Mr. Satoru Yoneda, Mr. Yuki Noguchi, Ms. Mariko Noguchi, Mr. Yuki Takeshita, Mr. Yoshihiro

Shioaku, Mr. Toshiyuki Kobashi, Mr. Masataka Kumano, Mr. Hikaru Oga, Mr. Kenji Kuwada, Mr. Wookjin Choi, Mr. Yusuke Tsutsui, Mr. Hiroshi Tomita, Mr. Yuki Tsujimoto, Mr. Akifumi Horio and all people who collaborated with author. The author is grateful for encouragement from colleagues, Ms. Yukari Hayashi and Dr. Yoichi Hoshimoto.

The author also acknowledges financial support from Japan Society for the Promotion of Science (JSPS) scholarship (No. 261480) during her Ph.D course.

Finally the author is thankful for my parents, Hiromu Ide and Kazuko Ide, her brother, Ryo Ide, grandparents, Haruaki Ide, Fumiko Ide, Hiroshi Katsuragawa, Hisako Katsuragawa, her uncle and aunts, Mitsuru Ide and Akiko Miura. The author gives thanks for all of them for their continuous support and encouragement.

January 2017

Marina Ide